Alloying Effect On Nanostructure Formation In Iron-based Soft Magnetic Materials

Zhang Yanrong

School of Materials Science and Engineering

A thesis submitted to the Nanyang Technological University
in fulfillment of the requirement for the degree of
PhD of Engineering

2007

ACKNOWLEDGEMENTS

The author would like to express her utmost appreciation to her supervisor A/Prof. Raju V. Ramanujan. During the past three years, he not only guided me in research but also provided considerable help in life. He taught me how to be a good researcher and how to conduct a project at a high level. Therefore, the author owes her achievement in research to her kind supervisor.

The author also wants to thank her family. Only with their support could she finish the project smoothly.

The author would like to express her gratitude to Dr Li Huafang, Dr Du Siwei, Dr Chris Boothroyd and Dr Foo Yong Lim of IMRE and Dr Y. Yoshizawa of Hitachi Metals for their kindness and help in research.

Last but not least, credit is given to Guo Jun, Irene, Lee Chin and Johnson from Advanced Materials Characterization Lab and Eric, Thomas, Patrick and Nelson from Metals Processing Lab for their assistance in carrying out the experiments.

TABLE OF CONTENTS

LIST OF TABLES

LIST OF FIGURES

ABSTRACT

In this project four alloy compositions were selected: $Fe_{77.5}Si_{13.5}B_9$, $Fe_{76.5}Si_{13.5}B_9Cu_1$, $Fe_{74.5}Si_{13.5}B_9Nb_3$ and $Fe_{73.5}Si_{13.5}B_9Nb_3Cu_1$. Thermal properties by DSC, phase formation by XRD, microstructural observation by TEM and magnetic properties by VSM were compared to elucidate the effects of Cu and Nb alloying additions in the $Fe_{73.5}Si_{13.5}B_9Nb_3Cu_1$ alloy.

In the case of the $Fe_{77.5}Si_{13.5}B_9$ alloy, crystallization resulted in the formation of the b.c.c. Fe-Si phase with an unusual dendritic morphology, the dendrite branches are composed of closely spaced crystals, the spacing between the crystals is a few nanometers. Hot stage in-situ TEM observation of the crystallization process of this alloy showed that the initial stage of crystallization resulted in an equiaxed morphology, followed by a morphological transition to a dendritic morphology. Significantly, this transition occurred beyond a critical size of about 45nm. A parameter related to the transition was determined to be in the range of 0.013-0.031, this experimental result lies in the range of theoretical predictions. Hence, the dendrite formation is consistent with the morphological stability theories of Mullins-Sekerka, Nesbit and Langer.

In the case of the $Fe_{76.5}Si_{13.5}B_9Cu_1$ alloy, 1 at% Cu alloying addition in the Fe-Si-B alloy resulted in the crystallization of a b.c.c. Fe-Si phase about 100nm in size, exhibiting a spheroidal morphology with rough interfaces, addition of Cu increases the nucleation density and influences the growth processes. Interestingly, the nucleation density in the

Fe-Si-B-Cu alloy is considerably less than that observed in the Fe-Si-B-Nb-Cu alloy, which showed that Nb also plays a role in increasing the nucleation density.

In the case of the $Fe_{74.5}Si_{13.5}B_9Nb_3$ alloy, 3 at% Nb alloying additions induced heterogeneous nucleation and growth of equiaxed crystals (about 50nm in size) of the Fe-Si, $Fe_{23}B_6$ and Fe_3B phases. Nb alloying additions changed the mechanism of crystallization from primary crystallization in the Fe-Si-B alloy to eutectic crystallization in the Fe-Si-B-Nb alloy.

In the case of $Fe_{73.5}Si_{13.5}B_9Nb_3Cu_1$ alloy addition of both Cu and Nb resulted in the smallest crystal size and highest crystal density, these alloying additions **synergetically** increase the crystal density and reduce the crystal size. Our model suggest that repulsion between Cu and Nb atoms resulted in the formation of both Cu rich and Nb rich regions, which is helpful for the formation of Cu and Nb clusters. In regions with low crystal density, Cu clusters can act as nucleation sites consistent with Hono's model. And the retardation of growth in regions with low crystal density the growth rate was reduced, as suggested by the Hunziker's model, by the strong interaction of Cu, Si, Nb and B. While in the regions containing high crystal density, Nb clusters can act as nucleation site due to the similar b.c.c. structure of Fe and Nb and the strong attractive interaction between Si and Nb. As well, soft impingement and Nb-B aggregates were crucial to inhibit the crystal growth. Our observations show that *both* Cu and Nb alloying additions play a crucial role in nucleation as well as growth stage, which is different from earlier models of nanocrystallization in this alloy system.

Chapter 1 INTRODUCTION

Soft magnetic materials are widely used in electric and electronic parts such as magnetic recording heads, transformers and inductors. Hence, the development of novel soft magnetic materials is an important area of materials research and development. Efforts are being made to achieve better soft magnetic properties in order to conserve energy by reducing losses in transformer cores and to achieve high efficiency electronic components. This effort involves developing new compositions as well as novel microstructures. The development of transition metal-metalloid type of metallic glasses using melt-spinning techniques was a major advance to achieve better soft magnetic properties.

The metallic glass compositions suitable for soft magnetic applications are mainly iron based alloys, of which the Fe-Si-B amorphous alloy composition is a typical example. In the Fe-Si-B alloy, Fe possesses high saturation magnetization, the addition of B aids in the formation of the amorphous state and addition of Si to the Fe-B system enhances the thermal stability of the alloy. The amorphous Fe-Si-B based alloys show important changes in their magnetic properties after crystallization. The crystallized fraction, the crystal morphology and the nature of the crystallized phases play a significant role in the change of the magnetic properties. Investigations have been particularly focused on materials that can produce nanocrystalline microstructures that have superior magnetic properties. The alloy with the composition $Fe_{73.5}Si_{13.5}B_9Nb_3Cu_1$ is the most well known commercial soft magnetic materials developed using this methodology[1-2]. Herzer's random anisotropy model has been used to explain the excellent soft magnetic properties

in this alloy [3]. When the crystal size is less than the intercrystal exchange coupling length, the magnetic anisotropy is reduced, leading to high saturation magnetization together with low coercivity.

Since the development of the $Fe_{73.5}Si_{13.5}B_9Nb_3Cu_1$ alloy in 1988 (trade name Finemet), great interest has been aroused owing to its soft magnetic properties, the magnetization of the alloy after heat treatment at 550 °C for 1 h may reach 1.2 T while the coercivity is 0.5 A/m[1,2]. The good magnetic properties are due to the crystallization of a high density of nanocrystals of the Fe-Si phase, with an average size of about 10 nm within the initially amorphous alloy [3].

Several studies have been carried out in order to elucidate the mechanism of nanostructure formation in this alloy [1,4,5,6,7-11]. It was shown that Cu and Nb alloying additions play a crucial role in the formation of nanocrystals.

Regarding the role of Cu alloying addition in this alloy there have been several contradictory reports: Yoshizawa and Yamauchi suggested that Cu clusters form prior to crystallization leading to an increase in the local concentration of Fe in the vicinity of these clusters, resulting in the formation of α-Fe crystals [7]. By means of atom probe field ion microscopy (APFIM) Hono et al found that after short time annealing at 550 °C, Cu clusters of few nanometers in size were formed, these clusters acted as heterogeneous nucleation sites for the α-Fe crystals [4-6]. On the other hand Ayers et al suggested that due to the similar crystal structure of f.c.c Cu and the DO_3 structure of the α-Fe phase,

f.c.c Cu clusters acted as the catalyst for the formation of a Fe-Si phase with the DO_3 crystal structure [8,9]. Duhaj suggested that the decisive factor in the process of primary crystallization from an amorphous alloy is the short-range order in the amorphous structure, which strongly depends on the mixing enthalpy of constituents [10].

Concerning the role of Nb alloying additions in the $Fe_{73.5}Si_{13.5}B_9Nb_3Cu_1$ alloy, Yavari assumed that a sharp concentration gradient of Nb exists at the crystal: matrix interface, this gradient would hinder the diffusion of Fe and Si, reducing the growth of the nanocrystal [11]. However, by means of Mossbauer spectrometry it was suggested that there was very little segregation of Nb atoms at the crystal: matrix interface. Nb diffuses out of the crystal but it does not just get segregated at the interface, rather it diffuses into the amorphous matrix giving rise to a diffuse Nb concentration gradient [12]. Hermann assumed that boron enrichment in combination with the presence of Nb leads to a diffusion barrier stopping the crystal growth [13]. On the other hand, another model has suggested that soft impingement by overlapping diffusion fields surrounding the crystals can lead to the observed retardation of crystal growth [14,15]. Hunziker suggested that diffusive interactions between Cu, Nb, Si and B can reduce the growth rate [16].

Thus, there is no clear understanding of the individual and particularly the crucial synergistic roles played by combined additions of Cu and Nb, although it is experimentally observed that both elements must be present in adequate concentration to produce the desired nanostructure. Most previous studies were conducted in the alloy containing both Cu and Nb alloying additions. It is well known that both Cu and Nb

alloying additions will influence the thermodynamics and kinetics of the crystallization in the $Fe_{73.5}Si_{13.5}B_9Nb_3Cu_1$ alloy. Hence, in order to obtain a fundamental understanding of the effects of Cu and Nb alloying additions in the $Fe_{73.5}Si_{13.5}B_9Nb_3Cu_1$ alloy, attention should be paid to individual as well as combined additions of Cu and Nb to the reference Fe-Si-B alloy.

Hence, $Fe_{77.5}Si_{13.5}B_9$, $Fe_{76.5}Si_{13.5}B_9Cu_1$, $Fe_{74.5}Si_{13.5}B_9Nb_3$ and $Fe_{73.5}Si_{13.5}B_9Nb_3Cu_1$ alloys were selected in this project. By comparing the thermal behavior, phase formation, microstructural observations and magnetic properties of the selected alloys the individual and synergistic effects of Cu and Nb alloying additions will be elucidated.

Chapter 2 LITERATURE REVIEW

In this chapter the development of soft magnetic materials will be introduced. Commercial soft magnetic materials with nanostructures formed by annealing the melt-spun amorphous alloys, such as the Finemet, Hitperm and Nanoperm class of alloys, will be introduced. The kinetics and thermodynamics governing these soft nanostructured magnetic materials will be introduced. The effects of Cu, Nb and other alloying additions in Finemet type alloys will be summarized.

2.1 Development of soft magnetic materials

The types of magnetism found in materials include diamagnetism, paramagnetism, ferromagnetism; antiferromagnetism and ferrimagnetism are considered to be subclasses of ferromagnetism. All materials exhibit at least one of these types of magnetism and the behavior broadly depends on the response of their electrons to the application of an externally applied magnetic field. In order to describe the various classes of magnetic materials susceptibility, the ratio of the magnetization (M) to the applied field (H) is used. $\chi = M/H$. The susceptibility is generally used to measure how magnetizable a substance can become in the presence of a magnetic field. Diamagnetism is a very weak form of magnetism that is nonpermanent and persists only while an external field is being applied. The volume susceptibility for diamagnetic solid materials is of the order of -10^{-5}. Paramagnetism is a relatively weak form of magnetism that results from the independent alignment of atomic magnetic dipoles with an applied magnetic field. Susceptibilities for paramagnetic materials range from about 10^{-5} to 10^{-2}. Ferromagnetism is a permanent and

large magnetization found in some metals (e.g., Fe, Ni and Co), which result from the cooperative parallel alignment of neighboring magnetic moments. Magnetic susceptibilities as high as 10^6 are possible for ferromagnetic materials.

Soft magnetic materials are widely used in energy related applications due to factors such as their high magnetic permeability (μ_e). [17]. Permeability is the ratio of the magnetic induction (B) to the magnetic field strength (H). The relation between susceptibility and permeability is that: $\mu_e = \mu_0(1+\chi)$, where μ_0 is the relative permeability. Thus in soft magnetic materials susceptibity should be high.

Saturation magnetization (M), i.e., is a material specific property defined as the magnetic moment (m) per unit volume (V). M = m/V. It represents the maximum induced magnetic moment that can be obtained in a magnetic field (H_{sat}). Since the mass of a sample is generally much easier to determine than the volume, magnetization is often alternately expressed as a mass magnetization defined as the moment per unit mass. Magnetocrystalline anisotropy (K_1) is the energy necessary to deflect the magnetic moment in a single crystal from the easy to the hard direction. The easy and hard directions arise from the interaction of the spin magnetic moment with the crystal lattice (spin-orbit coupling). Magnetostriction constant (λ_s) is a measure of the dimensional change exhibited by ferromagnetic materials when subjected to a magnetic field. Thus in order to get good soft magnetic properties high Ms, low K_1 and high λ_s are necessary.

There has been a long history of materials development of soft magnets. Pure iron is a

good candidate for soft magnetic materials according to the above requirements and iron was used in transformers many years ago. However, the performance of commercially pure iron is very sensitive to impurities like N and C, which makes the permeability unstable at temperatures around 100 °C. Another disadvantage of pure iron is its low electrical resistivity. A material with low electrical resistivity placed in an AC magnetic field will result in high energy loss through heating by induced eddy currents.

Among the conventional soft magnetic materials, ferrites have exceptionally high electrical resistivity and therefore low eddy losses. In addition, a careful choice of the elements in ferrites combined with a proper heat treatment may reduce K_1 to a very low value and hence a high permeability can be obtained.

A similar situation exists in nickel-iron alloys (Permalloys) [18]. At room temperature, iron has a positive K_1 while nickel has a negative value, the signs of the magnetostriction constant λs of iron and nickel are also opposite at room temperature. Therefore there is an excellent opportunity to obtain a high performance soft magnetic material with nearly zero K_1 and λs by alloying suitable amount of iron in nickel.

Another type of soft magnetic materials which has high initial permeability and other favorable properties is Sendust (Fe-Al-Si) alloys, which has been widely used in recording heads [19]. Ferrites, Sendust and nickel-iron alloys find only limited application in power transformation devices because of their relatively low saturation magnetization and Curie temperature.

Iron-cobalt alloys have the highest saturation magnetization and Curie temperature among soft magnetic materials. These alloys have been used in aircraft electric generators, which reduce the weight and size of the generators. An important iron-cobalt soft magnetic alloy is Hiperco Alloy 50(49%Fe-49%Co-2%V) [20]. The 2% vanadium improves the ductility and markedly increases the resistivity.

In order to develop soft magnetic materials with large saturation magnetization Ms, high effective permeability μ_e and low coercive field Hc, efforts are being made to develop metastable structures with better soft magnetic properties. For example, the technique of rapid quenching from melt has been used in order to prepare Fe-Si-B alloys. Figure 2. 1 shows the calculated isothermal sections at 900 ˚C and 1000 ˚C. The experimental phase equilibria reported by Tatsuya T. [21], was shown Figure 2. 1. From the experimental data, a phase equilibrium between FeB, Fe_5SiB_2, and FeSi were identified at both 900 ˚C and 1000 ˚C. On the other hand, XRD analysis of the prepared alloys equilibrated at 900 ˚C showed that a phase equilibrium between FeB, $Fe_{4.7}Si_2B$, and FeSi existed [21].

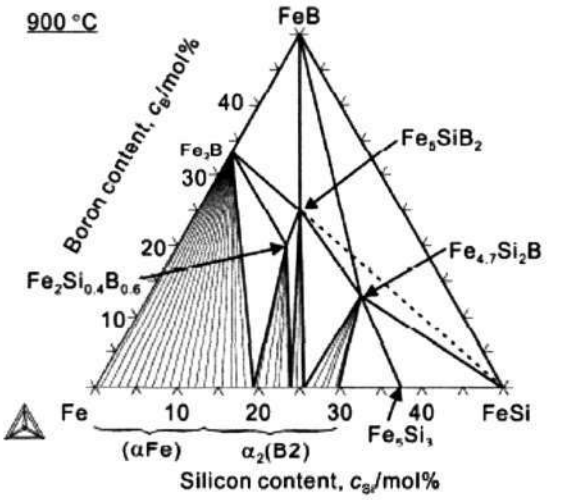

(a)

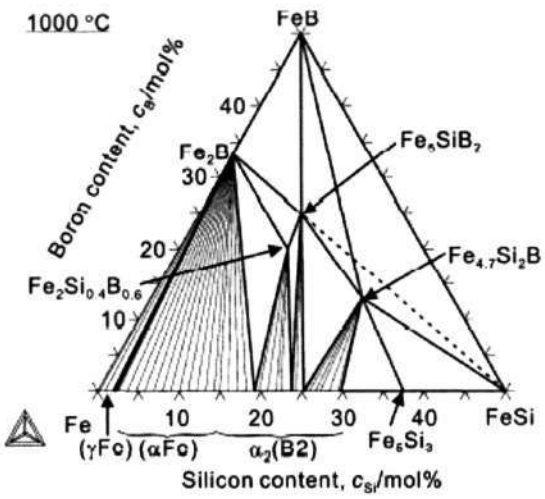

(b)

Figure 2. 1 Calculated isothermal section diagrams of the Fe–Si–B system at: (a) 900 and (b) 1000 ˚C.

The development of transition metal-metalloid type of metallic glasses using the melt-spinning technique was a major advance towards achieving better soft magnetic properties in metastable/non-equilibirium alloy phases. The metallics glass behaves as a

very soft magnetic material since its magnetocrystalline anisotropy is low and thus it exhibit lowest hysteresis loss. Thus it is widely applied in electronic transformers. The metallic glass compositions suitable for soft magnetic applications are usually either based on Fe or Co. The Fe based amorphous alloys possess high saturation magnetization but at the same time they have high magnetostriction, resulting in strong stress induced anisotropy causing the coercive field to increase. On the other hand Co based amorphous alloys can have almost zero magnetostriction but their saturation magnetization is relatively low compared with Fe based alloys.

Yoshizawa et al.[1] of Hitachi Metals Ltd., Japan, discovered another class of non-equilibrium microstructures consisting of nanocrystals dispersed in an amorphous matrix, which possess high saturation magnetization and low coercivity. They called this material Finemet. The pioneering work of Yoshizawa et al. has led to intensive activity in this field aimed at developing a detailed understanding of the formation of nanocrystalline phase, and their unique magnetic properties. Extensive efforts are also being made to find alternative alloy compositions. In addition to Finemet alloys a number of other nanaocrystalline Fe-Zr-B (Nanoperm) [22] and Fe-Co-Zr-B-Cu (Hitperm) [23] alloys have been developed which also exhibit similar nanocrystallization behavior and improved magnetic properties.

2.2 Novel Nanostructured Soft Magnetic Materials

2.2.1 Finemet Alloys

As mentioned earlier Yoshizawa et al. [1, 2] showed the potential of the Fe-Si-B-Nb-Cu

alloys as nanocrystalline soft magnetic materials. The amorphous $Fe_{73.5}Si_{13.5}B_9Nb_3Cu_1$ alloy was prepared by the melt-spinning method and subsequently annealed. The optimum annealing temperatures were in the range from 763 K to 833 K. After annealing, the microstructure consisted of a high density of Fe-Si nanocrystals about 10 nm in size dispersed in the remaining amorphous matrix, this microstructure was found to yield low loss and high permeability [24,25]. The reduction of crystal size below the regime of the domain wall size is a well-known approach to subdivide the material into single domain crystals, it increases the coercive field H_c towards a maximum value determined by the anisotropy present [26]. However, if the crystal size is reduced even further to less than 100 nm, the coercivity decreases again proportional to D^6 (D is the crystal size) due to the averaging of anisotropy. This point becomes clear from Figure 2. 2 where coercive field is plotted as a function of crystal size for different magnetic materials [27]. Conventionally, in order to increase the soft magnetic property, attempts have been made to make the crystal size as large as possible to obtain low coercivity and high permeability. However, from Figure 2. 2 it is evident that low coercivity can also occur in nanomagnetic materials. This situation is realized, for example, in the case of superparamagnetic crystals where the coercivity decreases because of thermal excitations in isolated or weakly coupled crystals [27].

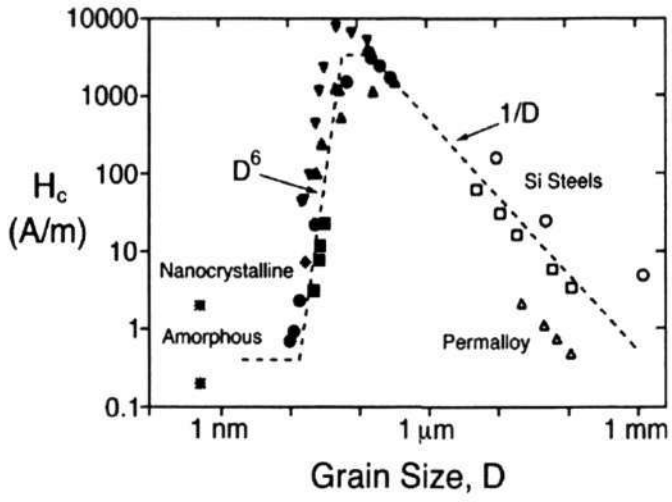

Figure 2. 2 Schematic illustration of the dependence of coercivity as a function of crystal size [27]

In the superparamagnetic regime although the coercivity vanishes, the permeability also goes down drastically. Materials with weak intergranular magnetic interactions are not good soft magnetic materials. In contrast to this, in the case of nanocrystalline alloys produced by partial crystallization of amorphous phase, strong magnetic interaction between individual crystals exists via the intervening amorphous phase, and thus at room temperature the crystals are aligned ferromagnetically with respect to each other. Magnetic softening occurs because the crystal size as well as the intergranular spacing is smaller than the ferromagnetic exchange length, the local anisotropies are reduced by exchange interaction and the average anisotropy becomes low[28]. The role of intergranular interaction via the amorphous matrix is evident from the temperature dependence of the coercive field as well as the initial permeability [29]. Further, the magnetostriction of the amorphous and nanocrystalline phases being opposite in sign,

they tend to cancel each other and therefore, the average magnetostriction of this composite material decreases with progressive increase in nanocrystallisation [30], and thus a low magnetostriction is achieved for an optimum volume fraction of nanocrystalline phase. Thus, the superior soft magnetic properties of this composite material arise as a result of the combined magnetic response of the nanocrystals and amorphous matrix [31].

2.2.2 Nanoperm Alloys

Since 1990, another class of nanostructured soft magnetic materials has been developed in Japan. It is based on the Fe-M-B systems (M=Zr, Hf or Nb), and is called Nanoperm [32]. The biggest improvement of the Nanoperm alloys compared with Finemet alloys is the higher magnetic flux density Bs of 1.5 T, due to the higher Fe content compared to Finemet alloys[33].

This type of material is also prepared by melt-spinning followed by annealing. The nanocrystalline ternary Fe-M-B alloys consist of α-Fe crystals about 20 nm in size surrounded by a small volume fraction of amorphous matrix. The matrix has a high Curie temperature because of the high M and B concentrations [34].

The intercrystal exchange coupling between the α-Fe crystals proceeds via the matrix. The soft magnetic properties are significantly improved with decreasing crystal size and increasing Curie temperature of the amorphous matrix. Additional improvements can be achieved with small alloying additions of Cu [35]. The Fe-Zr-Nb-B-Cu alloy system has

a crystal size of 7 nm, nearly zero magnetostriction, high Tc of amorphous matrix (500 K), high effective permeability μ_e (>10^5 at 1 kHz) and low Hc(<2 A/m)[36,37].

2.2.3 Hitperm Alloys

McHenry et al. [38] substituted half of Fe with Co in a Nanoperm based alloy with the aim of obtaining a soft magnetic material with higher operating temperatures. They found that the alloy with composition $(Fe_{0.5}Co_{0.5})_{88}Zr_7B_4Cu_1$ showed promising properties. They named this alloy Hitperm, the thermomagnetic properties of the Hitperm alloy are better than Nanoperm and the flux density is larger [39]. Figure 2. 3 shows the permeability and the magnetic induction data of several families of soft magnetic alloys including the three nanostructured materials discussed above.

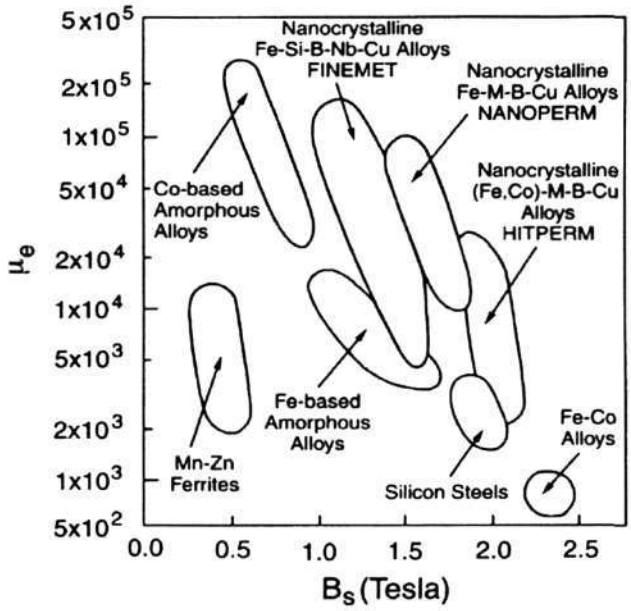

Figure 2. 3 Relationship between permeability, μ_e (at 1 kHz) and saturation magnetization for soft magnetic materials [39]

2.3 Nanocrystalline Soft Magnet Theory

After the Finemet alloy was developed many studies have been carried out to explain why it exhibits excellent magnetic properties. The most commonly accepted model is based on Herzer's work [40,41] relating coercivity to crystal size. Herzer found that when the crystal size is reduced to the order of nanometers below the single-domain crystal size, the coercivity decreases with decreasing crystal size. Herzer's work is important because it is in good agreement with experimental results.

Herzer [40, 41] found that for an α-Fe based soft magnetic alloy it is useful to define an exchange length:

$$L_0 = \sqrt{A / K_1} \qquad \text{Eq.2. 1}$$

Where A denotes the exchange stiffness and K_1 is the anisotropy constant.

When the crystal size is smaller than L_0, Herzer applied the Alben-Becker-Chi model for random-anistropy systems to account for the average anisotropy constant (K):

$$\langle K \rangle \approx K_1 (D/Lex)^{3/2} \qquad \text{Eq.2. 2}$$

where the exchange length Lex is related self-consistently to the average anisotropy constant by

$$L_{ex} = \sqrt{A/\langle K \rangle} \qquad \text{Eq.2. 3}$$

By combining (2.2) and (2.3) we have

$$\langle K \rangle \approx \frac{K_1^4}{A^3} D^6 \qquad \text{Eq.2. 4}$$

Because the coercivity is directly proportional to <K>, we have

$$H_c = C' \times D^6 \qquad \text{Eq.2. 5}$$

Where C' is a constant for a specific material.

This D^6 correlation agrees very well with experimental results, as shown in Figure 2. 2 for various Fe based alloys. Chudnovsky et.al. [42] has studied the extension of random-anistropy theory to nanostructures.

The normalization of L_{ex} given by Eq.2.3 is derived from the interplay of anisotropy and exchange energy. As magnetocrystalline anisotropy is suppressed by exchange interaction, the exchange length scale expands, and thus the local anisotropy is averaged out.

Further investigations made by Herzer [43] confirmed the above conclusion that intercrystal exchange coupling is the reason for the dramatically reduced coercivity with decreasing crystal size. The intercrystal exchange coupling takes place via the amorphous crystal boundaries which typically have thicknesses of several atomic layers in Fe-based nanostructured materials. When the temperature increases, the amorphous crystal boundary component becomes paramagnetic. This will certainly decrease the ferromagnetic exchange coupling. Experiments showed that when temperature increased up to 573 K, at which the amorphous matrix became paramagnetic, the coercivity of the alloys increased remarkably [44].

2.4 Thermodynamics in FINEMET Alloys

The difference of the Gibbs energy between the crystalline and the amorphous phase is the driving force for nucleation and initial crystalline growth [5,6]. There are three modes of crystallization of amorphous alloys: polymorphous, eutectic and primary crystallizations. Figure 2. 4 illustrates a schematic free energy–composition curve for a crystallization mode by annealing the amorphous alloy.

The first mode is polymorphous crystallization in which the free energy is reduced by changing from an amorphous to a crystalline structure without any change in composition. The final microstructure comprises of β phase crystals embedded in the α phase matrix. The crystallization reaction of the amorphous phase occurs in two stages, i.e.amorphous →α→α+β. Polymorphous crystallization is the mode which is least observed experimentally.

The second mode is eutectic crystallization, for compositions between c and d the solution is supersaturated with respect to both α and β phases. In such a case, eutectic crystallization occurs by which two phases appear usually with a lamellar structure. The initially amorphous alloy reaches equilibrium after crystallizing by the eutectic crystallization mode, thus this crystallization reaction occurs in one stage. The decomposition with the eutectic mode is thus represented as: amorphous→ α+β.

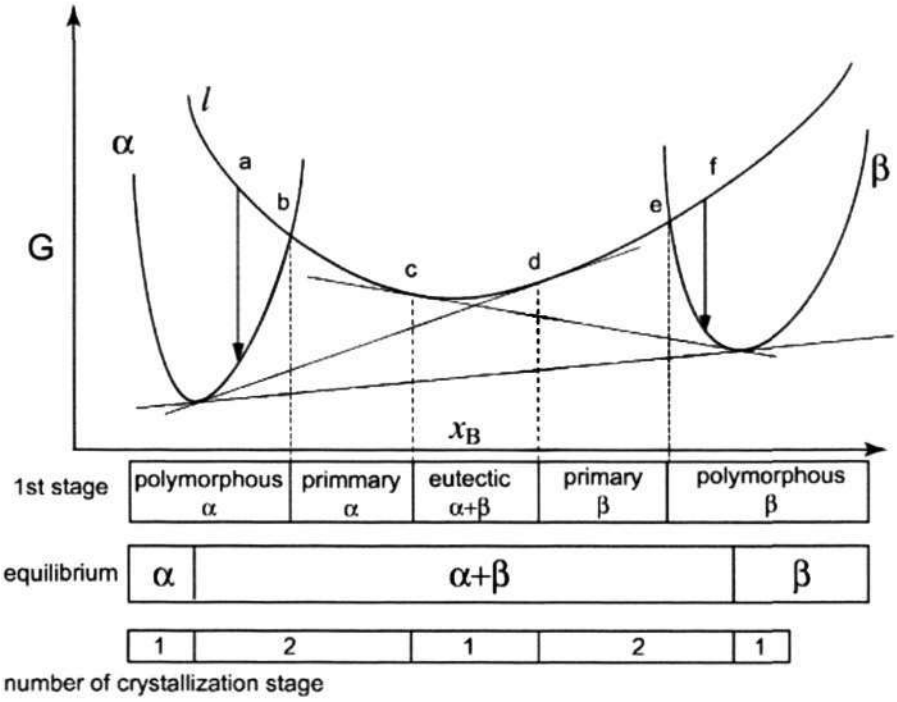

Figure 2. 4 Hypothetical free-energy composition diagrams to explain possible modes of crystallization from an amorphous alloy [6].

Nanocrystallization occurs mainly by the primary crystallization mode. In this mode the composition is between the polymorphous and eutectic regions, i.e. compositions between b and c, and d and e. Due to solute rejection during crystallization the remaining amorphous matrix transforms by one of the other mechanisms described above. Hence, the crystallization process of the amorphous alloy in two stages: amorphous →α+amorphous →α+β.

All amorphous alloys crystallize by one of the above mechanisms, depending on the thermodynamic driving force and the kinetics of each possible reaction. Thus the kinetics

of crystallization of amorphous alloys is also important.

2.5 Kinetics of crystallization in Finemet Alloys

The crystallization of Finemet alloys has been found to occur by two stages: one is primary crystallization (at temperatures between 480 °C and 580 °C) of Fe-Si nanocrystals which are relatively stable. The second stage is the crystallization at temperatures above 600 °C of the remaining amorphous matrix by the formation of the Fe-B compound phase. Concerning the kinetics of the crystallization process of the Finemet alloy there have been many studies using Differential Scanning Calorimetry (DSC), X-ray diffraction (XRD), Mossbauer spectroscopy (MS), X-ray synchrotron radiation and nuclear magnetic resonance (NMR) techniques[45,46,47,48,49,50]. In many cases modeling of the kinetics of the primary crystallization in the Finemet alloy has been based on the Johnson–Mehl -Avrami -Kolmogorov (JMAK) [15] kinetic model. However other reports by continuous-heating and isothermal DSC, X-ray, electron microscopy and Mossbauer kinetic analysis suggest that the JMAK law cannot fit the experimental data [46,51]. By continuous-heating and isothermal DSC measurements Illekova proposed a mechanism for the crystallization of Finemet-type alloys [46,51]. In this mechanism the JMAK model can be applied to the early stages of the crystallization. An alternative model, the normal-crystal-growth (NGG) kinetic law was suggested, the kinetics are controlled by a rearrangement of niobium atoms and independent of Cu and Si content. The JMAK and NGG models will now be described.

2.5.1 JMAK Model

The JMAK model for isothermal primary crystallization kinetics considers modifications to simple first-order reaction rate kinetics, the rate of transformation depends linearly on the volume fraction of the remaining amorphous matrix, *1-X(t)*, with a rate constant k which reflects thermal activation:

$$k = k_0 \exp\left(\frac{-Q}{k_B T}\right) \qquad \text{Eq.2. 6}$$

Here Q is the activation energy barrier to crystallization, k_B is the Boltzmann constant and k_0 is a constant.

The JMAK equation, for *X(t)*, is written in the general form:

$$X = 1 - \exp[-(kt)^n] \qquad \text{Eq.2. 7}$$

where X is the volume fraction transformed after time t, k is a nucleation and growth rate constant and the Avrami exponent, n, The Avrami exponent characterizes the dimensionality of the transformation and depends on whether the transformation is interface or diffusion controlled and also on the nucleation rate. Assuming constant or decreasing nucleation rate and isotropic growth, one obtains $3<n<4$ for interface controlled and $1.5<n<2.5$ for diffusion-controlled transformations. [6,13,15].

From a determination of *X(t)* at various temperatures, *k(T)* can be determined and Q_{JMA} inferred from the Arrhenius equation. Ozawa plots [52] can also be used to determine the activation energy for crystallization.

It should be noted that the assumptions of the JMAK model do not accurately represent experimental observations of nanocrystallization in an initially amorphous iron-based alloys[46,53-56], instead Avrami exponents $n<1$ are typical. This suggests that the crystallization process in nanostructured iron-based alloys cannot be understood in terms of the conventional JMAK model. Some limitations of the model are: (1) crystallization is considered in an unlimited medium, (2)the nucleation rate does not depend on the local microstructure, (3)the existence of a critical radius of nucleation is neglected, (4)the growth rate does not depend on the local chemical composition and its change during crystallization[13].

There have been attempts to reformulate and generalize the JMAK model. Fanfoni and Tomellini[54] derived an expression which can be used in treating the kinetics of growth of multiphase systems. Erukhimovitch and Baram[55] proposed an integral equation for the time evolution of the transformed volume fraction. Sessa et al [56] examined, by two-dimensional computer simulations, the validity of the JMAK model with respect to both random and nonrandom distribution of nuclei. They found that once the condition of randomness is relaxed, Eq.2.7 does not hold anymore.

Uebele and Hermann[57] studied by means of three-dimensional computer simulations the influence of non-uniform random and partially ordered distributions of nuclei on the crystallization kinetics. They showed that cluster like arrangements of nuclei cause a decrease of n in comparison with random homogeneous distribution. Hermann et al. [13]

proposed a theoretical approach to crystallization kinetics which takes into account the influence of microstructure and microstructural changes during crystallization. The critical radius of nuclei and slowly diffusing inhibitors were found to be controlling parameters for the evolution of the crystals. The authors derived a multiparameter integral equation which could explain the isothermal transformation data of some Finemet alloys. It was shown that the accumulated Nb atoms or Nb–B aggregates could act as inhibitors at the interface of nanocrystals. Pradell and Barandiaran [47, 58] attributed the anomalously low Avrami exponent to a soft impingement mechanism, following a transient interface controlled growth and decreasing nucleation rate. Terasa[15] modified the JMAK model by considering the following factors: (1) the dimensionality of the growing crystal, (2) the time dependence of the nucleation rate, (3) whether growth is linear or parabolic and (4) the eventual impingement of growing crystals at long times.

2.5.2 Normal Crystal Growth(NGG) Model

The driving force for the NGG process is the decrease of interfacial enthalpy, which is assumed to be related to the measured DSC signal [46]. The NGG model is not necessarily related to the existence of a nanocrystalline product. The nucleation and growth of the b.c.c. α-Fe based phase is generally manifested in the early stages of the transformation and the transformation is assumed to be controlled by a specific rearrangement of Nb atoms [46,60].

In the NGG process, larger crystals increase their size at the expense of smaller crystals. The driving force for this process is the decrease in interfacial enthalpy

$$H(t) = \frac{H_0 r_0}{r(t)} \qquad \text{Eq.2. 8}$$

where H_0 and r_0 respectively are the initial interfacial enthalpy and the initial average crystal radius. The increase in average crystal radius r is controlled by the following kinetic equation [59]:

$$\frac{dr}{dt} = \frac{K(T)}{mr(t)^{m-1}} \qquad \text{Eq.2. 9}$$

where the crystal growth rate constant $K(T)$ has an Arrhenius-like temperature dependence:

$$K(T) = A_{GG} \exp(-\frac{E^*_{GG}}{RT}) \qquad \text{Eq.2. 10}$$

m, A_{GG} and E^*_{GG} are the crystal growth exponent, pre-exponential factor and activation energy respectively. The change of the total interfacial enthalpy is related to the measured DSC signal $H(t)$ as:,

$$H(t) = H_0 + \int_0 H(t')dt' = H_0[1-\alpha(t)] \qquad \text{Eq.2. 11}$$

Combining Eqs. 2.08 2.09 and 2.11 gives the integral crystal growth kinetic equation:

$$[1-\alpha(t)]^m = \frac{\tau_{GG}(T)}{t+\tau_{GG}(T)} \qquad \text{Eq.2. 12}$$

where the time constant $\tau_{GG}(T)$ is related to the rate constant: $\tau_{GG}(T) = r_0^m(T)/K(T)$

$H_o(T)$ is directly measurable by integrating the entire isothermal DSC signal. On the basis of the kinetic Eq.2.12 the exponent $1/m$ can be obtained as the slope of the $\ln[1-\alpha(t)]$ vs. $\ln(t+\tau_{GG})$ curve.

Using this model Illekova obtained $m = 2$ which is consistent with the parabolic kinetics of the normal crystal growth process [60]. Regarding the application of the NGG model to Finemet alloys, it was assumed the microstructure of Fe-Si-B-like alloys consists of two types of regions [60]. One type consists of the regions occupied by the iron atoms having at least one boron nearest neighbor (Fe-B clusters) and the other type consists of regions without boron, the silicon atoms occupying the latter regions, e.g., Fe-Si clusters. The Fe-Si clusters would be the elementary structural units which move by collective quasi-jumps through the crystal-amorphous matrix interface, this growth mechanism is controlled by the diffusion of Nb out of the growing nanocrystal. Therefore the experimentally observed growth of the Fe-Si like nanocrystals in the early stages of crystallization of the Finemet alloy could be rationalized [61]. As the crystallization proceeds the validity of the parabolic law is associated with the migration of the crystal interfaces.

2. 6 Effect of Cu alloying additions in Finemet Alloys

The role of Cu in the formation of nanocrystalline microstructures in Finemet alloys is extremely important [62]. The following section will discuss the effect of Cu alloying additions.

2.6.1 Yoshizawa and Yamauchi's model

Yoshizawa and Yamauchi[1,2] explained that the formation of nanocrystalline microstructure in the Finemet alloy is due to the formation of small clusters of Cu prior to nanocrystallization, these clusters have a higher local concentration of Fe in their

vicinity, leading to the observed fine α-Fe crystals.

2.6.2 Hono's Model

By means of atom probe field ion microscopy (APFIM) Hono[4,5] found that after short annealing at 550 °C Cu clusters of a few nanometers in size had already formed and that Cu clusters served as nucleation sites for the α-Fe-Si phase. The following model of the crystallization process was put forward (Figure 2. 5): in the initial stage of annealing, diffusion of Cu occurs so that Cu rich clusters form. Chemical inhomogeneity of alloying elements (particularly of Fe) is induced by Cu cluster formation and causes an increased number of nucleation sites for the formation of the crystalline phase. Since Nb and B have negligible solubility in the Fe-Si phase, they are excluded from the crystallized fraction, and Nb and B enriched residual amorphous phases are formed. The Cu rich clusters continue to grow during crystallization. The nanocrystallization process of Finemet alloy is schematically presented in Figure 2. 5[6]:

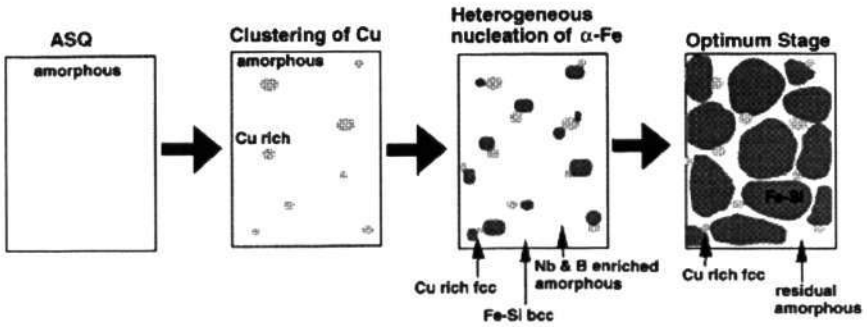

Figure 2. 5 Schematic drawing of microstructural evolution in melt-spun Finemet amorphous alloy by primary crystallization(Hono's model)

2.6.3 Ayers' Model

Based on the results of EXAFS and TEM studies Ayers [8, 9] proposed an alternative model which emphasized the role of Cu clusters in catalyzing nucleation of crystals with a DO_3 structure by providing low energy interfaces for nucleation. The crystallization process is described as occurring in four stages (Figure 2. 6): (1) Cu clusters precipitating from the amorphous matrix (2) DO_3 nanocrystals forming in intimate contact with the larger of these clusters enveloping the clusters as they grow. Cu clusters continue to form during the early stages of DO_3 crystallite coarsening. During the early stages of the crystallization process there should be growth of both the DO_3 nanocrystals and those Cu clusters which are not surrounded by the DO_3 phase. As the nanocrystals grow they reject Cu atoms and these atoms would cause Cu clusters in the untransformed matrix to grow. Once the supersaturation of Cu has dropped sufficiently, Ostwald ripening would cause further growth of the larger Cu clusters to occur at the expense of the smaller ones.

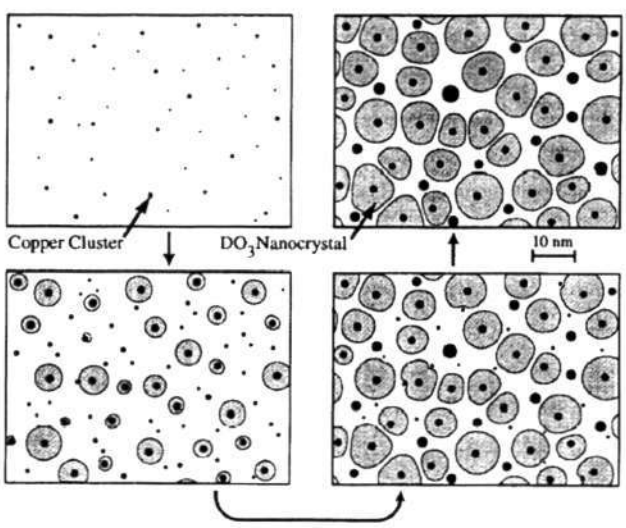

Figure 2. 6 Schematic representation of proposed model for the nucleation and growth of the Finemet alloy [8, 9].

One difference between Hono's model and Ayers' model is that in Ayers' model the Cu clusters were of two types: (a) those enveloped by subsequent Fe-Si crystals which cannot grow anymore and (b) those formed from atoms rejected by the Fe-Si crystals, which will grow further at the expense of the smaller clusters. However, in Hono's model, Cu clusters in contact with the Fe-Si crystals serve as nucleation sites.

2.6.4 Other assumptions

An important point is that in the Finemet alloy Cu loses its effectiveness to form the nanocrystalline phase in the absence of Nb[63]. On the other hand, in a number of alloys which contained no Cu additions a high volume fraction of nanocrystalline microstructure was observed, e.g. Fe–Zr–B, Fe–Nb–B, Co–Fe–Nb–B [64,65,66]. Thus, further understanding is required concerning the role of Cu and the synergy between Cu and Nb atoms. Using NMR techniques, Zhang et al. [67] have shown that short range order exists in the amorphous material. They demonstrated that the Fe-Zr-B system in the as quenched state contains a high density of amorphous regions that display fringe-like contrast which can be compared to the medium range order(MRO) structure proposed by Hirotsu et al.[68]. These regions increase in size and quantity with annealing, they probably act as embryos in the course of crystallization in a similar way as Cu-rich clusters do in Finemet alloys. Duhaj reported that the most important factor influencing the formation of nanocrystalline phase is the existence of medium-range ordered clusters with definite chemical composition in the as-quenched amorphous structure, such clusters increased in size upon annealing and act as embryos [10].

There have been several studies of the role of elements such as Ag, Pt, Pd and Mn substituting for Cu in Finemet type alloys. Cu substitution by Ag leads to higher crystallization temperature and higher crystallization activation energy. The substitution of Ag for Cu in Finemet alloys results in the pinning of the displacement of domain walls[69]. Cu substitution by Pd and Pt elements ($Fe_{73.5}M_1Nb_3Si_{13.5}B_9$ (M=Pd, Pt)) resulted in larger crystal sizes and the formation of the Fe_3B phase during primary crystallization, this phase was observed during secondary crystallization in Finemet alloys [70]. Cu substitution by Mn and Pt ($Fe_{73.5}Nb_3M_1Si_{13.5}B_9$(M=Cu, Mn, Pt)) resulted in the formation of new intermetallic phases like $FeMn_3$ or $FePt_3$ which caused a deterioration of soft magnetic properties. A lower volume fraction of Fe-Si nanocrystals and larger crystal size was favored if the Cu atoms are replaced by Pt and Mn due to the formation of the Nb-Fe-Si phase [71].

2. 7 Effect of Nb alloying additions in Finemet Alloys

We now examine the role of Nb alloying additions. There are two conditions for the formation of nanocrystallization [72]:

(a) Nanostructures can be formed by the controlled crystallization of an adequate hypoeutectic composition containing atoms with large differences in size in relation to the host atoms, such as Nb, which are preferably insoluble in the phase formed by primary crystallization. During primary crystallization, these large atoms with smaller diffusivities are rejected at the growing α-Fe-Si interfaces, forming a concentration gradient around the growing crystals.

(b) The matrix surrounding the growing crystals must remain amorphous. Boron which is added to facilitate the formation of the amorphous state from the liquid alloy is also rejected by the α-Fe-Si crystals. These two conditions are incorporated in Yavari's model. Yavari [11] assumed that during the formation of Fe-Si nanocrystals, boron atoms move rapidly in the amorphous phase away from the crystal boundaries whereas the Nb atoms diffuse more slowly and form a diffusion barrier limiting the crystal growth, a schematic model of the diffusion layer formed by Nb and B is shown in Figure 2. 7. Lecaude and Perron[73,74] also reached similar conclusions from calorimetric studies and enthalpy measurements.

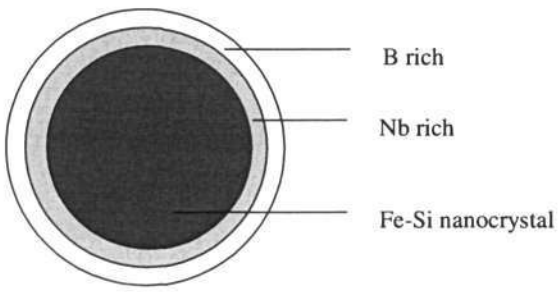

Figure 2. 7 Schematic drawing of boron and niobium diffusion layers ahead of the α-Fe: matrix interface, different shades indicate the b.c.c. phase, the Nb rich and B rich areas.

There are two important implications of these considerations. First, the crystals reach their final sizes which does not depend on the degree of the crystallization. This process indicates that the growth rate is slowed as the crystallization proceeds, due to the accumulation of the slower diffusing Nb atoms at the interface of the α-Fe-Si crystals. Secondly, the nucleation frequency is decreased due to the enrichment of the residual amorphous matrix by the faster diffusing B atoms[11].

An alternative model suggests that soft impingement is the dominant cause of retardation of growth in Finemet alloys. The term soft impingement refers to the decrease in the growth rate due to the overlap between the diffusion fields of two adjacent crystals, As shown in Figure 2. 8, the higher Nb concentration can be observed in the overlapping fields which hinder nanaocrystal growth.

This soft impingement following a transient interface controlled growth was introduced to explain decreasing nucleation rates during primary crystallization[58]. Soft impingement, used to model the crystallization process of Finemet alloy by Teresa[15], becomes more effective in the final stages of crystallization. It results from a reduction of the concentration gradient ahead of the interface, and may also result in a significant change of the solute diffusion coefficient at the interface. These changes reduce, and finally stop, crystal growth.

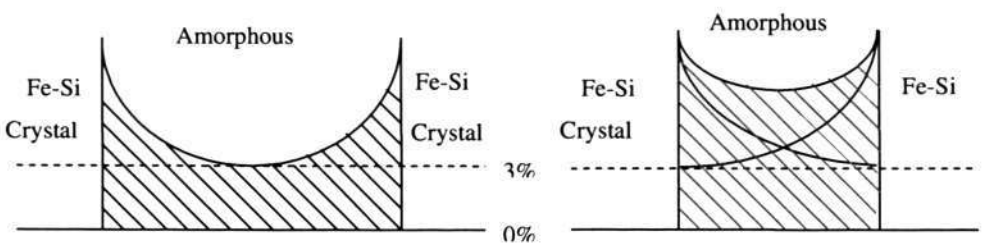

Figure 2. 8 Schematic representation of the dependence of Nb concentration profile on the amorphous layer thickness between neighbor nanocrystals: (a) at the initial stage of crystallization and (b) soft impingement in the overlapping fields. The 3% level represents the Nb concentration in the initial amorphous matrix and the 0% level the Nb concentration in the Fe-Si nanocrystal.

However based on small angle neutron scattering(SANS) results Hermann[75] proposed that the maximum size of the crystal is determined neither by the competition of nucleation and growth rates nor by diffusion field impingement but by the accumulation of Nb atoms or Nb-B aggregates acting as inhibitors at the surface of the nanocrystals.

In all the models previously discussed, diffusive interactions between the elements of the Finemet alloys were not considered, Hunziker[16] considered such interactions, assuming that two solutes with atomic radii smaller than the solvent will have attractive interactions. The diffusive interactions between the Nb, Cu, Si and B atoms were shown to inhibit crystal growth.

Many studies have been conducted in which Nb has been substituted by other elements, such as Mo, V, Cr, Ta, W[7,48]. Mo and V replacing Nb leads to a larger crystal size[7], after the same annealing conditions the volume fraction of the Fe-Si phase is increased due to the substitution of Nb by Mo and V [48].

The crystallization temperatures, magnetic properties, microstructures, composition, crystal structure and phases of Fe-Cu-M-Si-B (M = Cr, V, Mo, Nb, Ta, W) alloys were studied by means of DSC and TEM [7]. The crystallization temperature (Tx) increased with increasing M content and the magnitude of the increase of Tx is: Ta = Nb > W = Mo >V>Cr. On the other hand, Curie temperature(Tc) decreases with increasing M content and the magnitude of the decrease is in the order: Nb = Ta > W = Mo > V> Cr. The efficiency of suppression of b.c.c. crystal growth is: Nb=Ta>Mo=W>V>Cr, a similar

trend is observed in the soft magnetic properties. This suggests that a decrease of the crystal size by addition of the elements M contributes to the improvement of the soft magnetic properties; additions of 3 at% Nb is found to lead to the best soft magnetic properties.

Thus, it can be seen that soft magnetic properties of the Fe-Si-B-Nb-Cu alloy are critically dependent on the formation of a high density of nanocrystals in an amorphous matrix. This crystal formation, induced by selected heat treatment, depends critically on Cu and Nb alloying additions. In spite of considerable previous research work, there is no consensus on the effect of individual and combined additions of Cu and Nb in the Finemet alloy. Hence, this investigation was carried out to understand the roles of Cu and Nb alloying additions on the nanocrystallization process in Fe-Si-B-Nb-Cu alloys.

The next chapter will describe the experimental procedures employed in this project. The experimental parameters will also be introduced.

Chapter 3 EXPERIMENTAL METHODS

The experimental techniques used in this project include sample preparation and characterization. Sample preparation includes heat treatment of the melt spun amorphous ribbons. Operating parameters of the following experimental techniques are described: differential scanning calorimetry(DSC), X-ray diffraction(XRD), transmission electron microscopy(TEM), vibrating sample magnetometery(VSM).

3.1 Alloy System

The iron-based amorphous alloys used in this project were kindly provided by Dr Y. Yoshizawa of Hitachi Metals, Japan. The melt-spun amorphous alloys were received in the form of 20 μm thick and 25 mm wide ribbons and the compositions were: $Fe_{77.5}Si_{13.5}B_9$, $Fe_{74.5}Nb_3Si_{13.5}B_9$, $Fe_{76.5}Cu_1Si_{13.5}B_9$ and $Fe_{73.5}Cu_1Nb_3Si_{13.5}B_9$. The choice of 3 at% Nb and 1 at% Cu alloying additions in the Fe-Si-B alloy were selected based on the Finemet alloy composition: $Fe_{73.5}Cu_1Nb_3Si_{13.5}B_9$. The amorphous alloys were annealed in a vacuum furnace (10^{-5} torr) to induce crystallization.

3.2 Differential Scanning Calorimetry (DSC)

In DSC, the temperature difference between a reactive sample and a non-reactive reference is determined as a function of time, providing useful information about the phase transformation temperatures, thermodynamics and kinetics of reactions[76]. The Curie and crystallization temperatures can be obtained by DSC. Thermodynamic data, such as the heat released or absorbed in a phase transformation (latent heat), can also be

determined by DSC, the heat released/absorbed in a reaction is simply the area under the peak in a DSC curve.

The crystallization measurements of the selected alloys were performed from 200 °C to 800 °C with a NETZSCH DSC-404C using a continuous-heating regime. The vaccum in high T DSC is 10^{-2} torr. The samples were cut into small pieces (about 10 mg) and covered with an Al_2O_3 lid, an empty Al_2O_3 reference pan was used. The experiments were carried out at constant heating rate under vacuum (10^{-2} Torr), the heating rates were 2 K/min, 5 K/min, 10 K/min and 20 K/min. 3 samples were used to get each data point.

3.2 X-Ray Diffraction (XRD)

X-ray diffraction is essentially an interference phenomenon. X-rays can be deflected from their incident direction by collision with target atoms. When X-rays encounters an atom, scattering processes occur in all directions. If there is no change in the wavelength after scattering, it is coherent (elastic) scattering, while if the wavelength increases after scattering, the scattering is incoherent (inelastic).

Consider a section of crystal, its atoms arranged in a set of parallel (h k l) planes, A, B, C... having an inter-planar spacing d_{hkl}. X-ray beam of wavelength λ is incident on the crystal at an angle θ — called Bragg angle(Figure 3.1).

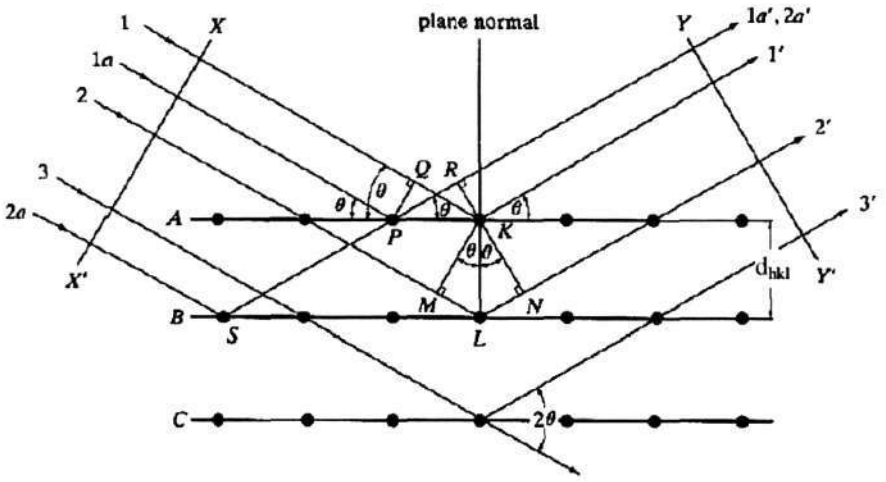

Figure 3. 1 Diffraction of X-rays by parallel atomic planes of a crystal [77]

The interplanar spacing, d, sets the difference in path length for the ray scattered from the top plane and the ray scattered from the bottom plane. Figure 3. 1 shows that this difference in path length is $2d\sin\theta$. Constructive wave interference (and hence strong diffraction) occurs when the difference in path length for the top and bottom is equal to an integral wavelength: $2d\sin\theta=n\lambda$(Bragg's law)

A diffraction pattern from a material typically contains many distinct peaks, each corresponding to a different interplanar spacing, d. Atomic periodicities with long repeat distance cause diffraction at small angles, while short repeat distances (as from small interplanar spacings) cause diffraction at high angles. Crystals with precise periodicities over long distances have sharp diffraction peaks. In a diffraction experiment, the incident wave must have a wavelength comparable to the spacing between atoms.

X-ray diffraction analysis was performed with a RIGAKU DMAX 2200 using Cu K。

radiation(λ=0.15405nm). The experimental conditions are listed in the following table:

Table 3. 1 XRD experimental conditions

Start angle	Stop angle	Step	Scan speed	Voltage	Current
30°	90°	0.02	1deg/min	50kV	20mA

3.3 Transmission Electron Microscopy (TEM)

The transmission electron microscopy (TEM) has become the premier tool for the microstructural characterization of materials. It has six main techniques:

(1) Conventional imaging (bright-field image and dark-field image)

(2) Electron diffraction (selected area electron diffraction, SAD)

(3) Phase-contrast imaging (high-resolution TEM, HRTEM)

(4) Energy-dispersive X-ray spectroscopy (EDS)

(5) Electron energy-loss spectroscopy (EELS)

A modern TEM has the capability of imaging the diffraction pattern (diffraction contrast imaging), imaging the phase contrast of the specimen (high-resolution imaging), obtaining diffraction patterns from selected areas of the specimen, and performing EELS and EDS spectroscopy measurements with a small, focused electron beam.

3.3.1 Two basic modes: SAD and Image

There are two basic modes in TEM: to form a diffraction pattern and to form an image.

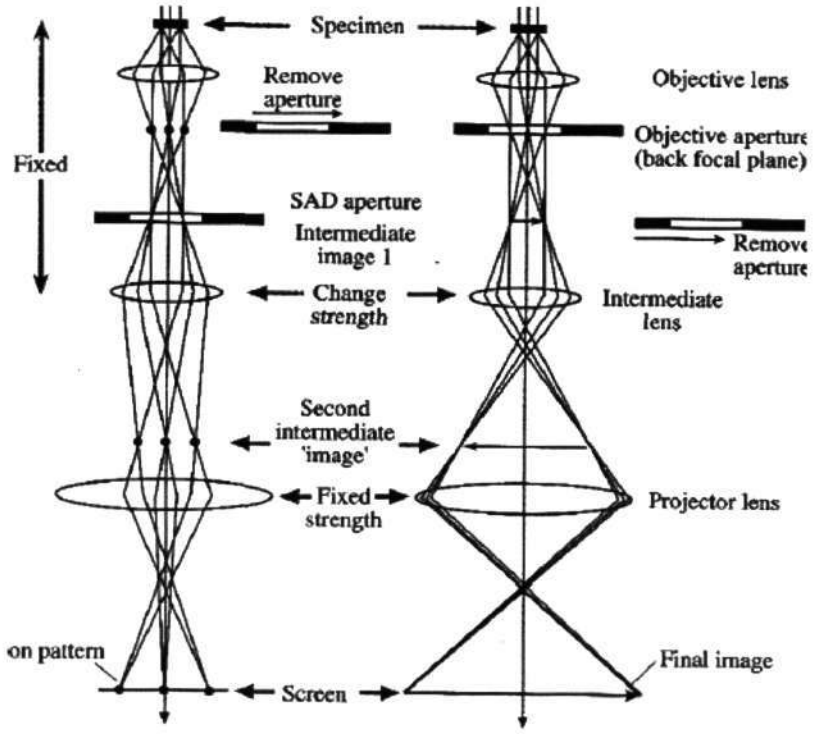

Figure 3. 2 Two basic modes in TEM: SAD and Image system [77]

As shown above, when the imaging system is adjusted so that the back focal plane of the objective lens is the objective plane of the intermediate lens, the diffraction pattern is projected onto the viewing screen. When the intermediate lens is adjusted so that its objective plane is the image plane of the projector lens, the image is projected onto the viewing screen.

3.3.1.1 Selected area diffraction pattern (SAD)

The diffraction pattern (DP) reflects the crystallography of the area of the specimen illuminated by the beam. Using the diffraction pattern, the crystal and its orientation can be identified. The positions of the allowed *hkl* reflections are characteristic of the crystal system. Indexing associates each point in the diffraction pattern with a plane, (*hkl*), in the crystal. From this indexing, the orientation of the crystal can be deduced in terms of the

zone axis [*uvw*] in which the indexed planes lie. This direction is normal to the plane of the DP and antiparallel to the electron beam, the convention is to define [*uvw*] as the beam direction.

3.3.1.2 Bright-field Image and Dark-Field Image

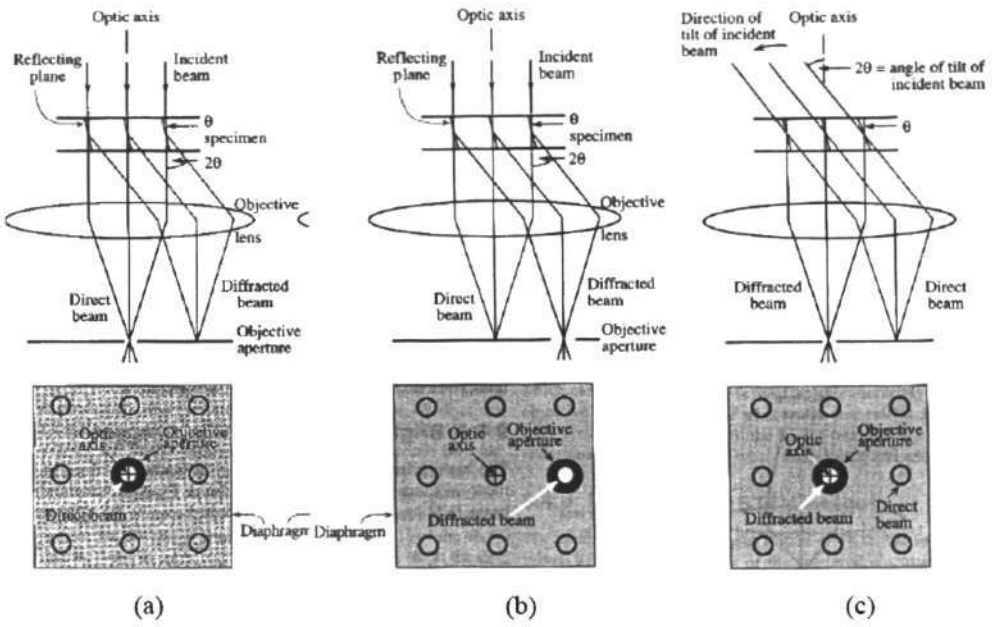

Figure 3. 3 (a) Bright-field (BF) mode (b) off-axis-dark-field (DF) mode and (c) Centered DF mode [90]

As illustrated in Figure 3. 3, each point in the back focal plane of the objective lens contains rays from all parts of the specimen. What distinguishes the points located in the back focal plane is that all rays entering a given point have been scattered by the specimen into the same angle. By positioning an objective aperture at a specific location in the back focal plane, an image is obtained with only those electrons that have been diffracted by a specific angle. When the aperture is positioned so that only the transmitted (un-diffracted) electrons can be observed, a bright field image is formed. When the

aperture is positioned so that only some diffracted electrons can be observed, a dark-field image is formed. When the aperture is centered around the optic axis, a centered dark field image results.

Dark field images were used to study the heat treated ribbon samples in order to determine the crystallization kinetics. In order to observe all the crystals six areas which cover the diffraction pattern are selected. From these DF images crystal number, and mean crystal size can be obtained in order to quantitatively determine the nucleation density, nucleation rate and growth rate.

3.3.2 High-resolution TEM (HRTEM)

A small aperture is used in bright-field and dark-field imaging to collect electrons that have been diffracted by the same angle. Producing a high-resolution image requires that we use an objective aperture large enough to include both the transmitted beam and at least one diffracted beam, the transmitted beam is required to provide a reference phase of the electron wavefront. High-resolution images are in fact interference patterns formed due to the phase relationships of the transmitted and diffracted beams.

3.3.3 Energy Dispersive X-ray Spectrometer (EDS)

When electrons are incident on the specimen, characteristic X-rays are emitted. These X-rays have a characteristic energy that is unique to the element from which it originates. These signals can be collected and sorted according to their energy. The EDS produces spectra that are plots of characteristic X-ray counts (or intensity) versus X-ray energy. By

identifying the peaks and determining the peak intensity ratio obtained in the EDS spectrum, we can obtain composition information of the specimen. After performing the Cliff-Lorimer[78] correction quantitative information can be obtained.

3.3.4 Electron Energy Loss Spectrometry

When an electron beam goes through a thin specimen, it may lose energy by a variety of processes. The reason we perform EELS is that we can isolate the inelastically scattered electrons and quantify the information they contain.

B mapping for the Fe-Si-B-Nb-Cu and Fe-Si-B alloys was conducted and Cu and Nb element mapping for the Fe-Si-B-Nb-Cu alloy was performed. For B, the energy selected for mapping is the K line(188 eV), for Nb the $M_{4,5}$ line(205 eV) and for Cu the L_3 line(951 eV).

EELS was also employed to measure the thickness of the TEM sample for quantitative studies of the crystallization process. The procedure for measuring the specimen thickness within a region defined by the incident beam is to record an energy-loss spectrum and to compare the area under the zero loss peak (I_0) with the total area under the whole spectrum (I_t). The thickness (t) can be given by

$$t / \lambda = \ln(I_t / I_0) \qquad \text{Eq.3. 1}$$

where λ is the total mean free path for inelastic scattering, the value of λ is required to obtain the thickness of the sample. For materials of known composition, λ can be obtained by using scattering theory to calculate λ in terms of the collection semiangle

β, the incident energy E_0 and a mean energy loss E_m which depends on the chemical composition of the specimen,

$$\lambda = \frac{106F(E_0 / E_m)}{\ln(2\beta E_0 / E_m)} \qquad \text{Eq.3. 2}$$

where λ is given in nm, β in mrad, E_o in keV, and E_m in eV; F is a relativistic factor equal to 0.618 for E_o = 200keV defined by

$$F = \frac{1 + E_0 / 1022}{(1 + E_0 / 511)^2} \qquad \text{Eq.3. 3}$$

This approximation is valid only for β<15 mrad.

For a specimen with known atomic number Z, E_m can be obtained from the approximate formula [79]

$$E_m \approx 7.6 Z_{eff}^{\ 0.36} \qquad \text{Eq.3. 4}$$

In the case of a compound the effective atomic number can be defined by

$$Z_{eff} = \frac{\sum_i f_i Z_i^{1.3}}{\sum_i f_i Z_i^{0.3}} \qquad \text{Eq.3. 5}$$

where f_i is the atomic fraction of each element of atomic number Z_i.

The collection semiangle β is given by:

$$\beta = (h / h_a) \times (R / L) \qquad \text{Eq.3. 6}$$

where h is the distance between the projector-lens crossover and the viewing screen (equal to 30 cm), h_a is the distance between the crossover and the spectrometer entrance aperture (equal to 72 cm), R is the radius of the selected entrance aperture (equal to 3 mm)

and L is the camera length of the diffraction pattern visible on the microscope viewing screen (equal to 12 cm). In the present case for the $Fe_{73.5}Si_{13.5}B_9Nb_3Cu_1$ alloy, β=10 mrad, Z_{eff}=23.9, E_m=23.8 eV and λ=107.3 nm.

A JEOL 2010 Transmission Electron Microscope (TEM) with an accelerating voltage of 200 kV was employed for microstructural observation. A Philips 300 kV TEM with EELS attachment was used for element mapping. In-situ hot stage observations were carried out in a JEOL 2000X TEM using an accelerating voltage of 200 kV. The sample holder was a Si plate and a thermocouple was used for the measurement of the temperature. Starting from room temperature, the temperature was increased until 400 °C and held for 30 min, subsequently at 25 °C intervals the specimen was left to thermally stabilize for 30 min and the observations were recorded. The shiny side of the ribbon was punched to a round shape, around 3 mm in diameter. Subsequently the specimen was annealed in a vacuum furnace. It was then thinned by ion milling machine.

3.4 Vibrating Sample Magnetometery (VSM)

When a sample is placed in a uniform magnetic field, a dipole moment proportional to the product of the sample susceptibility times the applied field is induced in the sample. If the sample is made to undergo sinusoidal motion as well, an electrical signal can be induced in suitably located stationary pick-up coils. This signal is proportional to the magnetic moment, vibration amplitude, and vibration frequency.

In this project, measurements of the magnetic properties were made using a LakeShore

7300 vibrating sample magnetometer. Standard thin foil sample holders were used. The saturation magnetization was obtained under maximum applied magnetic field of 1.2 T.

Chapter 4 RESULTS

In this chapter the thermal properties, phase formation, microstructural observation, crystallization behavior and magnetic properties of the $Fe_{77.5}Si_{13.5}B_9$, $Fe_{76.5}Si_{13.5}B_9Cu_1$, $Fe_{74.5}Si_{13.5}B_9Nb_3$ and $Fe_{73.5}Si_{13.5}B_9Nb_3Cu_1$ alloys will be described. The thermal properties were measured by DSC, phase formation after crystallization was identified by XRD. TEM was used to observe the crystallization products of the selected alloys. EDS was used to measure the concentration of the elements and EELS elemental mapping was conducted. VSM was used to measure the magnetic properties. In-situ hot stage TEM studies were carried out to observe dendrite formation in the case of the Fe-Si-B alloy and the crystallization behavior of the Fe-Si-B-Cu alloy. It was found that alloying additions of 1 at% Cu and 3 at% Nb had significant effects on the thermal properties, phase formation, morphology, crystallization behavior and magnetic properties.

4.1 $Fe_{77.5}Si_{13.5}B_9$ alloy

The thermal properties of the Fe-Si-B alloys were characterized using DSC techniques. The microstructure and phases formed after heat treatment at different temperatures for a series of annealing times were analyzed using TEM and XRD techniques[80]. The initial crystallization product was observed to posses an unusual dendritic morphology, the branches of the dendrites were composed of independent closely spaced crystals, the spacing between the crystals was of the order of several nanometers.

4.1.1 Thermal Analysis

By means of DSC the crystallization temperatures of the $Fe_{77.5}Si_{13.5}B_9$ alloy were measured at heating rates of 2, 5, 10, and 20 K/min respectively, as shown in Figure 4. 1.

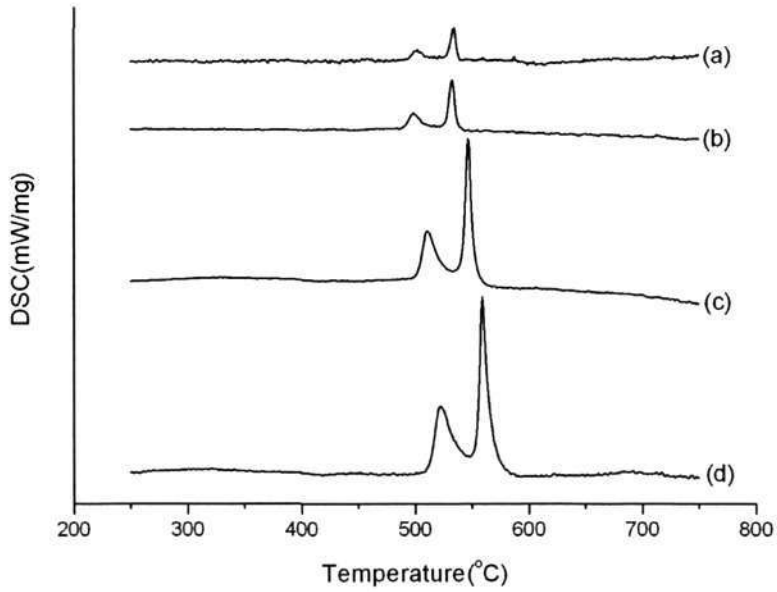

Figure 4. 1 DSC results for the $Fe_{77.5}Si_{13.5}B_9$ alloy at heating rates of: (a) 2 K/min, (b) 5 K/min, (c) 10 K/min and (d) 20 K/min

There are two exothermic peaks. The peak temperature of crystallization increased as the heating rate was increased from 2 K/min to 20 K/min. In Figure 4. 1 at a heating rate of 10 K/min, the first crystallization peak occurs at 527 °C while the second crystallization peak occurred at 552 °C, which is consistent with earlier reports [81,82,83,84,85].

By using the Doyle-Ozawa method the activation energies can be calculated by means of

the following equation [52]:

$$Logb = Log[AE / RF(\alpha)] - 2.315 - 0.4567E/(RT)$$

Where b is the heating rate, A is a constant, $F(\alpha)$ is the crystallized fraction, T is the temperature corresponding to the crystallized fraction, E is the activation energy and R is Boltzmann constant.

Plotting $Logb$ as the Y-axis and $1/T$ as the X-axis a straight line can be obtained, the slope of which is $-0.4567E/R$, thus the activation energy can be calculated(Figure 4. 2). By using software "ORIGIN" the slope was calculated to be: -194345±305.1 and -17610±1993.9 for the first and second peak respectively. Thus the activation energy corresponding to the first peak is calculated to be 376±5.9 kJ/mol while that of the second is 342±38.7 kJ/mol.

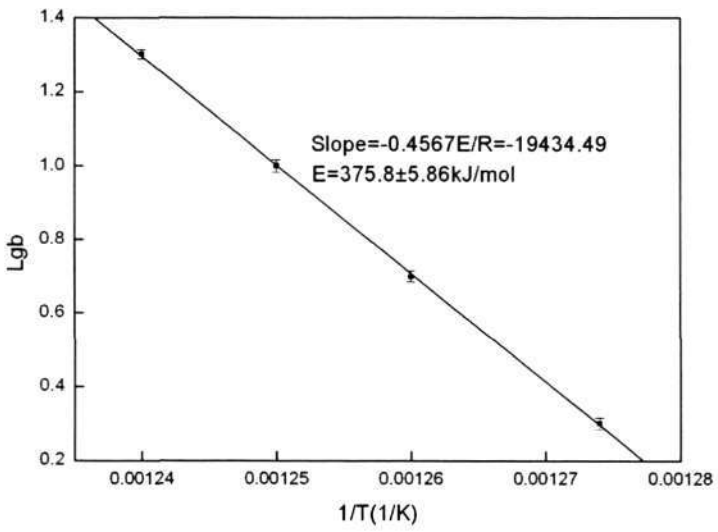

(a)

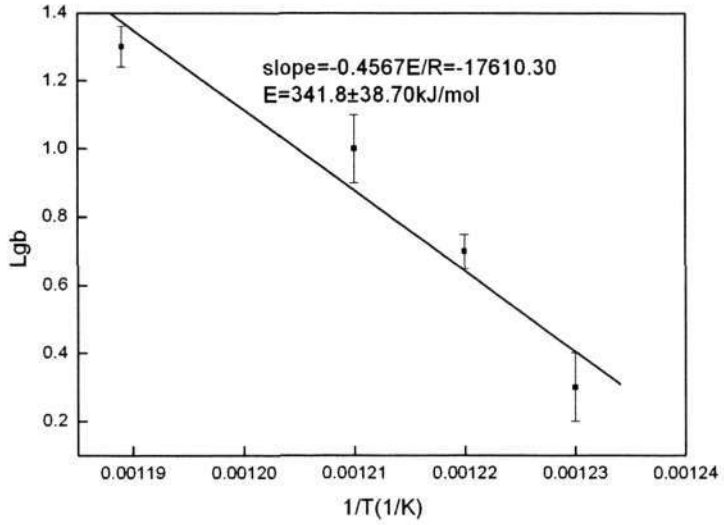

(b)

Figure 4. 2 Activation energy values obtained from DSC measurements for (a) the first peak and (b) second crystallization peak for a $Fe_{77.5}Si_{13.5}B_9$ alloy

The structural analysis of the $Fe_{77.5}Si_{13.5}B_9$ alloy as determined by XRD techniques will be described in the following section.

4.2.2 Structural Analysis

In this section the structural analysis of the $Fe_{77.5}Si_{13.5}B_9$ alloy after annealing at various temperatures and holding time will be described. The XRD results for samples after annealed at 490 °C for 1 h, 8 h and 20 h are shown in Figure 4. 3. The phase formation after annealing at 550 °C for 30 min, 1 h, 4 h, 8 h, 16 h and 24 h is shown in Figure 4. 4, the results after annealing at 420 °C, 490 °C, 500 °C, 515 °C, 550 °C, 600 °C and 640 °C for 1 h are shown in Figure 4. 5. The Fe-Si phase is found to be the primary

crystallization product, the formation of the Fe_3B phase indicated the occurrence of secondary crystallization, subsequently, Fe_3B decomposed to Fe_2B and α-Fe phases.

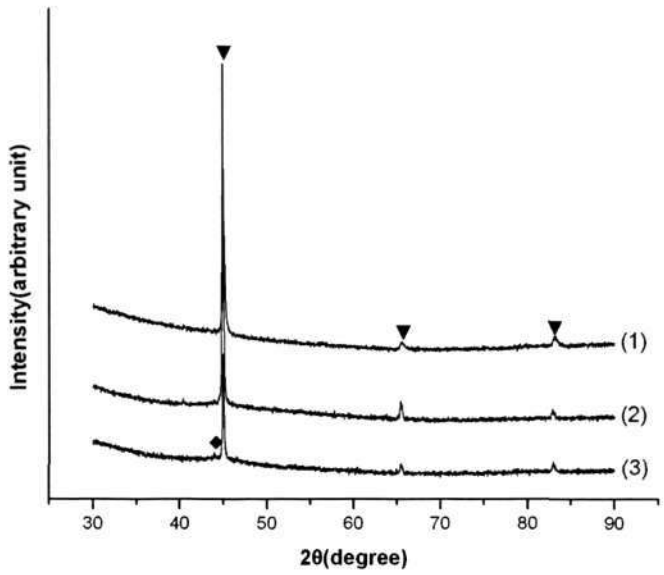

Figure 4. 3 XRD results for the $Fe_{77.5}Si_{13.5}B_9$ alloy heat treated at 490 °C for different holding time: (1)1 h, (2) 8 h and (3) 20 h: Fe-Si (▼), Fe_3B (♦)

The phases formed after the alloy was heat treated at 490 °C for various annealing times of 1 h, 8 h and 20 h were studied by XRD, the results showed that the Fe-Si phase continued to be the dominant phase as the annealing time was increased from 1 h to 20 h. The Fe_3B phase did not appear until 20 h of annealing time.

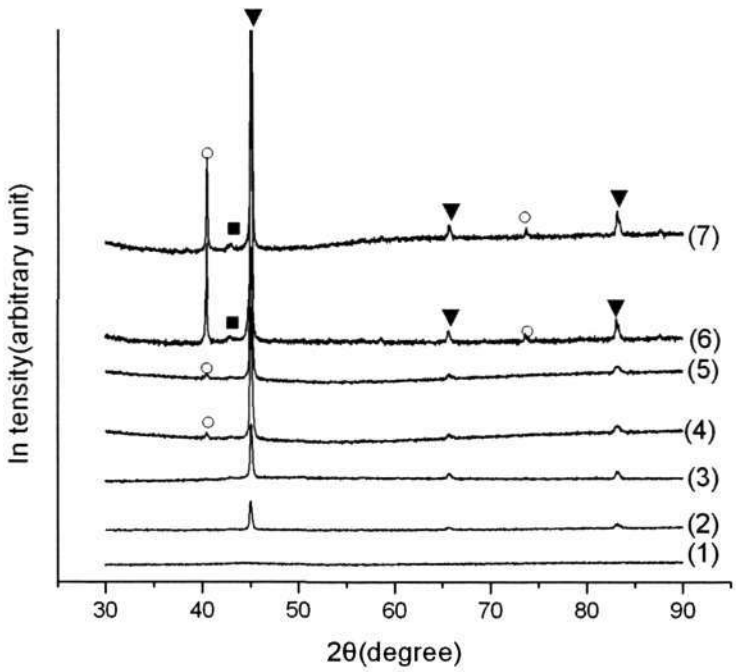

Figure 4. 4 XRD results for the $Fe_{77.5}Si_{13.5}B_9$ alloy heat treated at 550 °C for different holding time: (1) 5 min, (2)30 min, (3)1 h, (4)4 h, (5)8 h, (6)16 h and (7)24 h: Fe-Si (▼), Fe_2B (■) and Fe_3B (○)

From Figure 4. 4 it was observed that the alloy was still amorphous after heat treatment at 550 °C for 5 min, crystallization occurred after annealing for 30 min. The Fe-Si phase was again the dominant phase during the primary crystallization at this temperature until 4 h when the Fe_3B phase was identified, indicating the initiation of secondary crystallization. After the annealing was conducted for 16 h the Fe_2B phase was observed, it was formed by the decomposition of the Fe_3B phase.

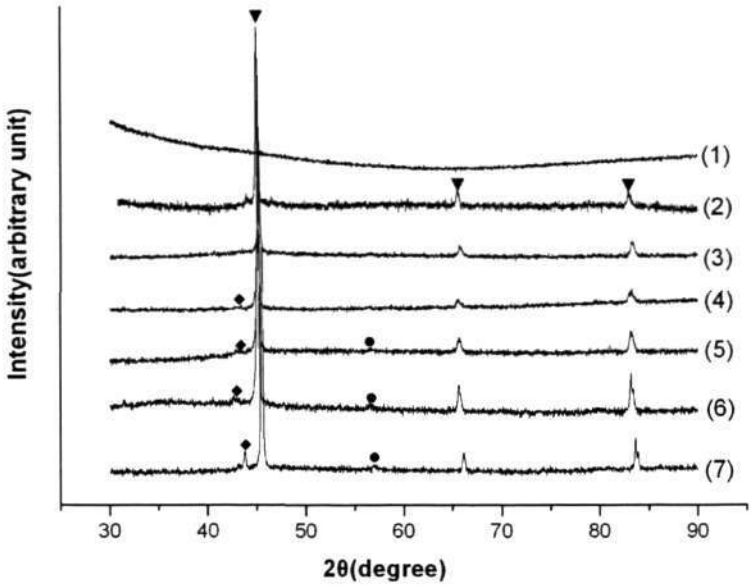

Figure 4. 5 XRD results for the $Fe_{77.5}Si_{13.5}B_9$ alloy heat treated at different temperatures for 1 h: (1)420 °C, (2)490 °C , (3)500 °C , (4)515 °C , (5)550 °C ,(6)600 °C , and (7)640 °C : Fe-Si (▼), Fe_3B(♦), Fe_2B(●)

The XRD results of the temperature dependence of phase formation after heat treatment for 1 h in the temperature range from 420 °C to 640 °C are shown in Figure 4. 5. These results showed that the Fe-Si phase formed during the first crystallization event at 490 °C while secondary crystallization products of the Fe_3B phase did not form until 550 °C.

By comparing these three different temperatures and annealing times it was observed that Fe-Si is the product of primary crystallization. Secondary crystallization occurred at 490 °C for annealing times up to 20 h. For an annealing temperature of 550 °C annealing time of just 1 h resulted in the secondary crystallization, i.e., the formation of the Fe_3B phase.

Morphological observation after crystallization was conducted by TEM techniques. By combining the structural analysis and microstructural observations, the crystallization behavior of the $Fe_{77.5}Si_{13.5}B_9$ alloy can be described.

4.2.3 Crystallization behavior

In this section the crystallization behavior of the $Fe_{77.5}Si_{13.5}B_9$ alloy will be described by combining the structural analysis in the previous section and the morphological observations of the annealed alloy by TEM techniques.

TEM micrographs and the corresponding SADP of the microstructure are presented in Figure 4. 6 which shows for the first time that the primary crystallization product has an unusual dendritic morphology, each branch of the dendrite is composed of independent closely spaced crystals, the spacing between crystals is of the order of several nanometers. Such a solid state dendritic morphology has not been reported earlier in this alloy system. Interestingly, these individual crystals follow the general contours of a continuous dendritic morphology showing that diffusion field effects are predominant in the formation of the dendritic microstructure. These dendrites were confirmed by SADP analysis to belong to the Fe-Si phase. During dendrite formation, solute rejection occurred at the dendrite: matrix interface. Hence, EDS was used to measure the compositions of Fe and Si near the interface between the crystal and the matrix (the composition of B cannot be determined from EDS measurements). The spots in Figure 4. 7 were selected for measurements, Cliff-Lorimer corrections were performed and the results are tabulated in Table 4.1[78]. It was found that the Si concentration in the matrix

was about 3 at% higher than the concentration within the dendritic crystals, which indicated solute rejection of Si during dendrite formation. B element mapping by EELS was conducted to identify the distribution of boron during crystallization (Figure 4. 8). The white area indicated regions with higher B concentration and the dark areas indicated regions with lower B concentration distribution, regions around the dendrite are clearly richer in B compared with the region within the dendrite.

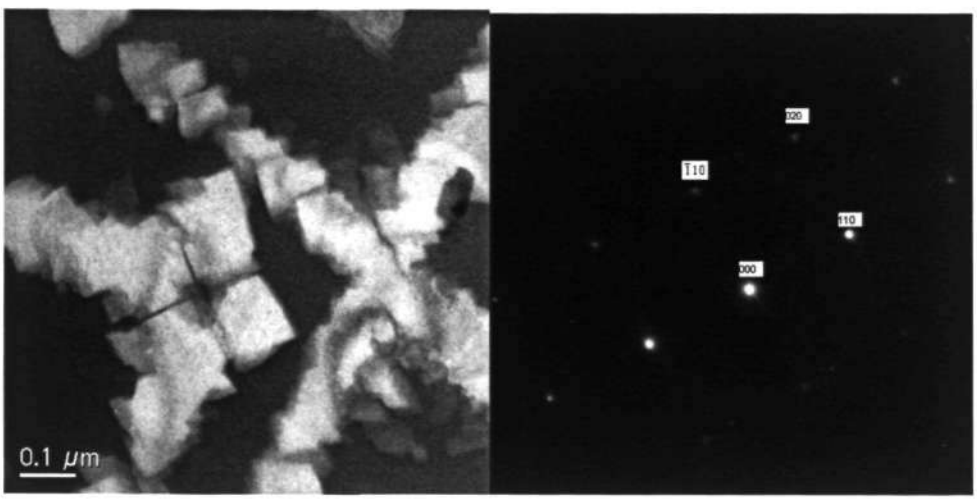

(a) (b)

Figure 4. 6 (a) BF TEM micrograph and (b) corresponding SADP of the $Fe_{77.5}Si_{13.5}B_9$ alloy annealed at 490 °C for 1 h, showing that the dendrite is a bcc Fe-Si phase, zone axis: [001]

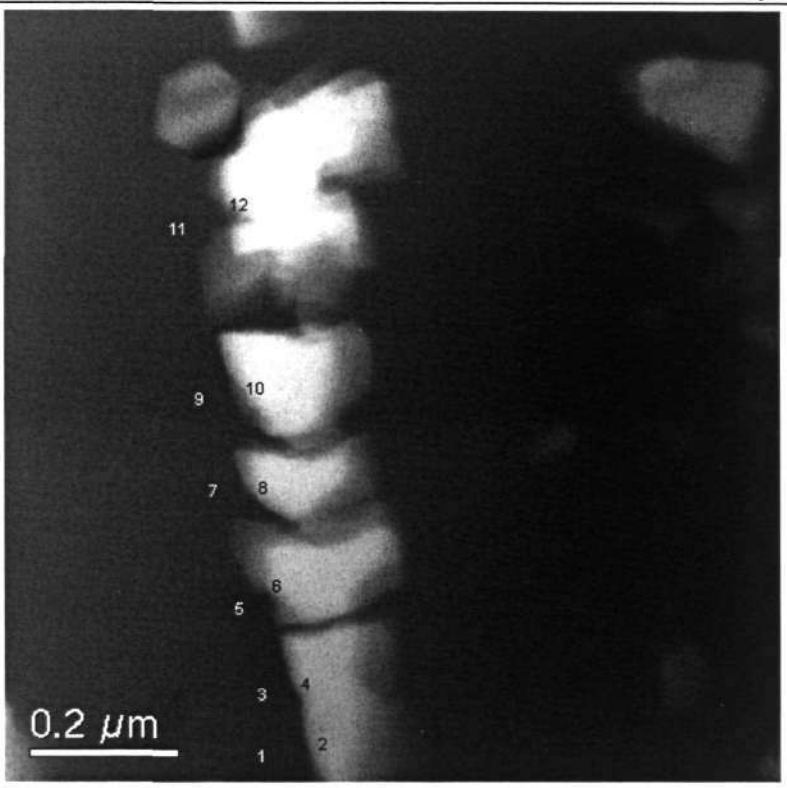

Figure 4. 7 EDS measurements for spots from 1 to 13 at the interface of the crystal and the matrix: the odd numbers are for the matrix along the interface, while the even numbers are the crystal along the interface

Table 4. 1 EDS measurement result corresponding to Figure 4. 7

Element	1	2	3	4	5	6	7	8	9	10	11	12
Fe(at%)	85	87.6	85.1	88.4	84.7	88	85.7	87.3	84.5	88.2	85.2	87.8
Si(at%)	15.0	12.4	14.9	11.6	15.3	12	14.3	12.7	15.5	11.8	14.8	12.2

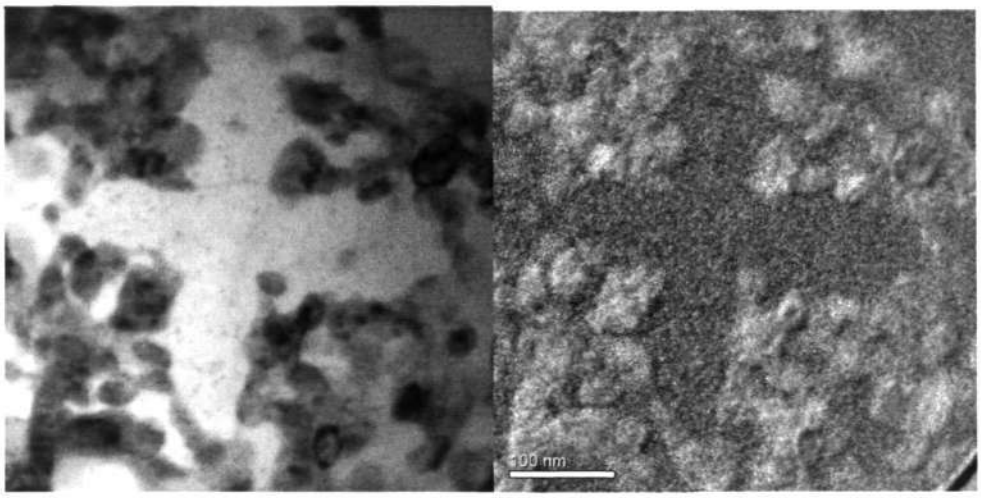

Figure 4. 8 B element mapping for the Fe-Si-B alloy after heat treatment at 550 °C for 30 min

Figure 4. 9 to Figure 4. 13 show the products of secondary crystallization. Secondary crystallization occurred not only between the dendrite branches but also between the closely spaced crystals (shown by arrows in Figure 4. 9). Secondary crystallization resulted in a striped structure consisting of the Fe_3B phase and a Fe-Si phase with a B2 ordered structure (Figure 4. 10), the existence of this B2 structure has not been reported earlier. After secondary crystallization was completed at 640 °C for 1 h, two morphologies were observed: large crystals (dark arrow in Figure 4. 11) and a striped sinuous morphology (bright arrow in Figure 4. 11). Bright field and dark field images of this striped morphology are presented in Figure 4. 12. This sinuous striped morphology was different from the lamellar structure observed in secondary crystallization products in Fe-Si-B alloys with more B [21]. Large crystals about 400 nm (Figure 4. 13) were also observed and found to belong to the b.c.c Fe-Si phase.

Figure 4. 9 BF TEM micrograph of the $Fe_{77.5}Si_{13.5}B_9$ alloy annealed at 490 °C for 20 h

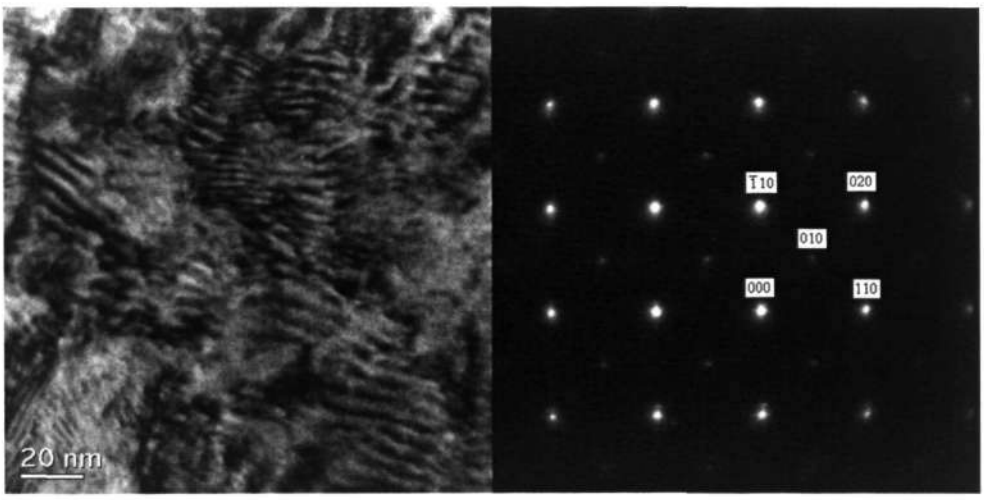

(a) (b)

Figure 4. 10 (a) The striped microstructure and (b) corresponding SADP of the $Fe_{77.5}Si_{13.5}B_9$ alloy annealed at 490 °C for 20 h: SADP showing the Fe-Si phase with B2 ordered structure, zone axis: [100]

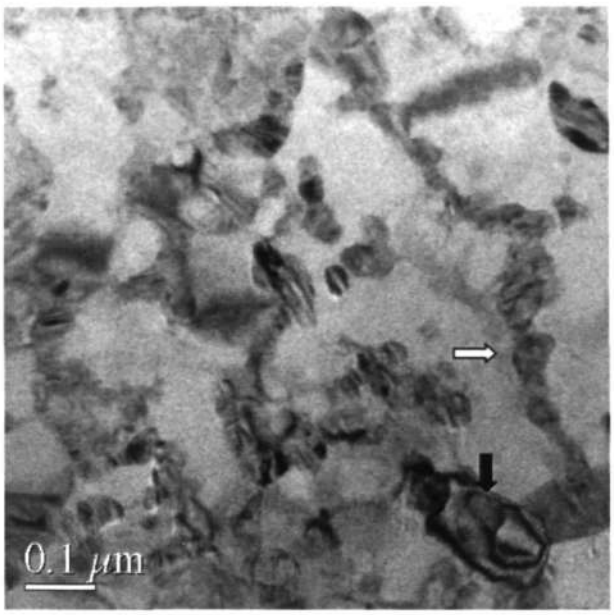

Figure 4. 11 BF TEM micrograph of the products at the end of crystallization of the $Fe_{77.5}Si_{13.5}B_9$ alloy annealed at 640 °C for 1 h

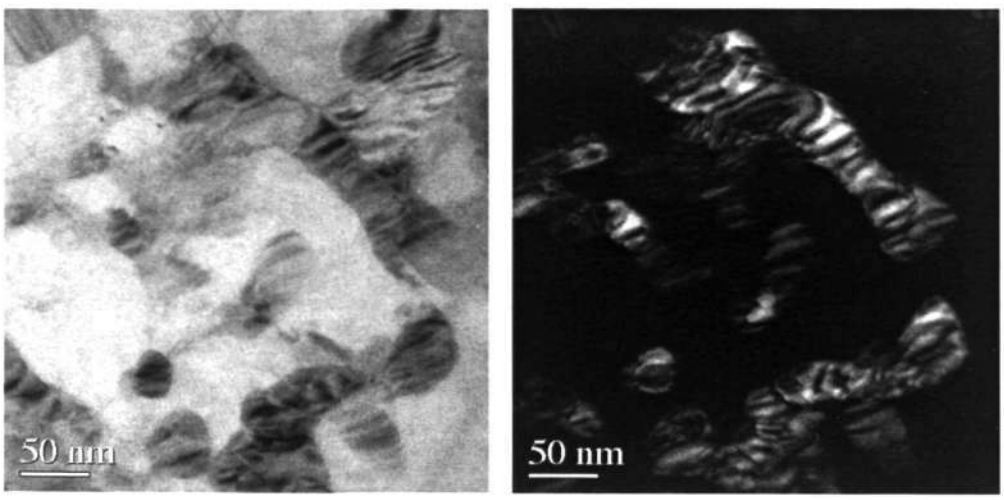

(a) (b)

Figure 4. 12 (a) BF and corresponding (b) DF TEM micrographs of the striped microstructure of the $Fe_{77.5}Si_{13.5}B_9$ alloy annealed at 640 °C for 1 h

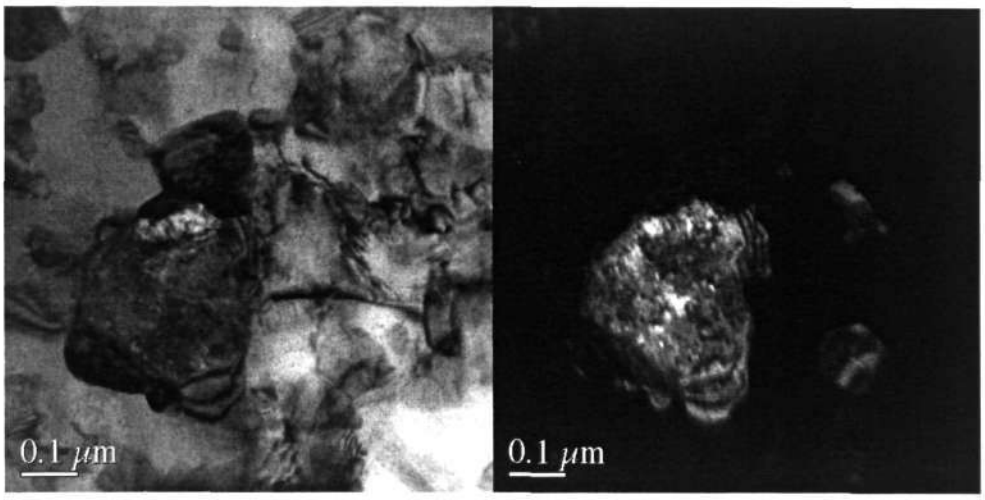

(a) (b)

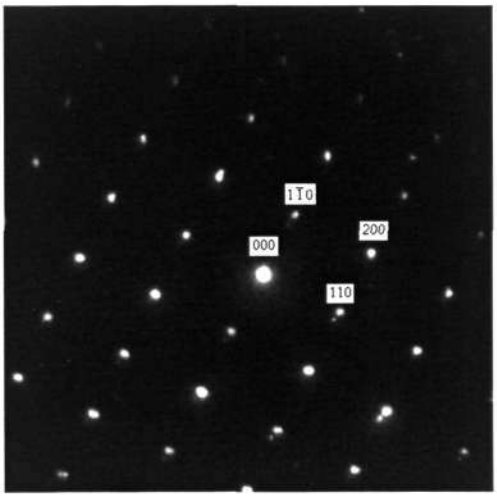

(c)

Figure 4. 13 TEM micrograph of a large crystal observed in a $Fe_{77.5}Si_{13.5}B_9$ alloy annealed at 640 °C for 1 h: (a) bright field image (b) dark field image (c) SADP showing that the crystal belonging to the b.c.c. α-Fe-Si phase: zone axis: [001]

The following section will deal with in-situ hot stage TEM observation of crystallization of this alloy, the process of dendrite formation will be described.

4.2 In-situ hot stage TEM observation of crystallization of the Fe-Si-B alloy

In this section, observation of crystallization occurring during in-situ hot stage TEM is described for the initially amorphous Fe-Si-B alloy. Interestingly, an equiaxed to dendritic morphological transition was observed for the first time after the specimen was heated at 500 °C between 300 s to 480 s(white arrow in Figure 4. 14 to Figure 4. 18). An equiaxed crystal about 10 nm in size formed after annealing for 300 s(Figure 4. 14). Subsequently four perpendicular dendrite branches with a length up to 45 nm were observed (Figure 4. 15). As the crystallization time was increased to 480 s dendritic growth resulted in branches extending to 200 nm (Figure 4. 18).

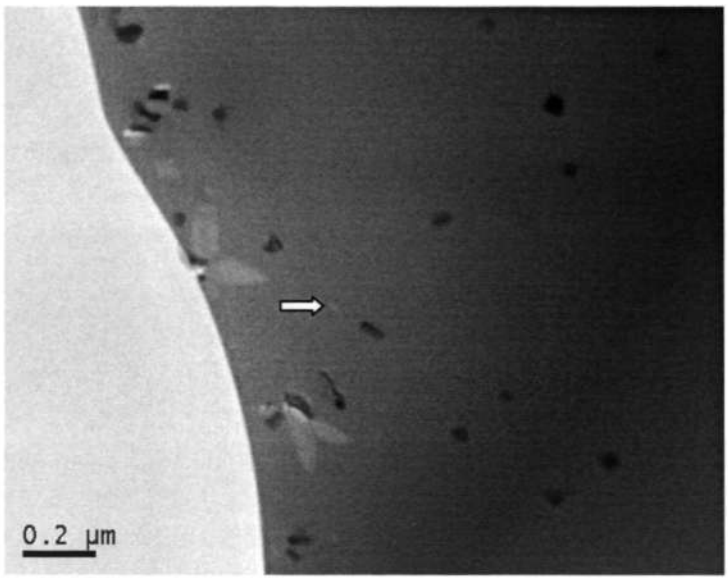

Figure 4. 14 BF TEM micrograph of the $Fe_{77.5}Si_{13.5}B_9$ alloy annealed at 500 °C for 300 s

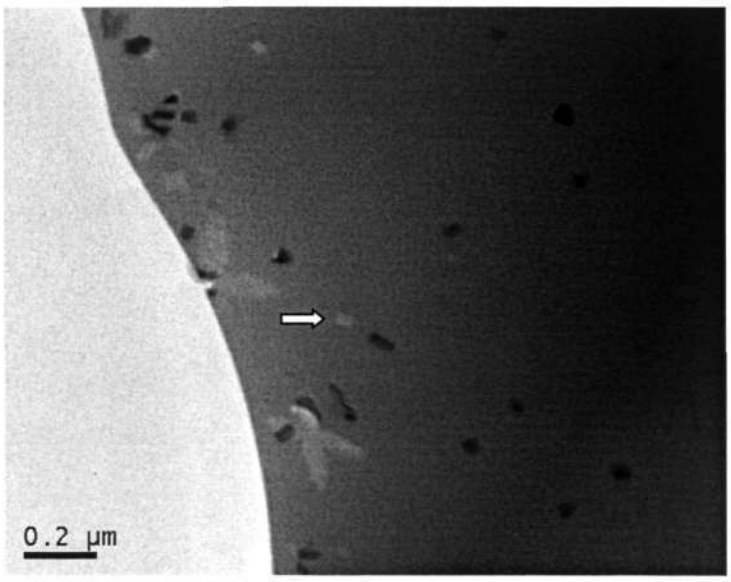

Figure 4. 15 BF TEM micrograph of the $Fe_{77.5}Si_{13.5}B_9$ alloy annealed at 500 °C for 306 s

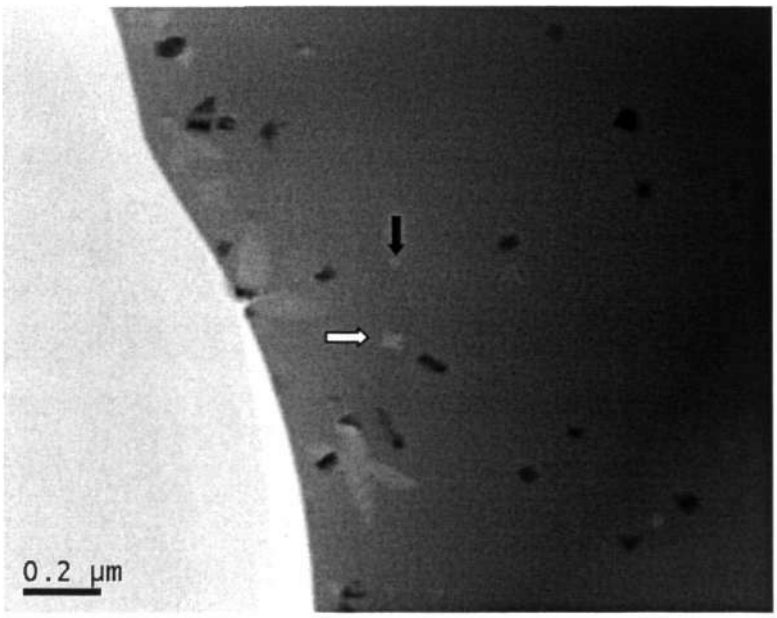

Figure 4. 16 BF TEM micrograph of the $Fe_{77.5}Si_{13.5}B_9$ alloy annealed at 500 °C for 312 s

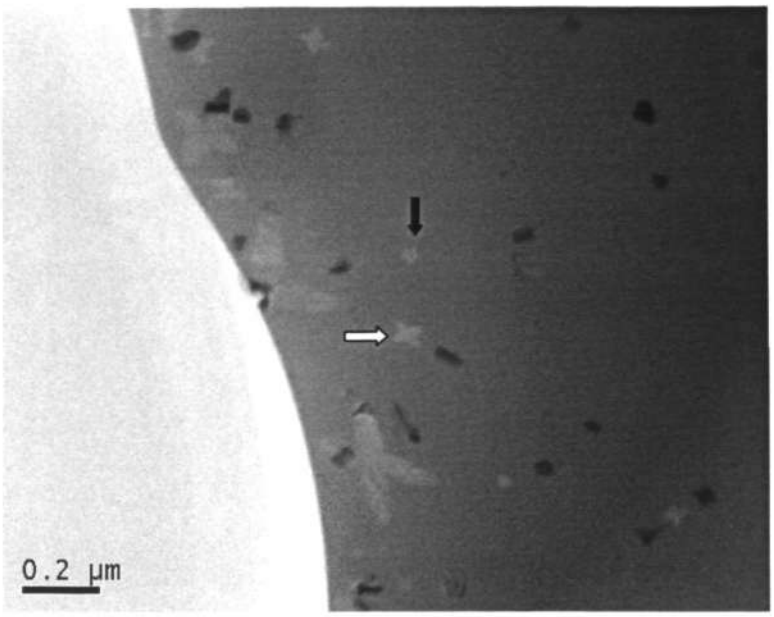

Figure 4. 17 BF TEM micrograph of the $Fe_{77.5}Si_{13.5}B_9$ alloy annealed at 500 °C for 360 s

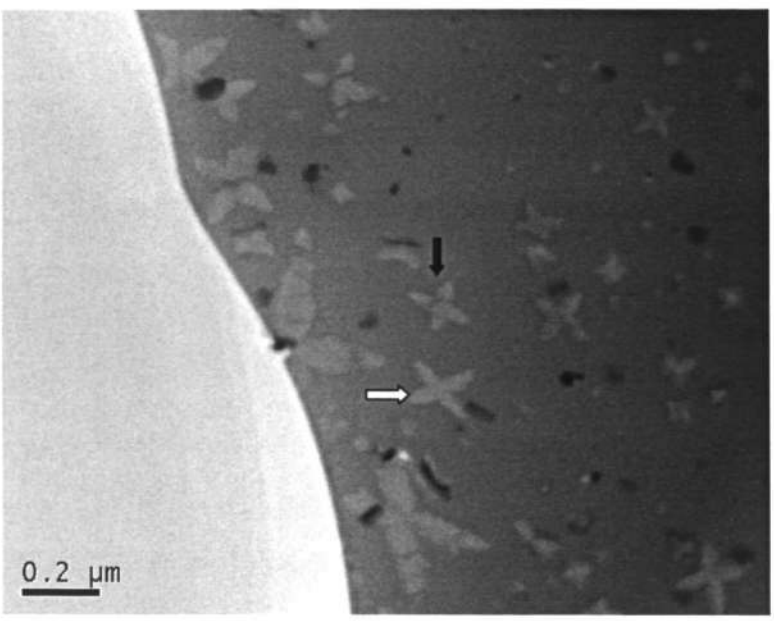

Figure 4. 18 BF TEM micrograph of the $Fe_{77.5}Si_{13.5}B_9$ alloy annealed at 500 °C for 480 s

The next section will describe the thermal properties, structural analysis and crystallization behavior of the copper containing $Fe_{76.5}Si_{13.5}B_9Cu_1$ alloy. It was found that

1 at% Cu alloying addition in the $Fe_{76.5}Si_{13.5}B_9Cu_1$ alloy has a large effect on the thermal properties, phase formation and microstructure after crystallization.

4.3 $Fe_{76.5}Si_{13.5}B_9Cu_1$ alloy

In this section the thermal analysis, structural analysis and crystallization behavior of the $Fe_{76.5}Si_{13.5}B_9Cu_1$ alloy will be described [86]. Compared with the $Fe_{77.5}Si_{13.5}B_9$ alloy 1 at% Cu alloying addition induces the crystallization at lower temperatures and changes the microstructure from the dendritic morphology observed in the Fe-Si-B alloy to a spheroidal morphology with rough interfaces.

4.3.1 Thermal Analysis

By means of DSC the crystallization temperatures of the $Fe_{76.5}Si_{13.5}B_9Cu_1$ alloy were measured at heating rates of 2, 5, 10, and 20 K/min, as shown in Figure 4. 19. The calculated activation energy of crystallization is shown in Figure 4. 20. Two exothermic peaks were observed. At a heating rate of 10 K/min the first crystallization peak in the case of the Fe-Si-B-Cu alloy occurs at 466 °C, lower than that observed in the Fe-Si-B alloy. At the same time, Cu alloying addition resulted in an increase in the gap between the first peak and second peak compared with the corresponding DSC curve of the Fe-Si-B alloy (Figure 4. 1). The calculated activation energy of primary and secondary crystallization of the $Fe_{76.5}Si_{13.5}B_9Cu_1$ alloy was 260±20.8 kJ/mol and 257±30.4 kJ/mol respectively. Compared with the values of the $Fe_{77.5}Si_{13.5}B_9$ alloy, 1 at% Cu alloying addition reduced the activation energy for crystallization.

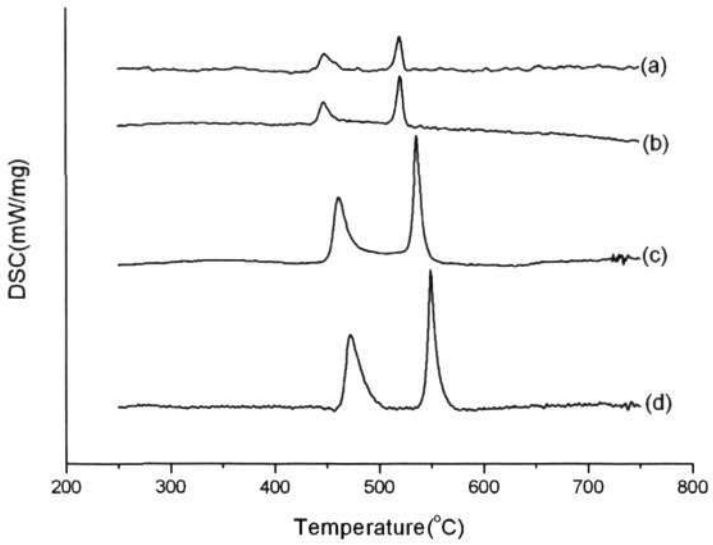

Figure 4. 19 DSC results for the Fe-Si-B-Cu alloy at heating rates of: (a)2 K/min, (b)5 K/min, (c)10 K/min and (d)20 K/min

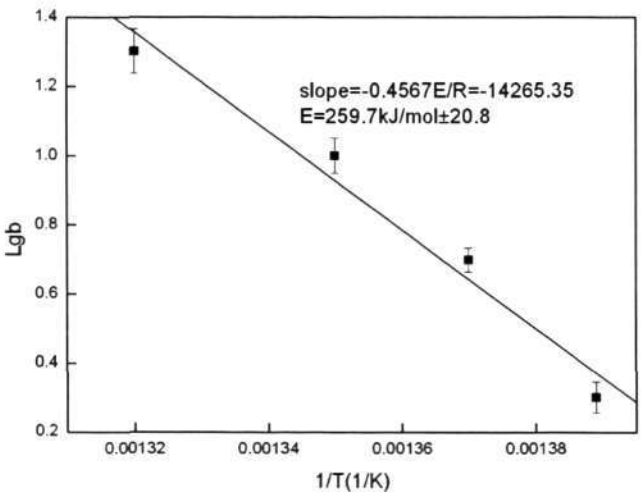

(a)

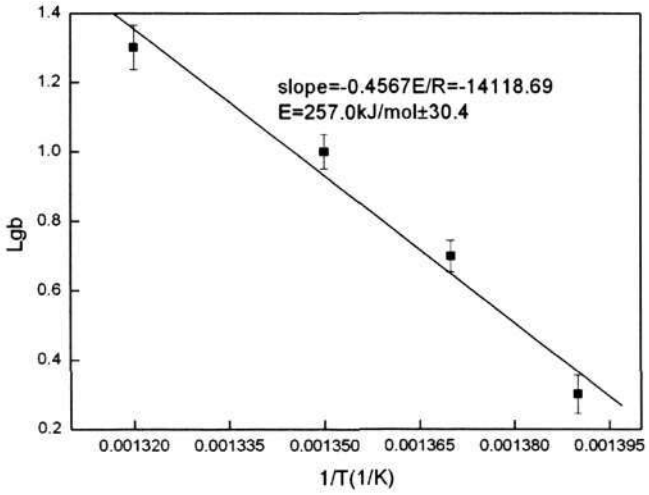

(b)

Figure 4. 20 Activation energy obtained from DSC measurement for the first peak (a) and second crystallization peak (b) for a $Fe_{76.5}Si_{13.5}B_9Cu_1$ alloy

The structural analysis of the $Fe_{76.5}Si_{13.5}B_9Cu_1$ alloy after heat treatment was conducted by XRD analysis and the results are described in the following section.

4.3.2 Structural Analysis

In this section the structural analysis of the $Fe_{76.5}Si_{13.5}B_9Cu_1$ alloy after annealing at various temperatures will be described. The phase formation after heat treatment at different temperatures: 420 °C, 490 °C, 500 °C, 515 °C, 550 °C, 600 °C, and 640 °C for 1 h was identified by XRD techniques and the results are shown in Figure 4. 21. These temperatures were selected based on the DSC results presented earlier.

With Cu alloying additions primary crystallization occurred at lower temperatures: 420 °C,

compared with 490 °C in the Fe-Si-B alloy. The Fe-Si phase was identified in samples annealed at 420 °C and the Fe_3B phase formed at 500 °C. This showed that both the primary and secondary crystallization temperatures in the case of the Fe-Si-B-Cu alloy are lower than those of the Fe-Si-B alloy, which is consistent with the DSC results.

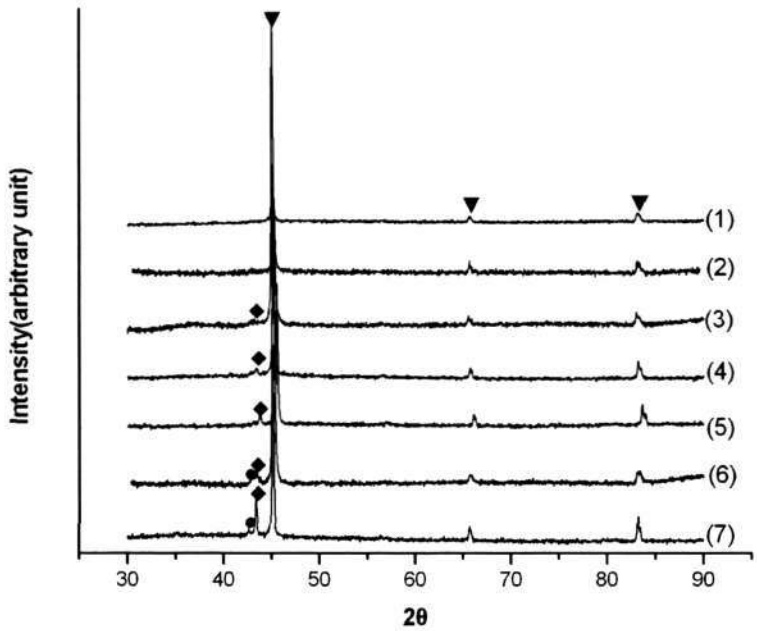

Figure 4. 21 XRD results for $Fe_{76.5}Si_{13.5}B_9Cu_1$ alloy heat treated at different temperatures for 1 h: (1)420 °C, (2)490 °C, (3)500 °C, (4)515 °C, (5)550 °C, (6)600 °C, and (7)640 °C: Fe-Si(▼), Fe_3B(♦), Fe_2B(●)

The crystallization behavior of the $Fe_{76.5}Si_{13.5}B_9Cu_1$ alloy will be described in the following section by combining the structural analysis in this section and with TEM based microstructural observations.

4.3.3 Crystallization behavior

This section deals with TEM observations of the crystallization behavior of the $Fe_{76.5}Si_{13.5}B_9Cu_1$ alloy. In the case of the Fe-Si-B-Cu alloy, the microstructural evolution was significantly different from that of the Fe-Si-B alloy; instead of the dendritic morphology observed in the Fe-Si-B alloy, spheroidal crystals with rough interfaces less than 100 nm in size were observed as the product of primary crystallization (Figure 4. 22). Figure 4. 23 (a) shows a higher magnification micrograph of spheroidal crystals about 50nm in size, the corresponding SADP (Figure 4. 23 (b)) was indexed as the b.c.c. Fe-Si phase which is consistent with the XRD data presented identification in Figure 4. 21. At a higher annealing temperature of 490 °C, a higher crystal density was observed and spheroidal crystals larger than 100 nm in size were observed (Figure 4. 24). At 500 °C secondary crystallization occurred with the formation of a striped structure of the Fe_3B phase, as indicated by the arrow in Figure 4. 25. In order to obtain a better understanding of the striped microstructure of the Fe_3B phase, BF and corresponding DF micrographs were obtained (Figure 4. 26). These striped products formed from the remaining amorphous matrix. At the same time, a higher volume fraction of the Fe-Si phase, which formed from the amorphous matrix during secondary crystallization was observed in the form of crystals larger than 200 nm. The crystal structure was found by SADP analysis to belong to the DO_3 ordered structure (Figure 4. 27).

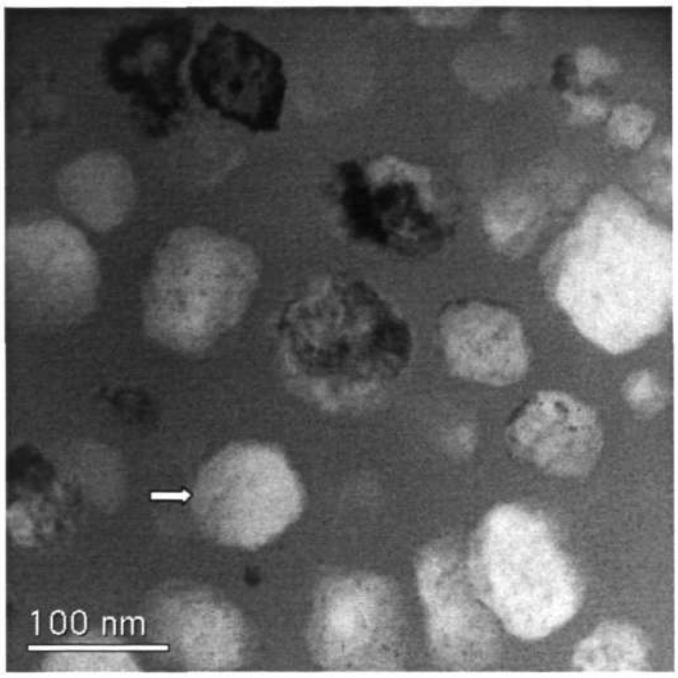

Figure 4. 22 BF TEM micrograph of Fe-Si-B-Cu alloy heat treatment at 420 °C for 1 h

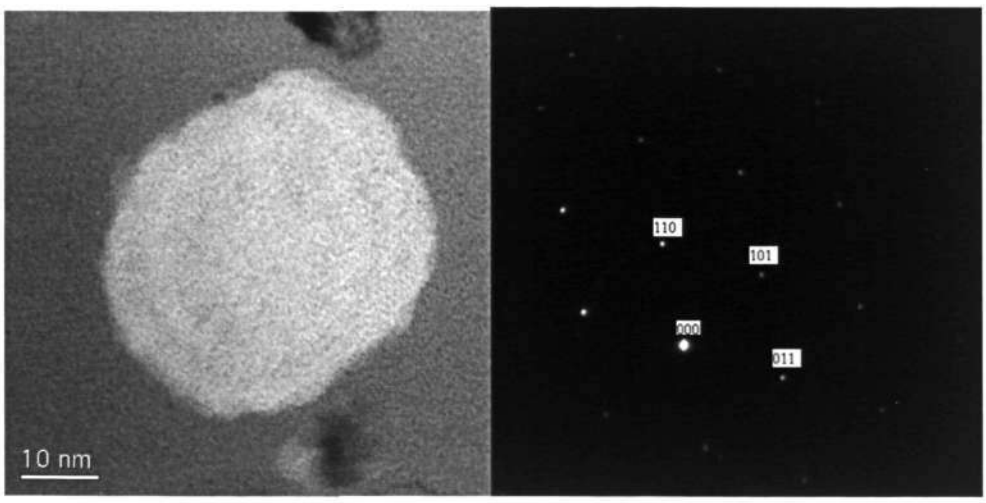

(a) (b)

Figure 4. 23 (a) BF TEM micrograph and SADP(b) of the crystal indicated by arrow in Figure 4. 22: zone axis: $[1\bar{1}1]$

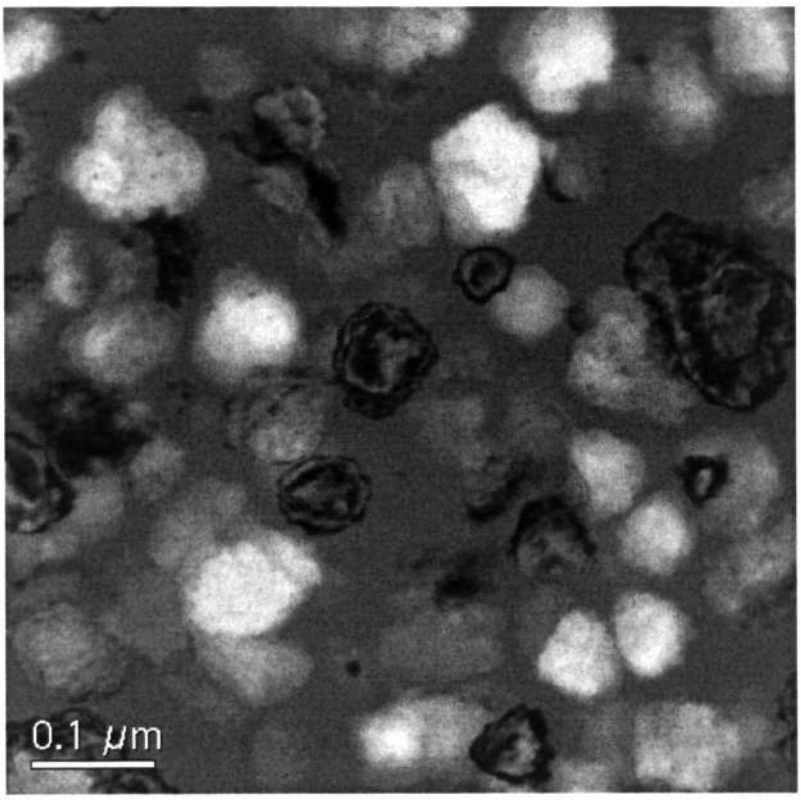

Figure 4. 24 Bright field micrograph of Fe-Si-B-Cu alloy heat treatment at 490 ^{o}C for 1 h

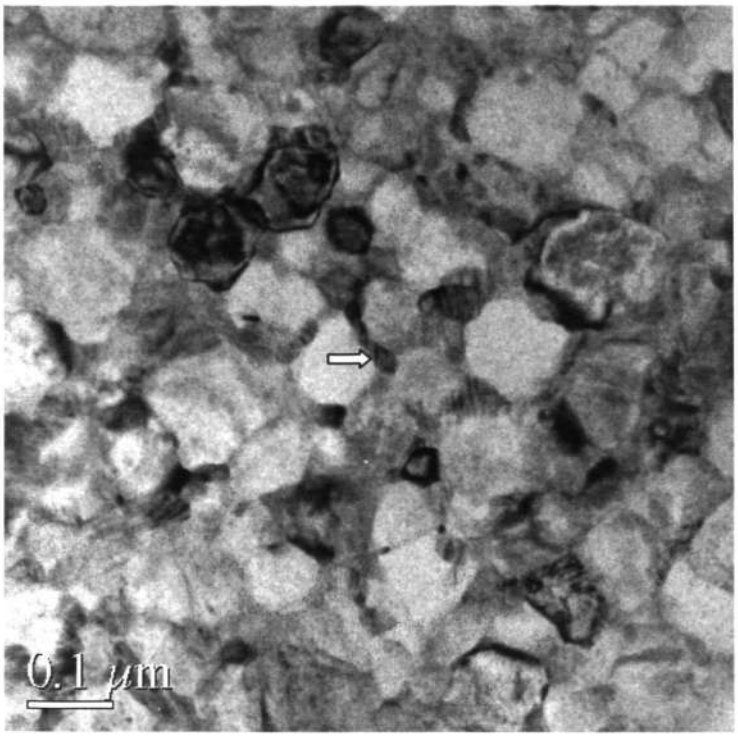

Figure 4. 25 Bright field micrograph of the Fe-Si-B-Cu alloy heat treatment at 640 °C for 1 h

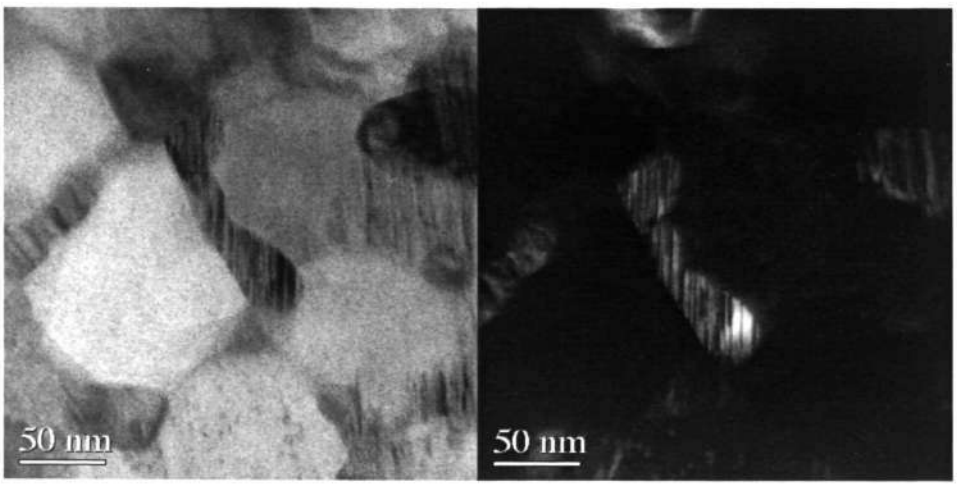

(a) (b)

Figure 4. 26 BF (a) and DF (b) TEM micrographs of the striped morphology indicated by arrow in Figure 4. 25

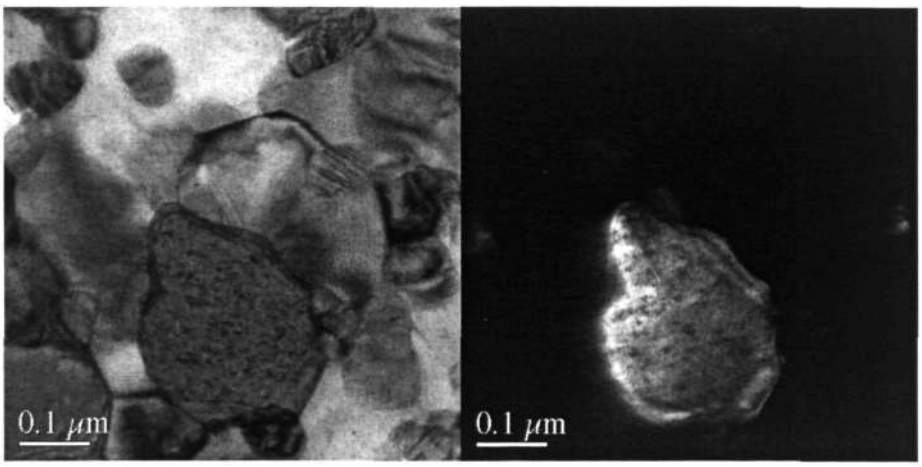

(a) (b)

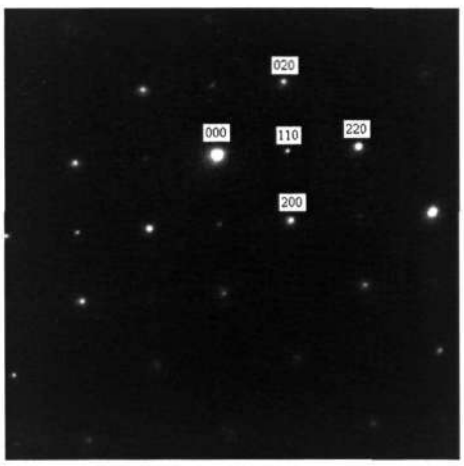

(c)

Figure 4. 27 TEM micrograph of the crystal from the Fe-Si-Cu-B alloy annealed at 640 °C for 1 h: (a) bright field image (b) dark field image (c) SADP: zone axis:[$00\bar{1}$]

The next section will deal with in-situ hot stage TEM observation of the Fe-Si-B-Cu alloy, the formation of the spheroidal crystals was directly observed.

4.4 In-situ hot stage TEM observation of the Fe-Si-B-Cu alloy

In-situ hot stage TEM observations of the Fe-Si-B-Cu alloy were conducted. As observed

in Figure 4. 28 b.c.c. Fe-Si crystals about 10 nm in size appear at about 400 °C. With increasing time, both the number density and size of the crystals increased (Figure 4. 29). Figure 4. 30 to Figure 4. 33 shows this formation and growth of a spheroidal crystal (indicated by arrows), the morphology is significantly different from the typical dendrite morphology observation in the Fe-Si-B alloy. After 600 s of heating at 450 °C crystals larger than 100 nm were observed, interfacial instability caused the crystals to develop a rough, wavy interface (arrow in Figure 4. 34).

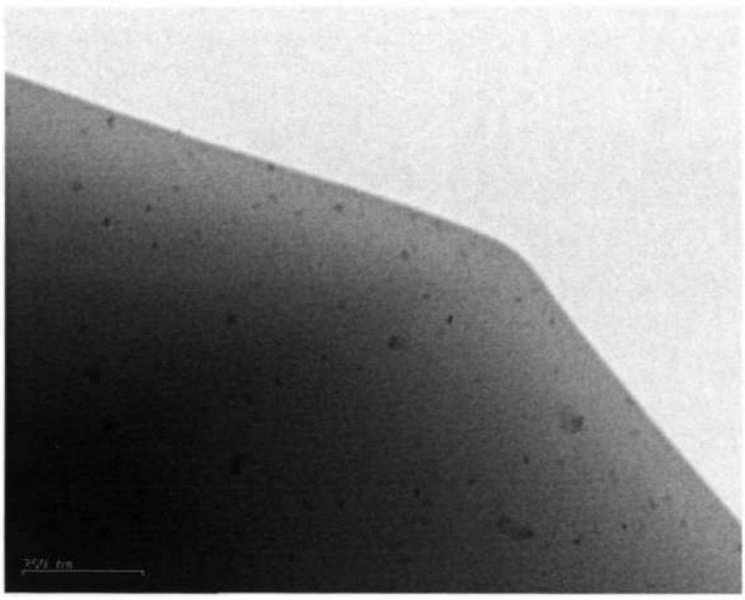

Figure 4. 28 BF TEM micrograph of the $Fe_{76.5}Si_{13.5}B_9Cu_1$ alloy annealed at 400 °C for 260 s

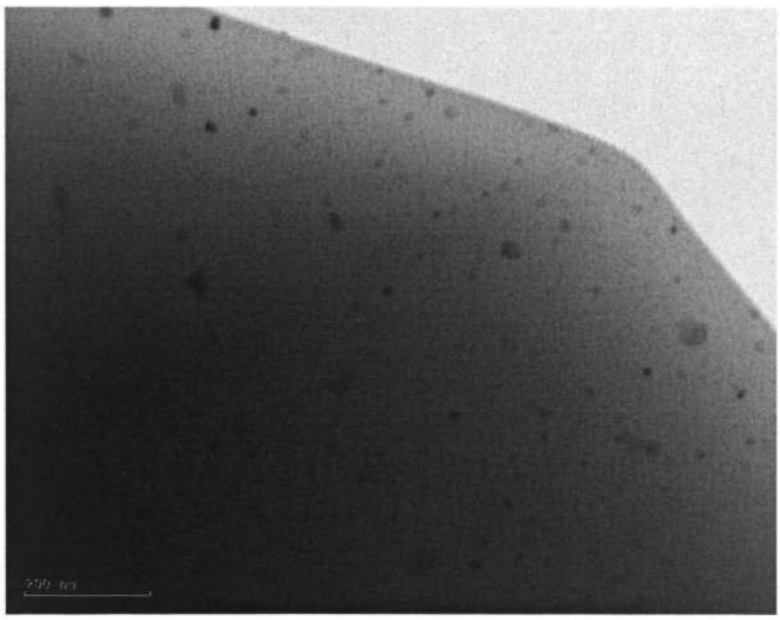

Figure 4. 29 BF TEM micrograph of the $Fe_{76.5}Si_{13.5}B_9Cu_1$ alloy annealed at 400 °C for 300 s

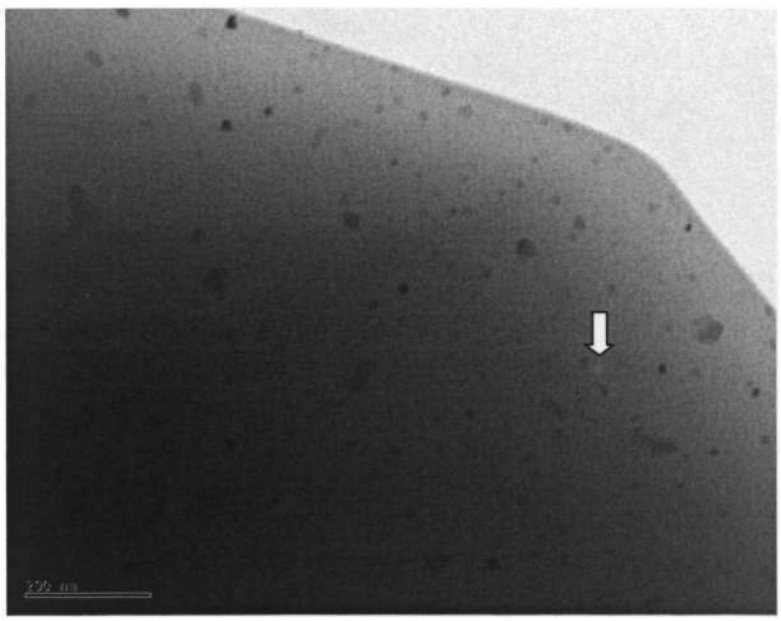

Figure 4. 30 BF TEM micrograph of the $Fe_{76.5}Si_{13.5}B_9Cu_1$ alloy annealed at 400 °C for 306 s

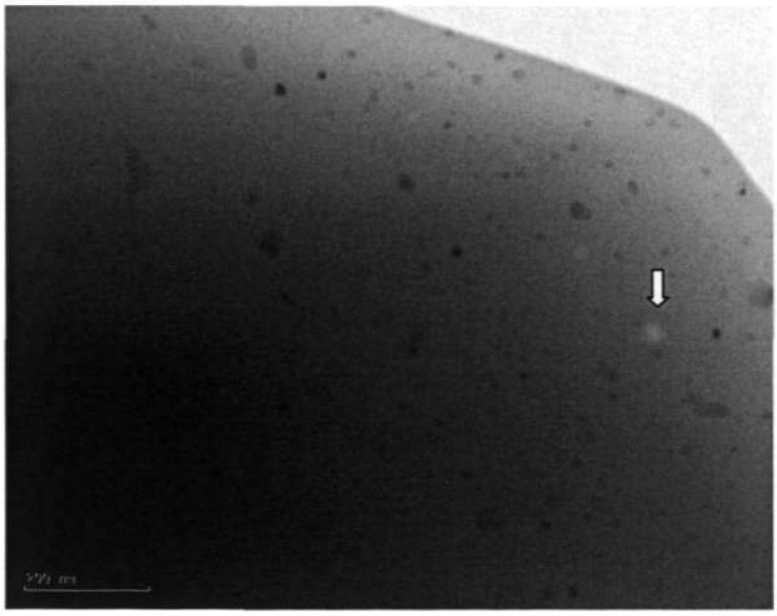

Figure 4. 31 BF TEM micrograph of the $Fe_{76.5}Si_{13.5}B_9Cu_1$ alloy annealed at 400 °C for 312 s

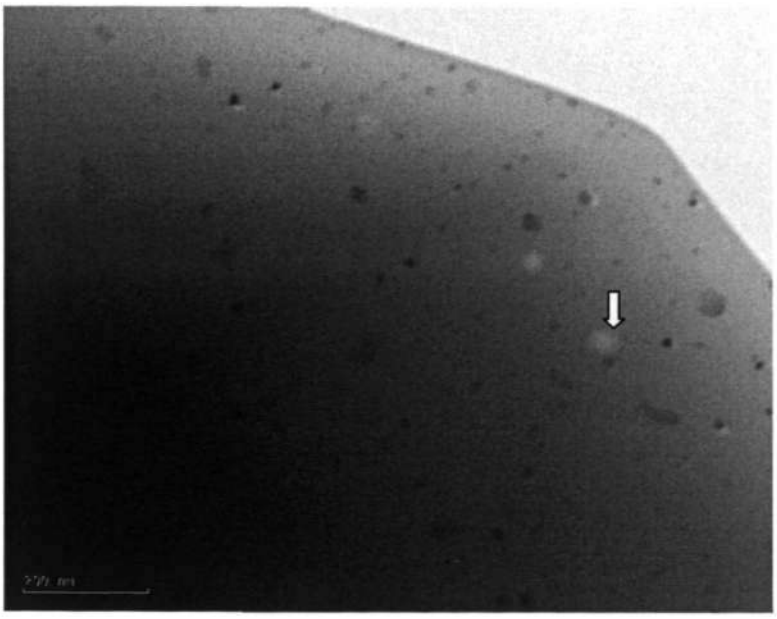

Figure 4. 32 BF TEM micrograph of the $Fe_{76.5}Si_{13.5}B_9Cu_1$ alloy annealed at 400 °C for 318 s

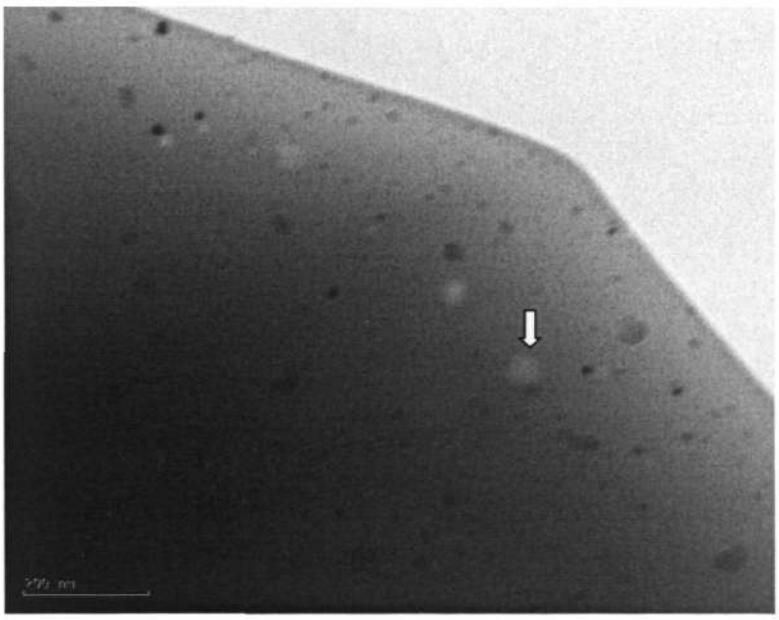

Figure 4. 33 BF TEM micrograph of the $Fe_{76.5}Si_{13.5}B_9Cu_1$ alloy annealed at 400 °C for 330 s

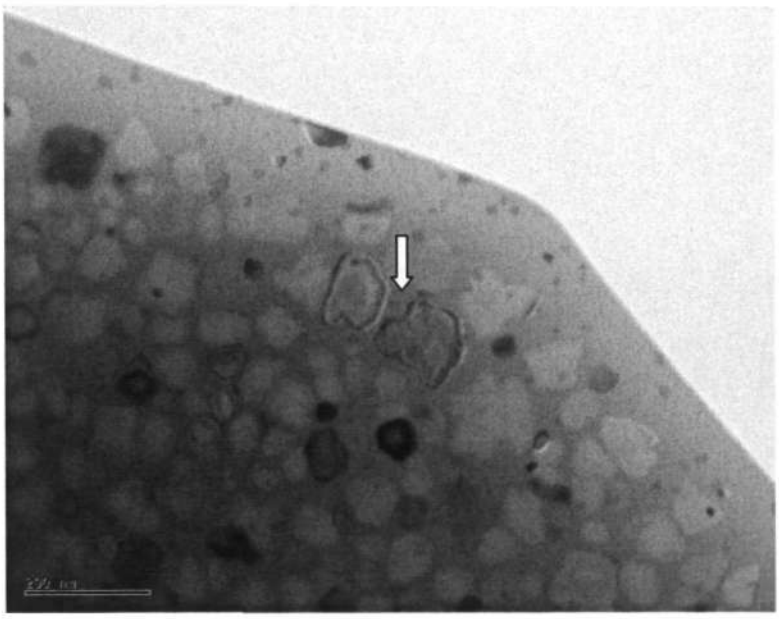

Figure 4. 34 BF TEM micrograph of the $Fe_{76.5}Si_{13.5}B_9Cu_1$ alloy annealed at 450 °C for 600 s

In order to describe the nucleation and crystal growth behavior during the crystallization

process, we measured the crystal density (N) and maximum crystal diameter of the b.c.c. Fe-Si phase after isothermal annealing at three temperatures. Figure 4. 35 and Figure 4. 36 show the nucleation density and maximum crystal diameter dependence on annealing time at 400 °C, 425 °C, 450 °C respectively. Interestingly, for different temperatures, crystal density increases rapidly in the initial stages, and tends to saturate. The crystals grow steadily, but the growth does not follow the parabolic growth law.

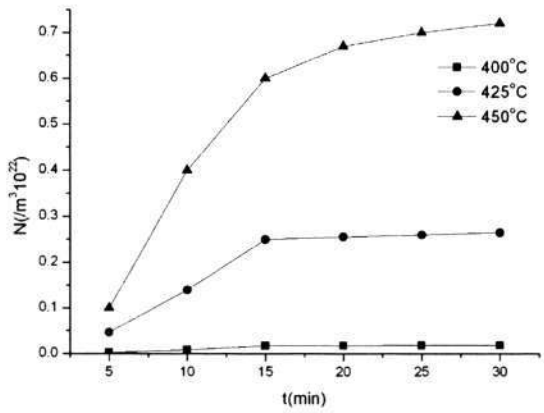

Figure 4. 35 Crystal density of the α-Fe-Si phase after isothermal annealing at three different temperatures

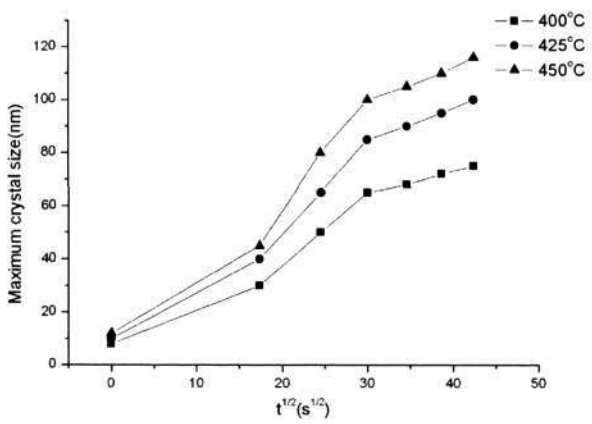

Figure 4. 36 Maximum crystal diameter of the α-Fe-Si phase after isothermal annealing at three different temperatures

The following section deals with the thermal analysis, structural analysis and crystallization behavior of the Nb containing $Fe_{74.5}Si_{13.5}B_9Nb_3$ alloy. The additions of 3 at% Nb alloying addition had a significant influence on the thermal, structural and crystallization behavior.

4.5 $Fe_{74.5}Si_{13.5}B_9Nb_3$ alloy

In this section the effect of 3 at% Nb in the Fe-Si-B alloy on the thermal properties, structural analysis and crystallization behavior will be described[87]. It was found that the additions of 3 at% Nb changed the mechanism of crystallization from primary crystallization in the Fe-Si-B alloy to eutectic crystallization in the Fe-Si-B-Nb alloy.

4.5.1 Thermal Analysis

By means of DSC techniques the crystallization temperatures of the $Fe_{76.5}Si_{13.5}B_9Nb_3$ alloy were measured at heating rates of 2, 5, 10, and 20 K/min (Figure 4. 37). The calculated activation energy for crystallization is shown in Figure 4. 38. At a heating rate of 10 K/min the DSC curve exhibited only one exothermic peak at 589 °C, this result is different from the two peaks observed in the DSC curves of Fe-Si-B and Fe-Si-B-Cu alloys. In the Fe-Si-B alloy as the heating rate increased from 2 K/min to 20 K/min the peak become sharper while with Nb alloying addition, the peak is highest at a heating rate of 10 K/min. The value of the activation energy of crystallization is 549±35.7 kJ/mol, higher than that of the Fe-Si-B and Fe-Si-B-Cu alloys.

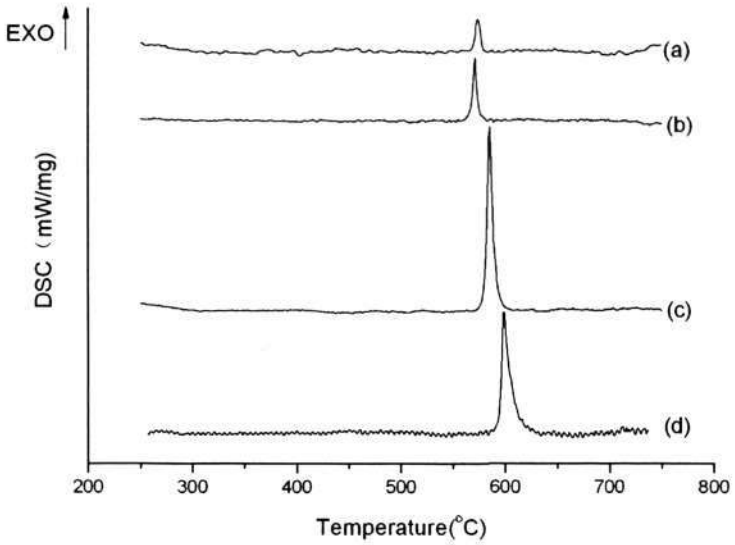

Figure 4. 37 DSC results for the Fe-Si-B-Nb alloy at heating rates of: (a)2 K/min, (b)5 K/min, (c)10 K/min and (d)20 K/min

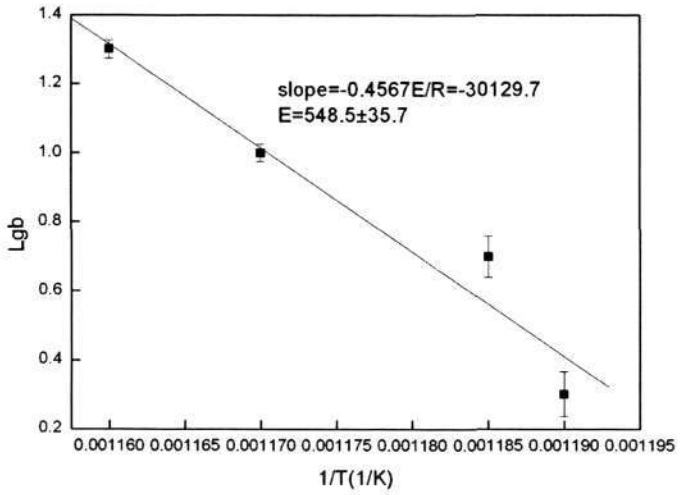

Figure 4. 38 Activation energy obtained from DSC measurement for the only peak of $Fe_{74.5}Si_{13.5}B_9Nb_3$ alloy

4.5.2 Structural Analysis

The phase formation of the initially amorphous $Fe_{74.5}Si_{13.5}B_9Nb_3$ alloy after heat treatment at 550 °C for different holding time: 5 min, 30 min, 1 h, 4 h, 8 h, 16 h and 24 h was studied by XRD technique (Figure 4. 39). With Nb alloying addition complex $Fe_{23}B_6$ and Fe_3B phases were formed in addition to the Fe-Si phase. It was also observed that as the annealing time was increased the relative intensity of the highest peak of the Fe-Si phase to that of the $Fe_{23}B_6$ phase increased. However, the relative intensity of the highest peak of the Fe_3B phase to that of the $Fe_{23}B_6$ phase decreased as the annealing time was increased.

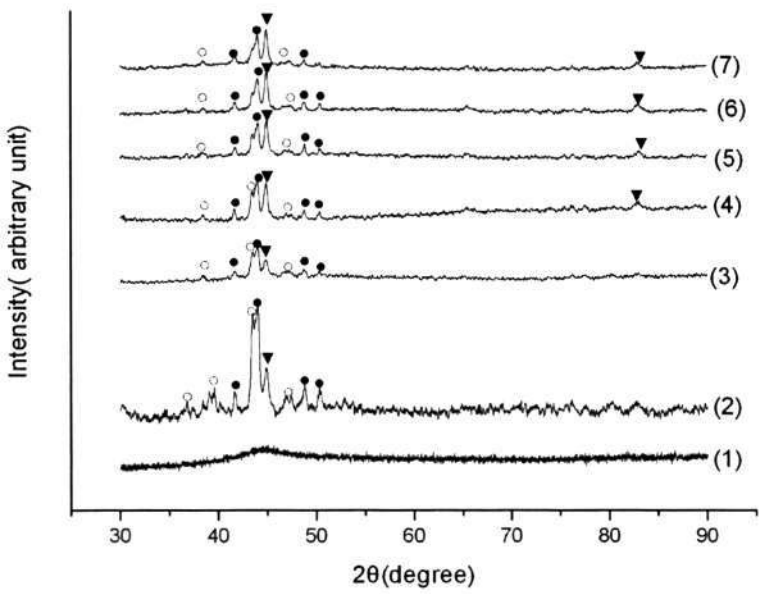

Figure 4. 39 XRD results for the $Fe_{74.5}Si_{13.5}B_9Nb_3$ alloy heat treatment at 550 °C for different holding time: (1)5 min, (2)30 min, (3)1 h, (4)4 h, (5)8 h, (6)16 h and (7)24 h: Fe-Si (▼), $Fe_{23}B_6$(●), and Fe_3B(○)

The following section combines the results of the structural analysis and microstructural observations by TEM analysis to describe the crystallization behavior of the initially amorphous $Fe_{74.5}Si_{13.5}B_9Nb_3$ alloy.

4.5.3 Crystallization Behavior

In this section the crystallization behavior of the $Fe_{74.5}Si_{13.5}B_9Nb_3$ alloy are described by combining TEM observations and the structural analysis by the XRD technique outlined in the previous section. Bright field TEM micrographs (Figure 4. 40) show that the equiaxed morphology of the products was retained the same as the annealing time was increased from 0.5 h to 24 h. Figure 4. 41 to Figure 4. 43 shows the morphology and the SADP of the phases formed after crystallization. With Nb alloying additions, instead of the dendritic morphology observed in the Fe-Si-B alloy, an equiaxed morphology was observed(Figure 4. 40). A high resolution TEM micrograph and corresponding SADP of the $Fe_{23}B_6$ phase are shown in Figure 4. 41. The lattice parameter of the $Fe_{23}B_6$ was measured as 1.073 nm, SADP analysis indicated an ordered f.c.c phase. For the Fe_3B phase a twinned lamellar morphology was observed in BF and DF micrographs, the corresponding SADP is provided in Figure 4. 42. BF, DF micrographs of the morphology of the Fe-Si phase and corresponding SADP were shown in Figure 4. 43.

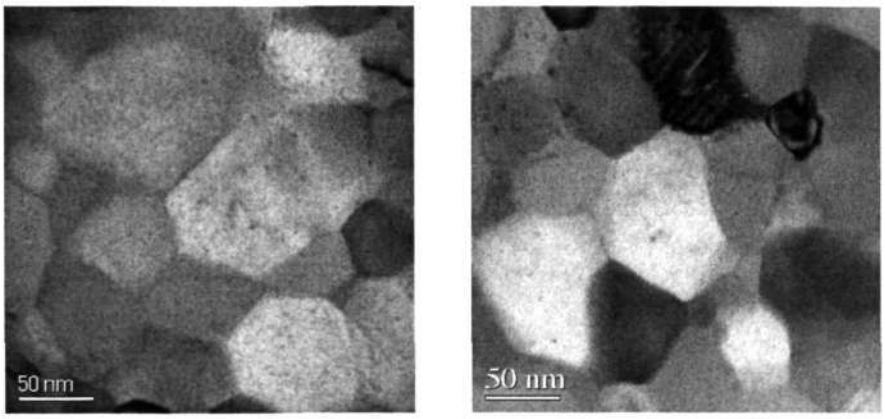

(a) (b)

Figure 4. 40 BF TEM micrographs of the $Fe_{74.5}Si_{13.5}B_9Nb_3$ alloy annealed at 550 °C for different time: (a) 0.5 h (b) 24 h

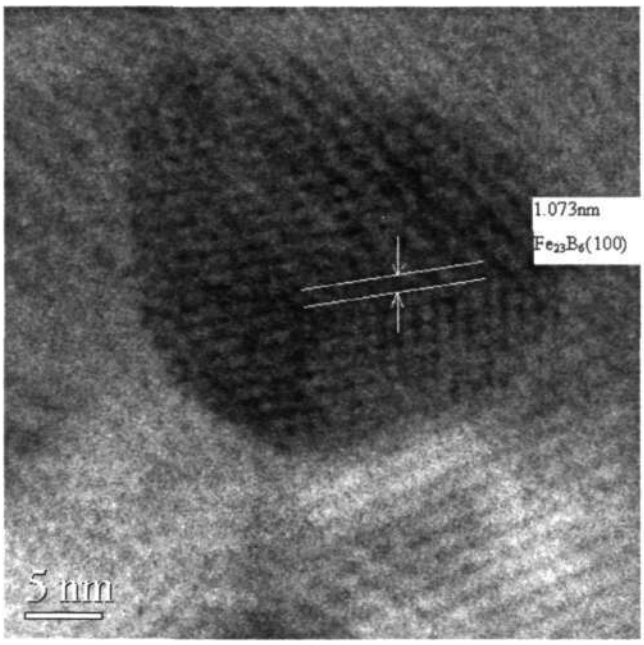

(a)

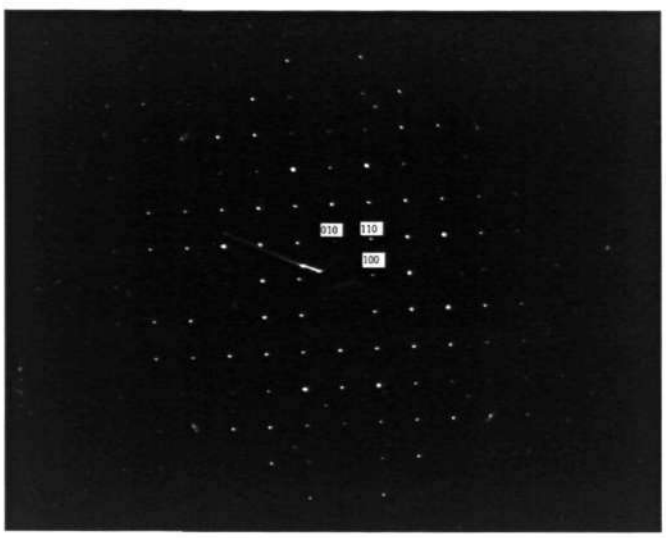

(b)

Figure 4. 41 HRTEM micrograph of the crystal of the $Fe_{23}B_6$ phase of the $Fe_{74.5}Si_{13.5}B_9Nb_3$ alloy annealed at 550 °C for 30 min: (a) bright field image (b) SADP, zone axis: $[01\bar{1}]$

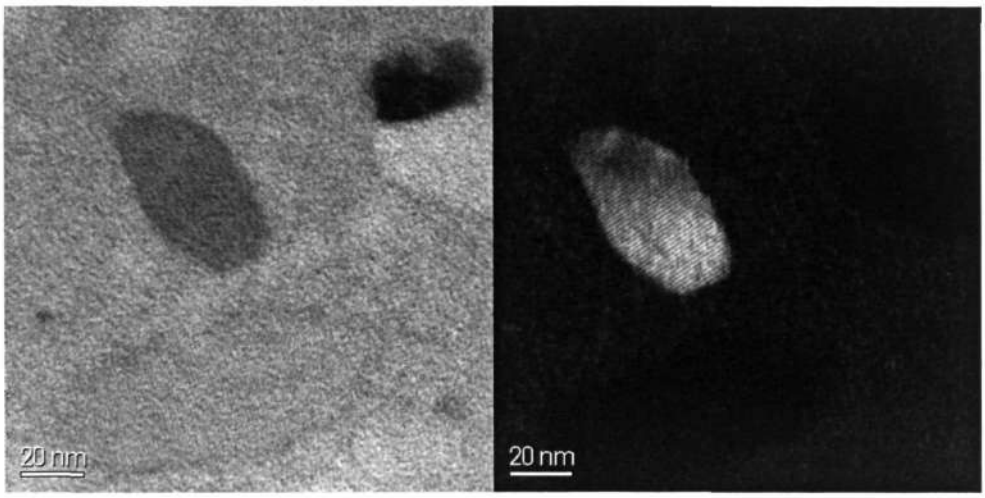

(a) (b)

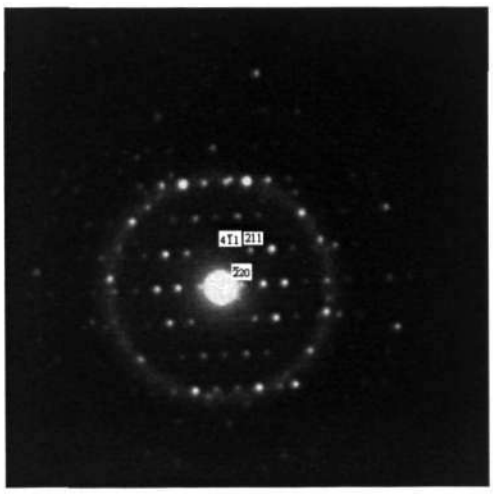

(c)

Figure 4. 42 TEM micrograph of the Fe_3B phase of the $Fe_{74.5}Si_{13.5}B_9Nb_3$ alloy annealed at 550 °C for 30 min: (a) bright field image (b) dark field image (c) SADP, zone axis:$[12\bar{2}]$

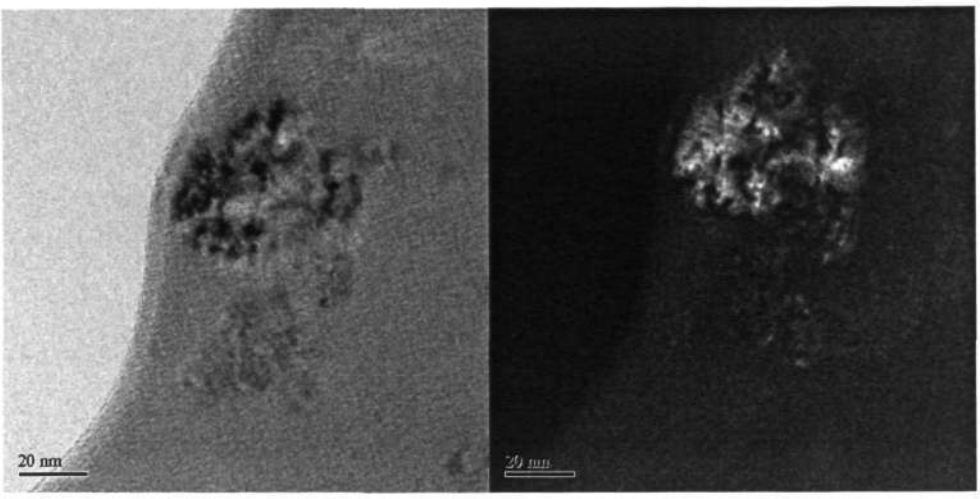

(a) (b)

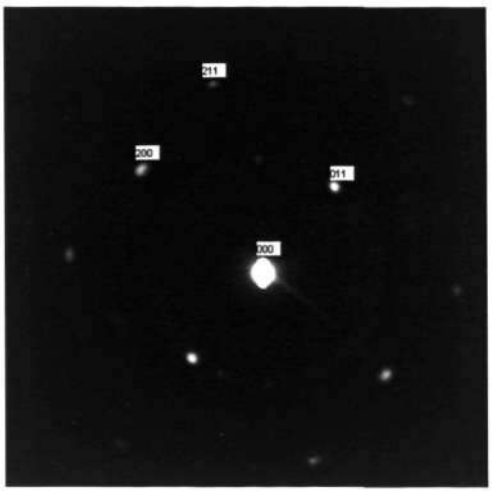

(c)

Figure 4. 43 TEM micrograph of the Fe-Si phase of the $Fe_{74.5}Si_{13.5}B_9Nb_3$ alloy annealed at 550 °C for 30 min: (a) bright field image (b) dark field image (c) SADP, zone axis:[$01\bar{1}$]

The next section deals with the thermal properties, structural analysis, crystallization behavior, EDS measurement and EELS elemental mapping of the alloy containing both Cu and Nb alloying additions. It was found that the effects of 1 at% Cu and 3 at% Nb

combined alloying additions are significantly different from that of the individual alloying additions of Cu and Nb. EDS and EELS elemental maps were used to elucidate the role of Cu and Nb alloying additions.

4.6 $Fe_{73.5}Si_{13.5}B_9Nb_3Cu_1$ alloy

In this section the thermal analysis, structural analysis, crystallization behavior, EDS measurements and EELS elemental mapping of the $Fe_{73.5}Si_{13.5}B_9Nb_3Cu_1$ alloy will be described[88]. It was found that the interaction between Cu and Nb alloying addition plays a crucial role in the crystallization process of this alloy.

4.6.1 Thermal Analysis

By means of DSC the crystallization temperatures of the $Fe_{73.5}Si_{13.5}B_9Nb_3Cu_1$ alloy were measured at heating rates of 2, 5, 10, and 20 K/min (Figure 4. 44). The calculated activation energy of crystallization was shown in Figure 4. 45. From the DSC curve it was observed that there are three exothermic peaks; the higher the heating rate, the higher is the peak temperature. At a heating rate of 10 K/min, the first crystallization peak occurs at 524 °C, the second at 681 °C and the third at 715 °C. The calculated activation energy of corresponding peaks was: 360±40.1 kJ/mol, 456±35.7 kJ/mol and 381±23.8 kJ/mol respectively, which are consistent with earlier reports [89,90].

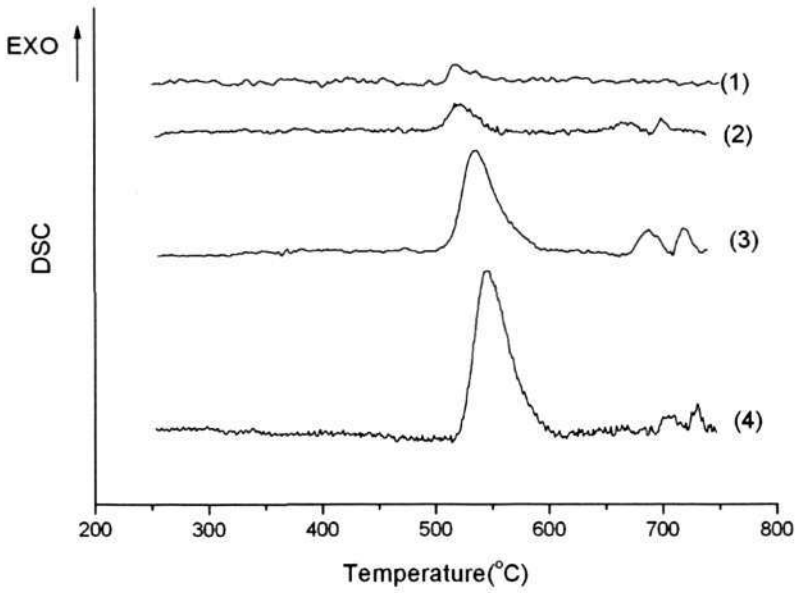

Figure 4. 44 DSC results for the $Fe_{73.5}Si_{13.5}B_9Nb_3Cu_1$ alloy at heating rates of: (1) 2 K/min, (2) 5 K/min, (3) 10K/min and (4)20 K/min

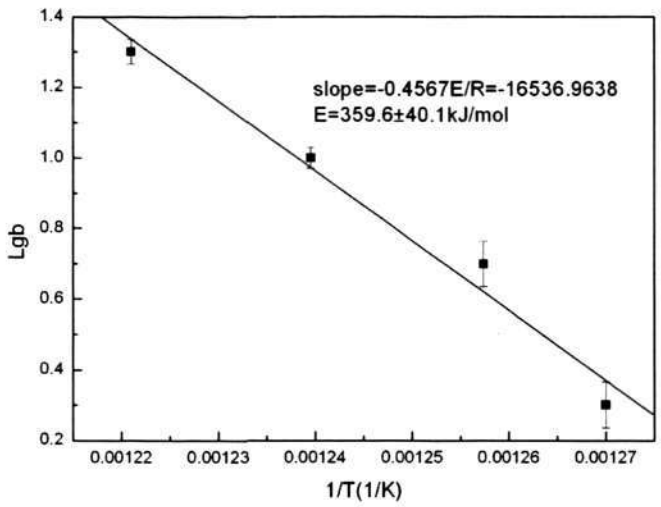

(a)

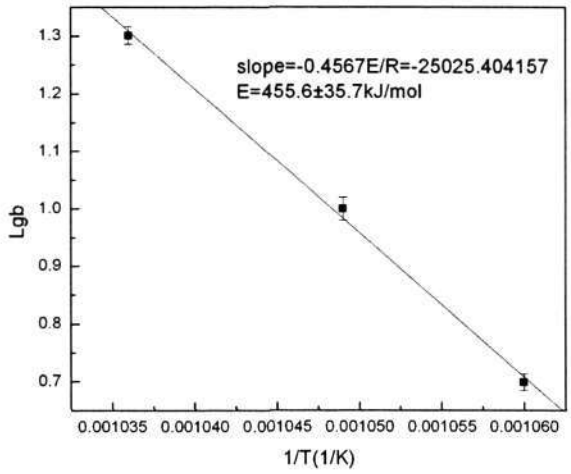

(b)

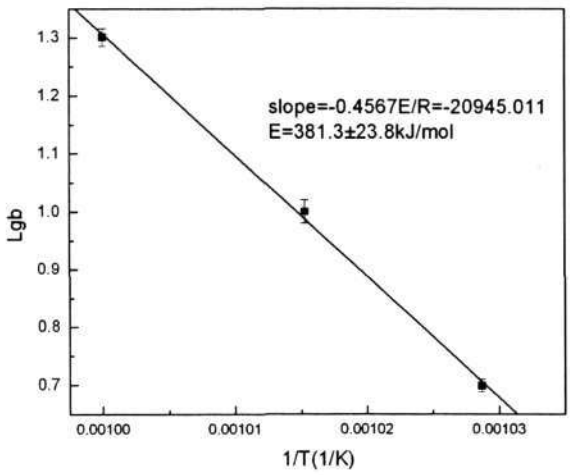

(c)

Figure 4. 45 Activation energy obtained from DSC measurements for the (a) first peak, (b) second crystallization peak and (c) third peak for a $Fe_{73.5}Si_{13.5}B_9Nb_3Cu_1$ alloy

4.6.2 Structural Analysis

The annealing temperature and time dependence of the phase formation were identified by XRD techniques, the results are shown in Figure 4. 46 and Figure 4. 47 respectively. It

can be seen that the alloy remains in the amorphous state after the sample was heat treated at 490 °C for 1 h and at 550 °C for 5 min. Primary crystallization was observed in samples annealed at 500 °C for 1 h. As the annealing temperature was increased from 500 °C to 640 °C the Fe-Si phase was the dominant phase. The Fe_3B phase did not appear until an annealing temperature of 600 °C was reached. After annealing at 640 °C for 1 h, the Fe_2B phase appeared due to the decomposition of the Fe_3B phase, this corresponds to the third peak in the DSC curves. Regarding the effect of annealing time on phase formation, it was found that as the annealing time was increased at 550 °C, the Fe-Si phase dominated while the secondary crystallization products (Fe_3B phase) did not form until 8 h of annealing. When the annealing time and temperature were increased, the relative intensity of the peak of the Fe-Si phase was found to increase indicating a higher volume fraction of the Fe-Si phase.

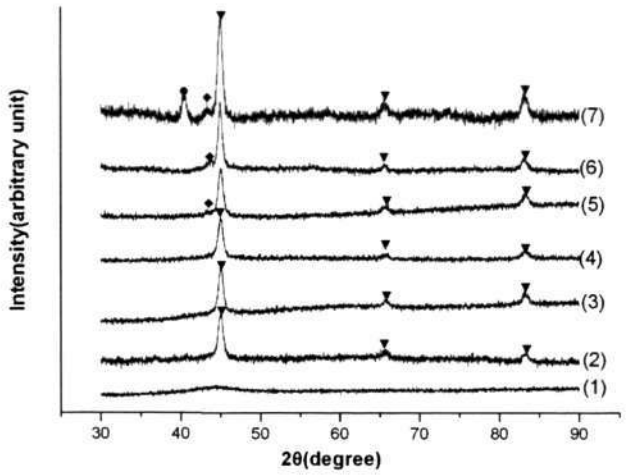

Figure 4. 46 XRD results for the $Fe_{73.5}Si_{13.5}B_9Nb_3Cu_1$ alloy heat treated at different temperature for 1 h: (1)490 °C, (2)500 °C, (3)515 °C, (4)530 °C, (5)550 °C, (6)600 °C, and (7)640 °C: Fe-Si (▼), Fe_3B(♦), Fe_2B(●)

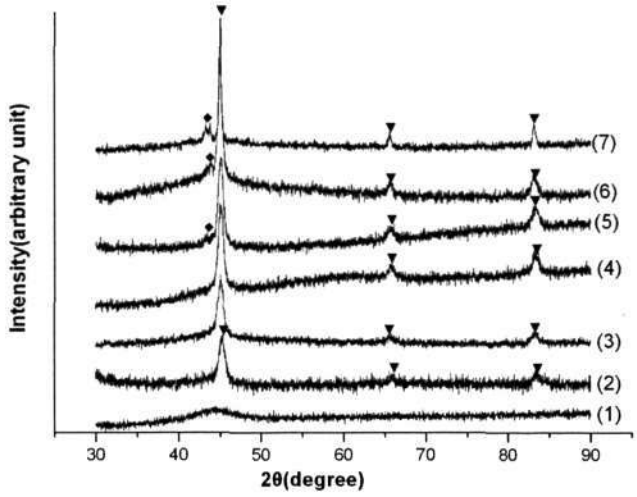

Figure 4. 47 XRD results for the $Fe_{73.5}Si_{13.5}B_9Nb_3Cu_1$ alloy heat treatment at 550 °C for different holding time: (1)5 min, (2)30 min, (3)1 h, (4)4 h, (5)8 h, (6)16 h and (7)24 h: Fe-Si (▼), Fe_3B(♦)

The following section presents TEM observations of the crystallization behavior of the $Fe_{73.5}Si_{13.5}B_9Nb_3Cu_1$ alloy.

4.6.3 Crystallization Behavior

The crystallization behavior of the $Fe_{73.5}Si_{13.5}B_9Nb_3Cu_1$ alloy was studied by TEM. Selected TEM micrographs and the corresponding SADP obtained from samples following heat treatment at 500 °C and 640 °C for 1 h are presented in Figure 4. 48. The primary crystallization products and corresponding SADP are shown in Figure 4. 48(a) and (b). As has been mentioned previously, crystals about 10 nm in size were found within the amorphous matrix [1,2,91]. From the corresponding SADP the phase was indexed as a b.c.c. Fe-Si phase which is consistent with the XRD results (Figure 4. 47). When the annealing temperature was increased to 600 °C secondary crystallization

occurred, resulting in the formation of the Fe_3B phase with a striped morphology, as can be seen in the bright field and dark field images in Figure 4. 48 (c) and (d). The dark field image was obtained from the streaks as circled in the corresponding SADP (Figure 4. 48(e)).

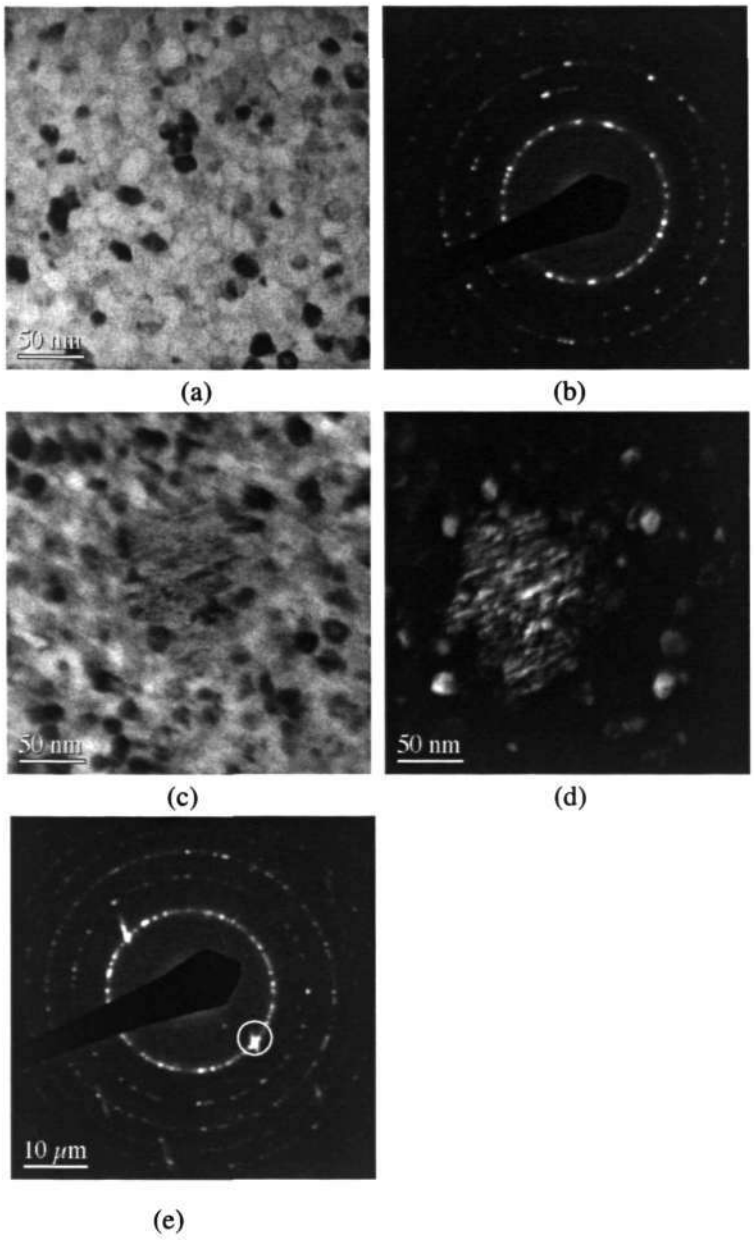

Figure 4. 48 TEM micrographs of the crystal from the $Fe_{73.5}Si_{13.5}B_9Nb_3Cu_1$ alloy annealed at 500 °C for 1 h: (a) bright field image (b) SADP after an annealing at 600 °C for 1 h: (c) bright field image (d) dark field image (e) SADP

In order to elucidate the role of Cu and Nb, EDS measurements of the concentration of Fe, Si, Nb and Cu in regions with low as well as high crystal densities were performed.

4.6.4 EDS measurements

In this section the EDS measurements of the Fe, Si, Nb and Cu are repeated. The diameter of the electron spot size is about 2 nm. The measured EDS spectra were corrected for instrumental errors, digitally filtered to suppress the background and Cliff-Lorimer corrections were performed [78].

HRTEM was used to check that no overlap between the nanocrystals occurred in the observed areas. In samples heat treated at 500 °C for 10 min and 550 °C for 60 min respectively HRTEM and the corresponding results of concentration profiles in the regions with a low crystal density are shown in Figure 4. 49 and Figure 4. 51. The compositions values are presented in Table 4. 2 and Table 4. 4. Interestingly, it was observed that the concentration profile of Cu and Nb elements showed opposite trends. At the center of the single crystal Nb content is higher and Cu content is lower, which can also be observed from the relative intensity of Cu and Nb peaks in Figure 4. 51(c). However, at the interface of the crystal the composition of Cu is higher while that of Nb is higher (Figure 4. 51(d)).

Figure 4. 50 and Figure 4. 52 show the concentration profile in regions with high crystal density after the samples were annealed at 500 °C for 10 min and 550 °C for 60 min, respectively. The corresponding values are tabulated in Table 4.3 and Table 4. 5. It was

again observed that the concentration profile of Cu and Nb showed opposite trends, but the changing trends of Cu and Nb elements differed from that observed in the case of low crystal density. In the center of the nanocrystal the concentration of Cu element is higher than that at the interface, this can be also observed in Figure 4. 52(c). At the same time the Nb content in the region between the nanocrystals is much higher than that in the nanocrystal, as indicated by Figure 4. 52(d)

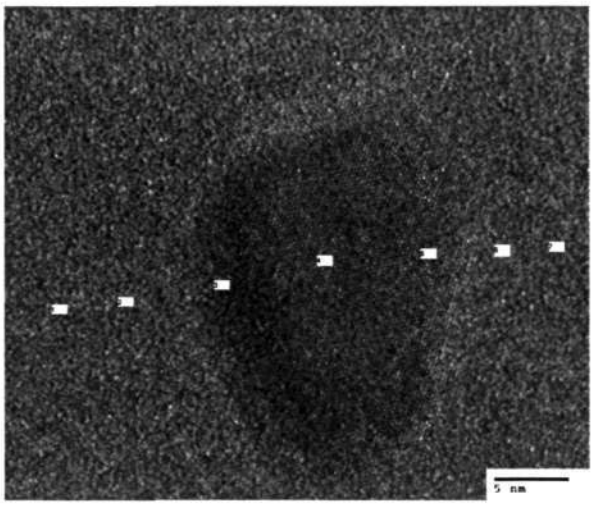

(a)

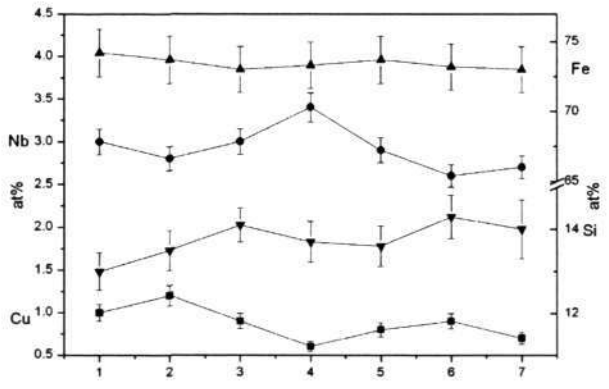

(b)

Figure 4. 49 TEM micrograph (a) and concentration profile of the elements (b) corresponding to the indicated spots in Figure 4. 49(a) after the $Fe_{73.5}Si_{13.5}B_9Nb_3Cu_1$alloy was annealed at 500 °C for 10 min

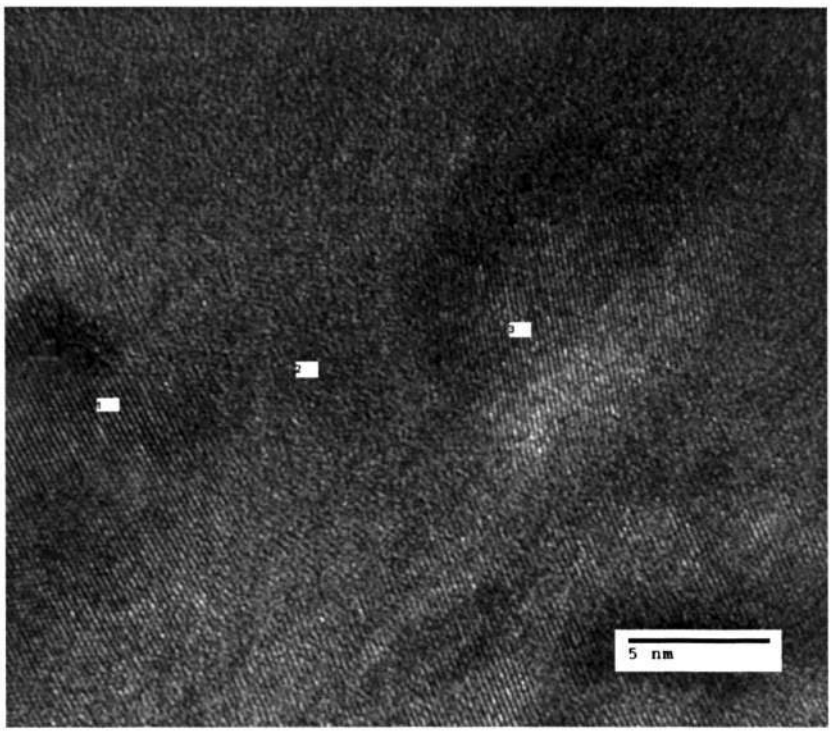

(a)

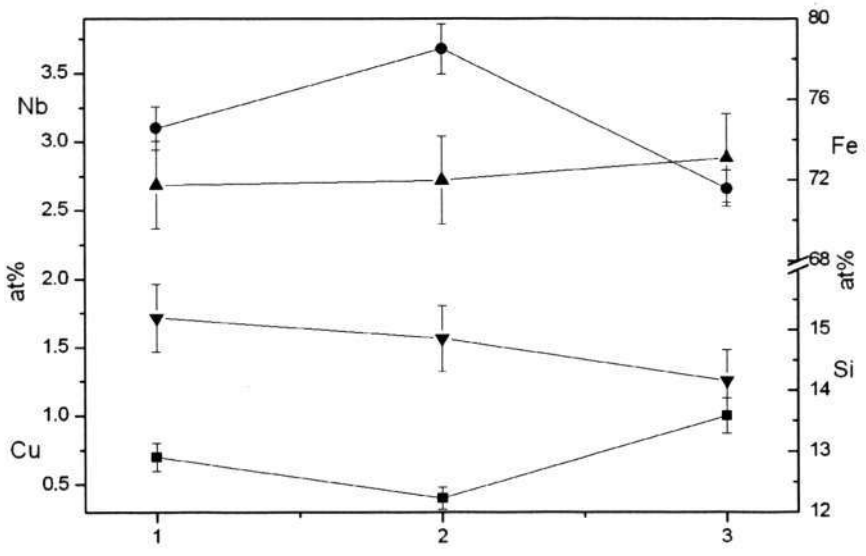

(b)

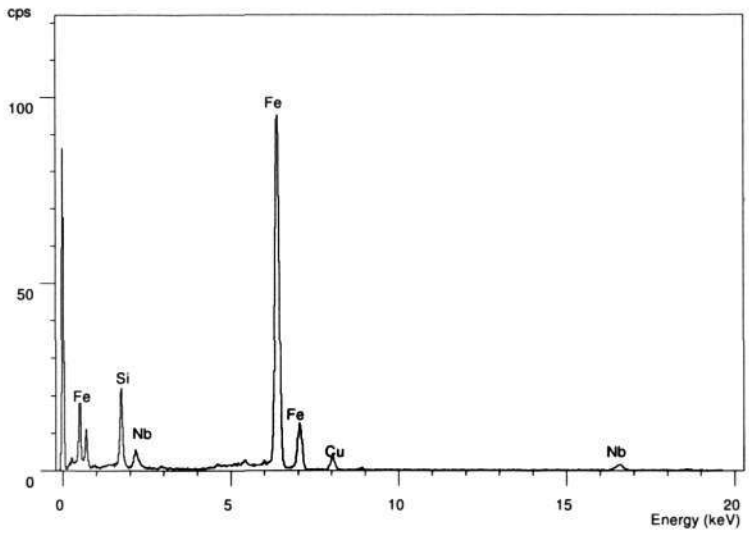

(c)

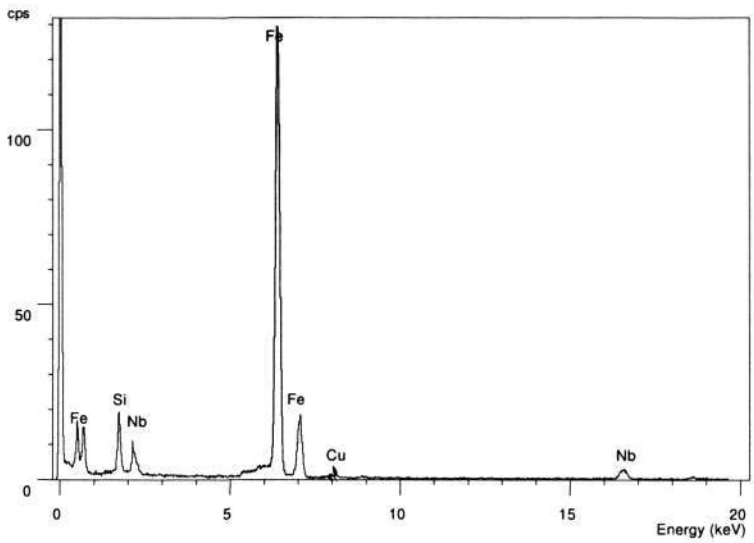

(d)

Figure 4. 50 TEM micrograph (a) and concentration profile of the elements (b) corresponding to the indicated spots in Figure 4. 50(a), EDS spectrum of spot 3 (c) and EDS spectrum of spot 2 (d) after the $Fe_{73.5}Si_{13.5}B_9Nb_3Cu_1$alloy was annealed at 500 °C for 10 min

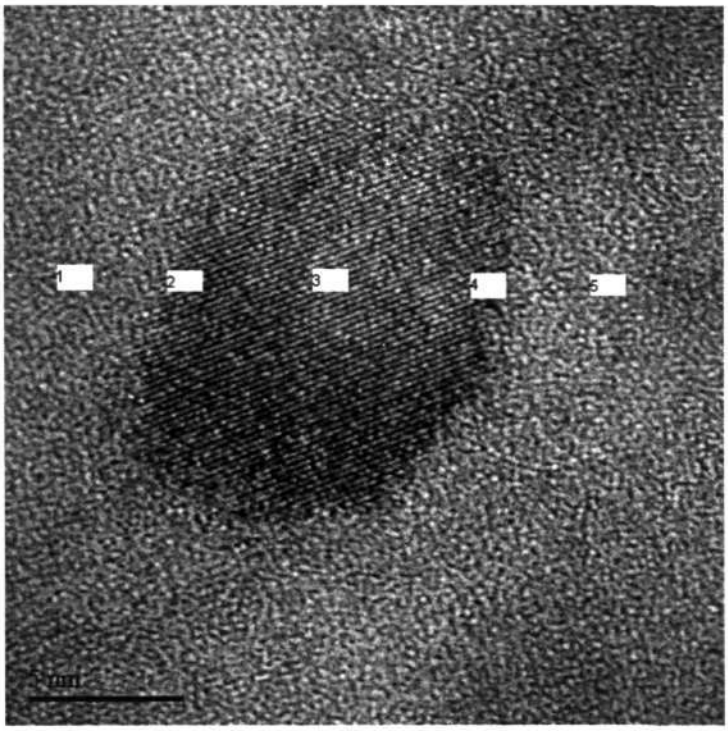

(a)

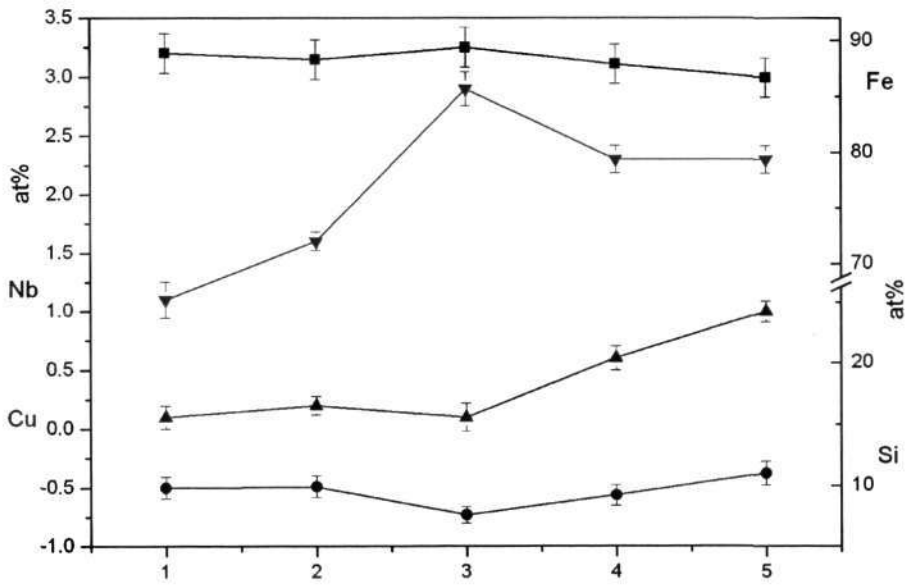

(b)

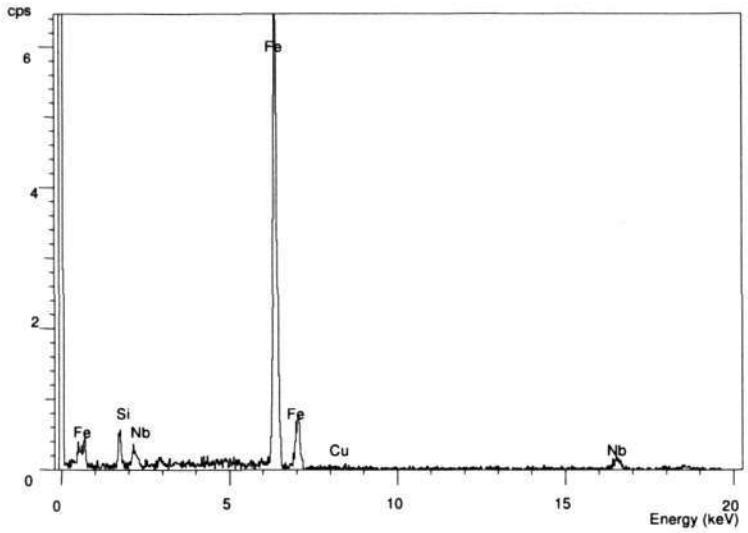

(c)

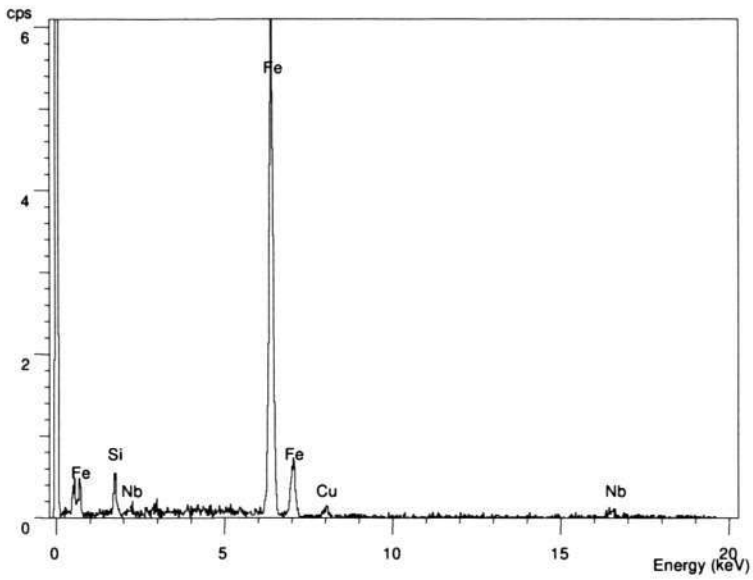

(d)

Figure 4. 51 TEM micrograph (a) and concentration profile of the elements (b) corresponding to the indicated spots in Figure 4. 51(a), EDS spectrum of spot 3 (c) and EDS spectrum of spot 4 (d) after the $Fe_{73.5}Si_{13.5}B_9Nb_3Cu_1$alloy was annealed at 550 °C for 60 min

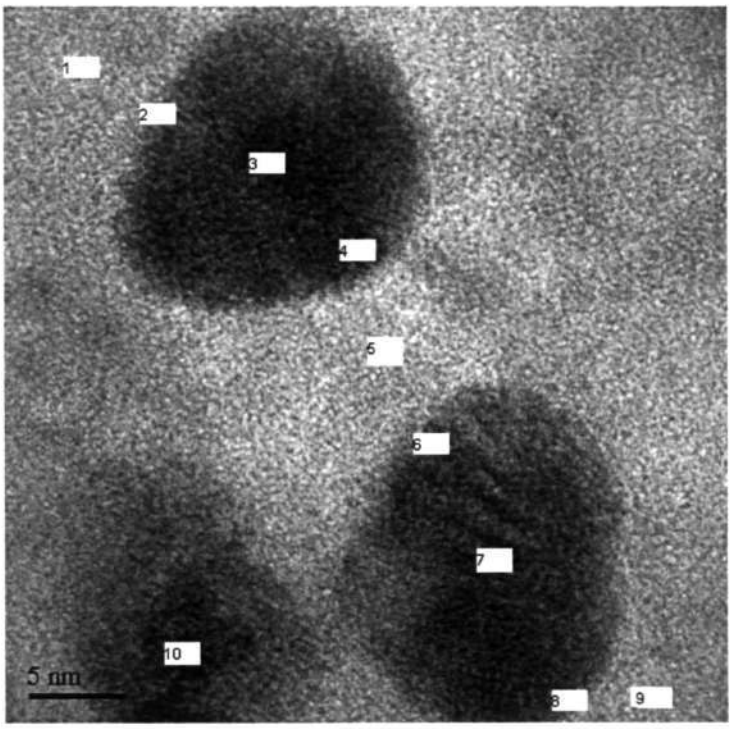

(a)

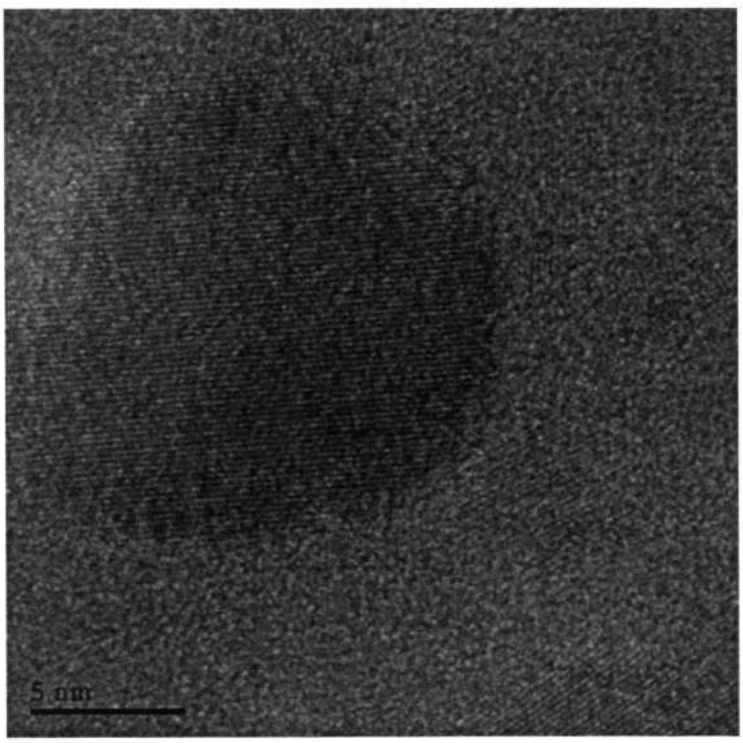

(b)

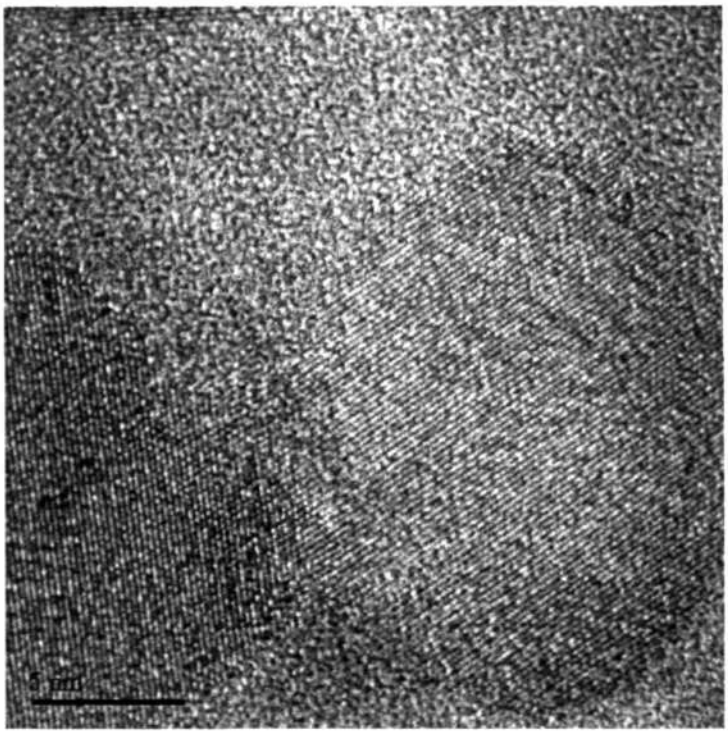

(c)

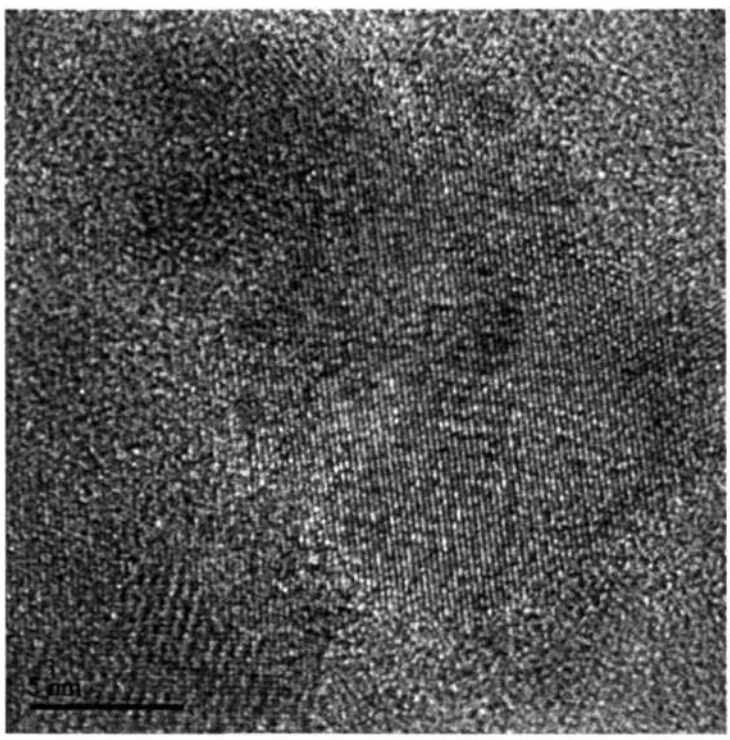

(d)

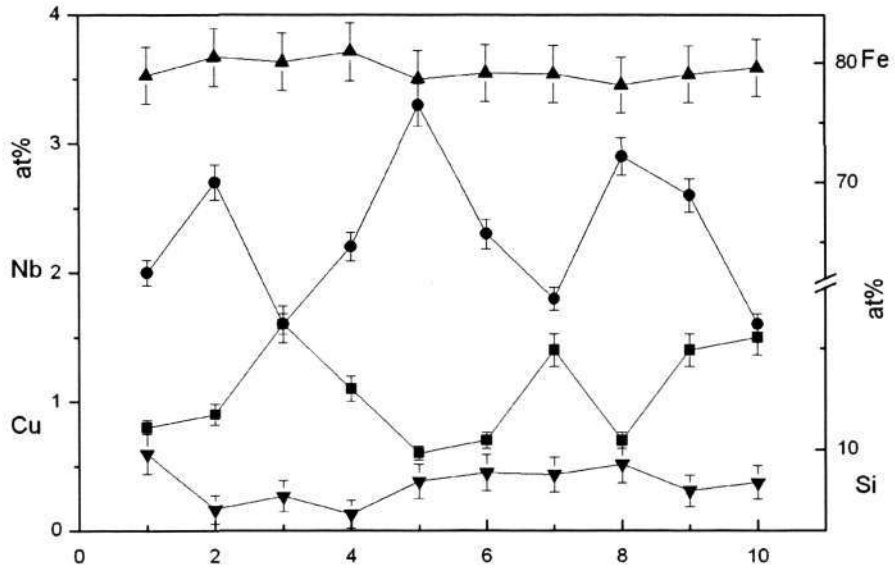

(e)

Figure 4. 52 TEM micrograph and EDS measurements of the region between nanocrystals from a $Fe_{73.5}Si_{13.5}B_9Nb_3Cu_1$ alloy annealed at 550 °C for 60 min: (a) bright field image (b) HRTEM image corresponding to the nanocrystal 3; (c) HRTEM image corresponding to nanocrystal 7; (d) HRTEM image corresponding to the nanocrystal 10; (e) concentration profile of the elements corresponding to the marked spots in Figure 4. 52(a)

Table 4. 2 EDS measurements corresponding to Figure 4. 49

Element(at%)	1	2	3	4	5	6	7
Fe	74	73.5	73	73.3	73.7	73.2	73.6
Si	3	13.5	14.1	13.7	13.6	14.3	14
Cu	1	1.2	0.9	0.6	0.8	0.9	0.7
Nb	3	2.8	3	3.4	2.9	2.6	2.7

Table 4. 3 EDS measurements corresponding to Figure 4. 50

Element(at%)	1	2	3
Fe	72.9	72.2	73.5
Si	15	14.7	14
Cu	1.3	0.6	1.5
Nb	1.8	3.5	2.

Table 4. 4 EDS measurements corresponding to Figure 4. 51

Element(at%)	1	2	3	4	5
Fe	80.9	74.3	81.4	80.0	78.9
Si	8.9	9.0	6.9	8.4	10.1
Cu	0.1	0.2	0.1	0.5	0.9
Nb	1.1	1.5	2.6	2.1	2.1

Table 4. 5 EDS measurements corresponding to Figure 4. 52

Element(at%)	1	2	3	4	5	6	7	8	9	10
Fe	80.2	81.5	81.0	81.8	79.8	80.3	80.1	79.4	80.1	80.5
Si	8.0	6.4	7.0	6.2	7.7	8.0	8.0	8.4	7.2	7.6
Cu	1.0	0.8	1.5	1.0	0.5	0.6	1.3	0.6	1.3	1.4
Nb	1.8	2.5	1.5	2.0	3.0	2.1	1.6	2.6	2.4	1.5

4.6.5 EELS Elemental Mapping

In order to corroborate the EDS measurement results, EELS elemental mapping was conducted for B, Nb and Cu, white regions indicate a higher concentration of an element. After annealing at 500 °C for 10 min, the initial stage of the crystallization is observed, some regions rich in Cu are observed(Figure 4. 53(b)), while other regions rich in Nb (Figure 4. 53(c)) are also seen. Such Cu and Nb rich regions can serve as nucleation sites for the formation of new Fe-Si nanocrystals.

Observation of samples after heat treatment at 550 °C for 60 min show that the Nb composition is higher near the matrix: crystal interface, consistent with the EDS results(Figure 4. 54). B composition is higher near the interface compared to within the crystal indicating that B was rejected during crystallization, consistent with previous reports [11].

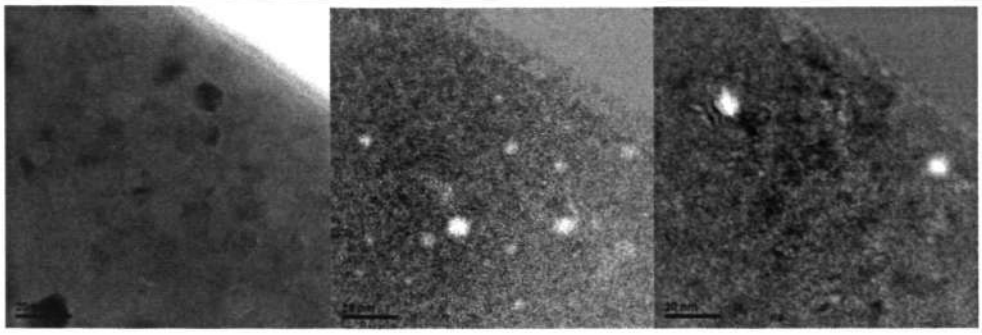

(a) (b) (c)

Figure 4. 53 (a) BF TEM micrograph of the Fe-Si-B-Nb-Cu alloy after heat treatment at 500°C for 10min (b) EELS map of Cu (c) EELS map of Nb

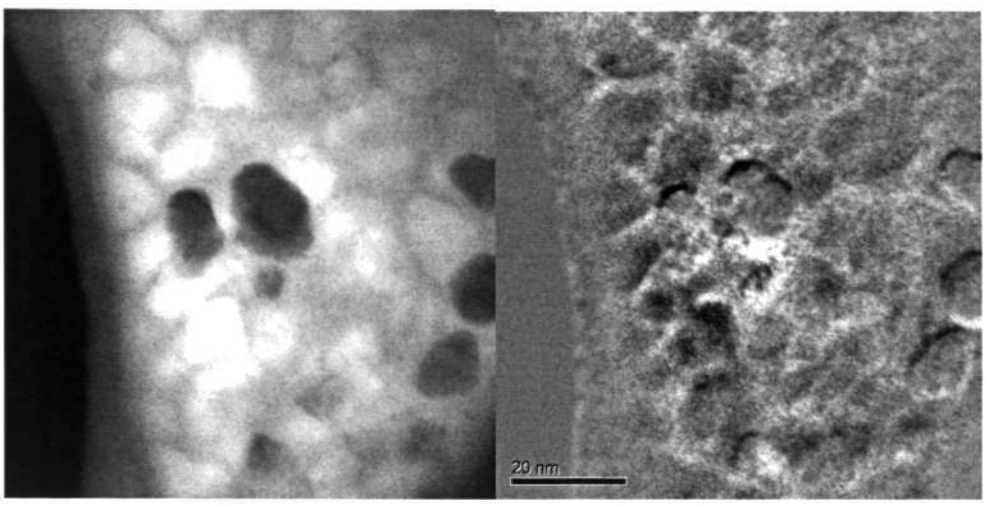

(a) (b)

Figure 4. 54 (a) BF TEM micrograph of the Fe-Si-B-Nb-Cu alloy after heat treatment at 550 °C for 1 h (b) EELS map of Nb

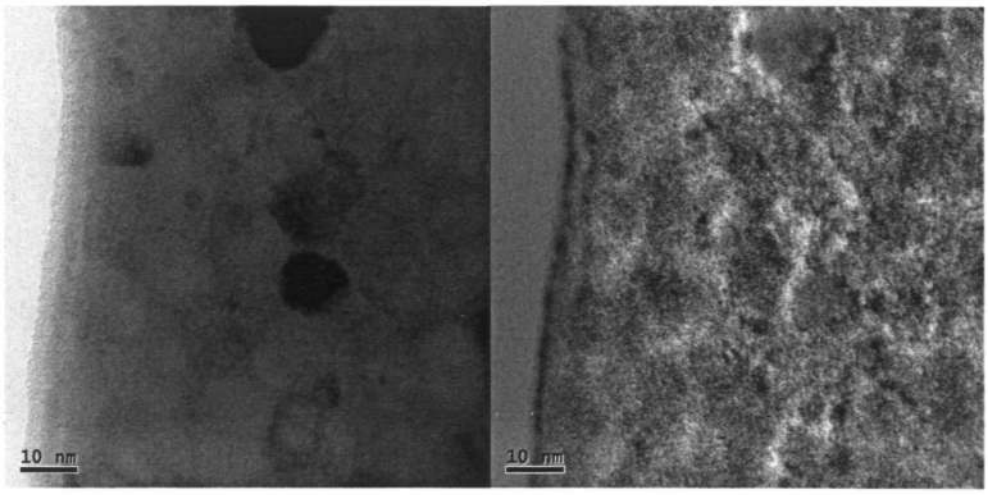

(a) (b)

Figure 4. 55 (a) BF TEM micrograph of the Fe-Si-B-Nb-Cu alloy after heat treatment at 550 °C for 1 h (b) EELS map of B

4.6.6 Quantitative measurements

TEM was used, for the first time in this alloy composition, to achieve a quantitative evaluation of the crystal size distribution, crystal number density and volume fraction. Based on these quantitative values the crystallization process can be understood. The crystal density and mean crystal size were studied by dark field TEM. Some crystals appear more than once in the dark field image due to the symmetry of b.c.c. crystals, these crystals were eliminated before quantitative analysis. The micrographs observed in TEM are the projection of crystals from the top to the bottom of the specimen, which implies that the crystal density and size observed in the projected image should be corrected for the thickness of the sample [92].

The thickness of the specimen was typically measured to be about 100 nm by the EELS

technique, the crystal size is much smaller than the specimen thickness. The mean crystal size is given by [93]:

$$\overline{D} = \frac{dt}{t - d + \frac{\pi A_A}{L_A}} \qquad \text{Eq.4. 1}$$

where, A_A is the projected area, t is the foil thickness, L_A is the perimeter density (1/nm), d is the projected diameter of the crystal, $\overline{D}$ is the real mean diameter.

The number of crystals per unit area, N_A, was determined using the line intersection technique of quantitative metallography, the number of crystals per unit volume, Nv, can be calculated by the equation:

$$N_v = \frac{N_A}{t + \overline{D}} \qquad \text{Eq.4. 2}$$

The volume fraction of crystal, fv, can be calculated from the fraction of the projected area, f_A, by Eq. 4.3

$$f_v = \frac{f_A}{1 + \frac{3t}{2\overline{D}}} \qquad \text{Eq.4. 3}$$

A large projected area compared with the crystal size was selected to increase the precision of the data [94].

The sample thickness was measured by EELS technique. In different regions the degree of variation in the sample thickness is about several nanometers. Figure 4. 56 showed a typical EELS result for the sample heat treated at 550 °C for 1 h.

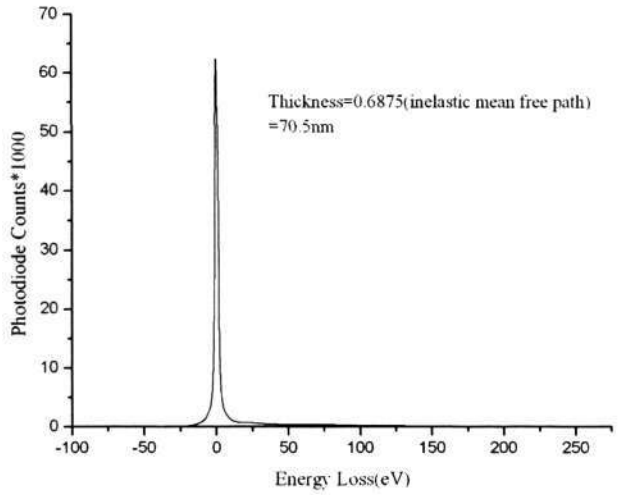

Figure 4. 56 EELS result for the sample heat treated at 550 °C for 1 h

Details of the quantitative metallography were measured from the dark field images and the calculated values are listed in Appendix I, Table A1 to Table A4. The crystal size, number of crystals/unit volume and the volume fraction generally increased with increasing heat treatment time.

A quantitative analysis of the crystal size distribution of the samples after heat treatment at different temperatures and time is presented in Figure 4. 57 to Figure 4. 60. During this measurement it was assumed that the thickness of the subtended area is constant and the crystal is spherical. As annealing temperature was increased the mean crystal size and the fraction of crystals more than 20 nm in size increased.

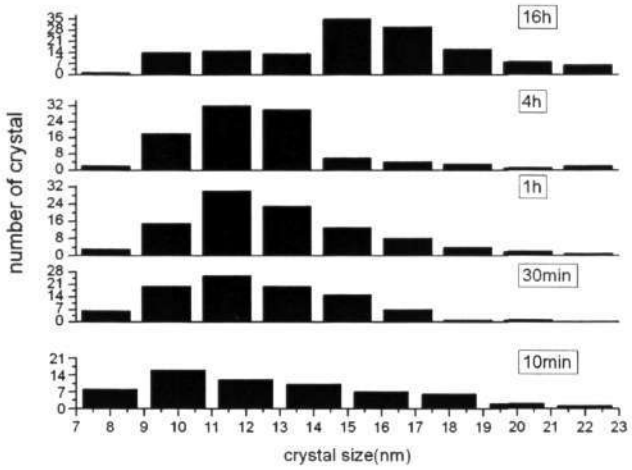

Figure 4. 57Quantitative analysis of crystal size distribution after heat treatment at 500 °C

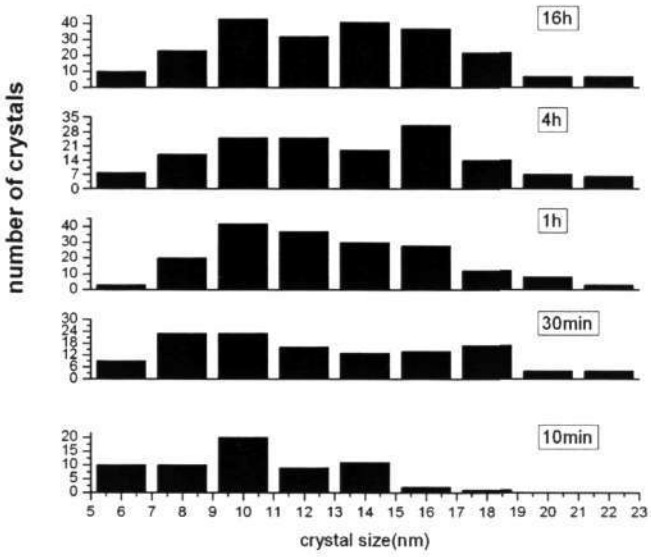

Figure 4. 58 Quantitative analysis of crystal size distribution after heat treatment at 515°C

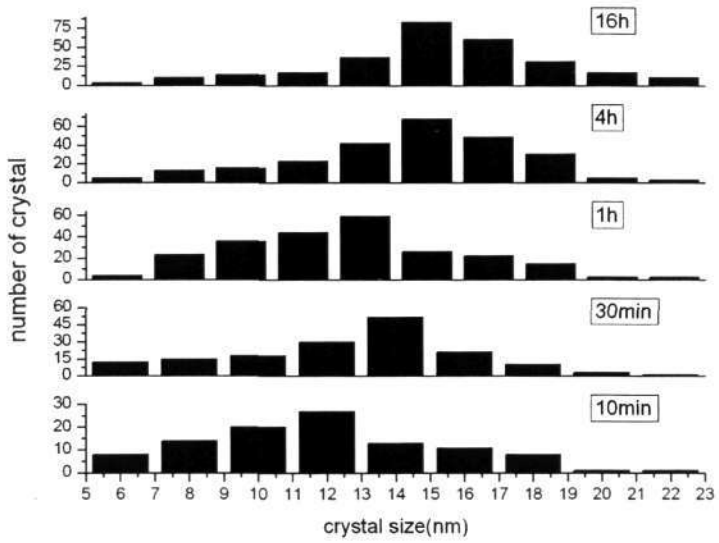

Figure 4. 59 Quantitative analysis of crystal size distribution after heat treatment at 530°C

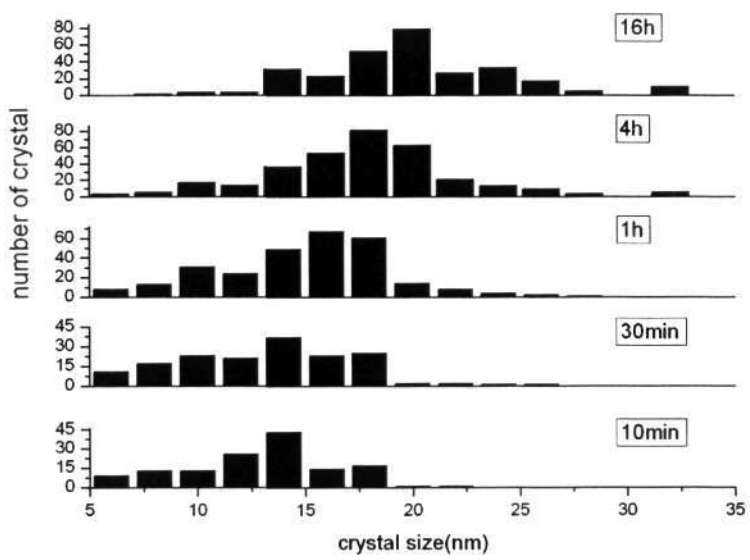

Figure 4. 60 Quantitative analysis of crystal size distribution after heat treatment at 550°C

Figure 4. 61 shows the crystal volume fraction at different temperature as a function of annealing time. The volume fraction increased as the annealing time and temperature

were increased. It is very interesting to note that the growth slowed down after aging times of 1 h. The variation of number of crystals per unit volume with heat treatment time at different temperatures are shown in Figure 4. 62. The average crystal density increased initially with an increase in heat treatment time, and reached a constant value. Figure 4. 63 indicates the average crystal size as a function of heat treatment time, initially the growth rate is high followed by a marked slowing down in the growth as the crystallization proceeded. That is because the crystallization process is diffusion controlled. After annealing for 1 h the volume fraction of crystals increased slowly due to the slow diffusion of Si and Fe as more and more crystals formed. At the same time the nucleation sites become less as more and more crystals formed. The overlapping of the diffusion fields after annealing for 1 h also slowed down the growth. Thus the growth of the crystal volume fraction decreased after aging of 1h

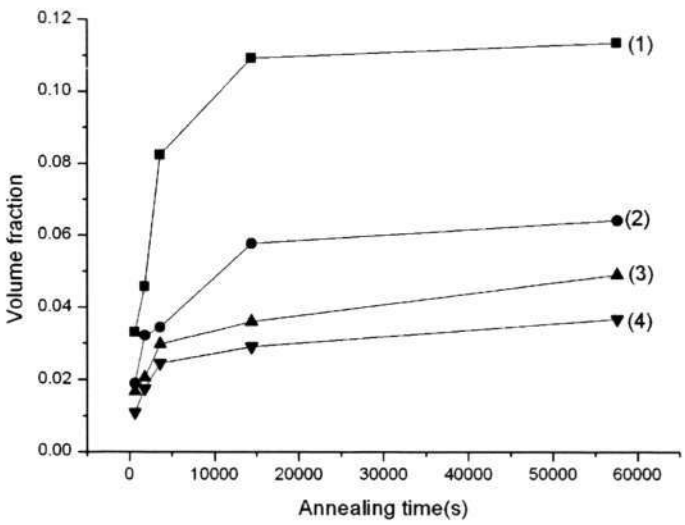

Figure 4. 61 Crystal volume fraction measured by TEM at (1) 550 °C, (2) 530 °C, (3) 515 °C and (4) 500 °C

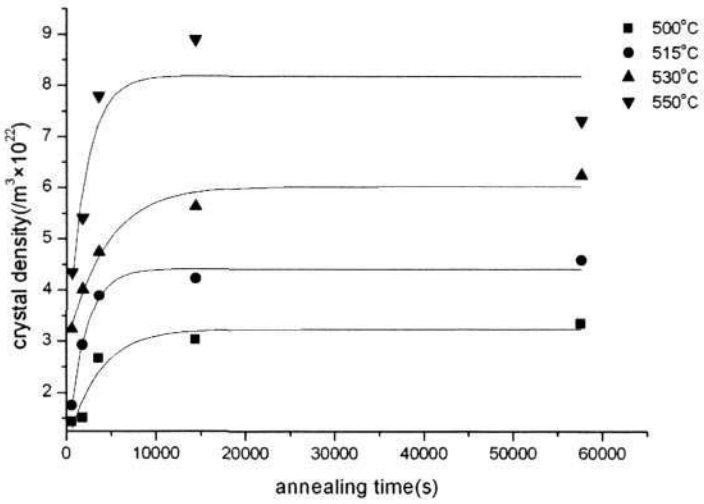

Figure 4. 62 The number of crystal per unit volume formed during crystallization. Note that the number of crystal rises sharply and then stabilizes at longer heat treatment time

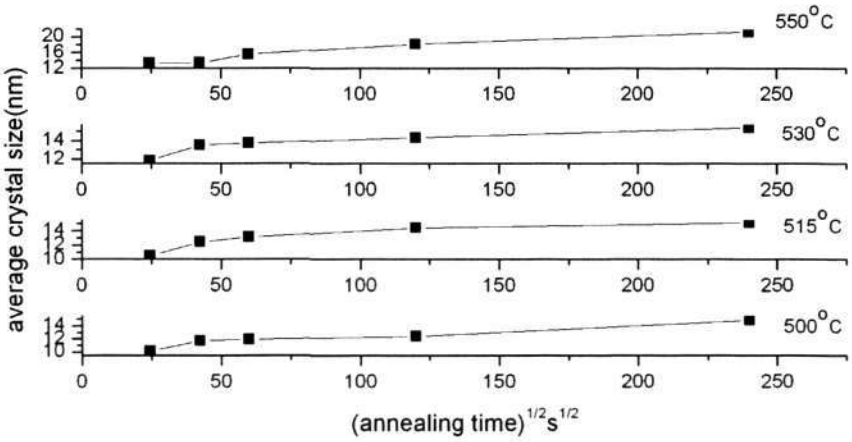

Figure 4. 63 The average crystal size as a function of heat treatment time

4.7 Comparison of the results for the four alloys

This section compares the results of thermal properties (Figure 4. 64), structural analysis (Figure 4. 65) and microstructural observation (Figure 4. 66) of the four alloy

compositions in order to study the individual and synergistic effects of 1 at% Cu and 3 at% Nb alloying additions in the $Fe_{77.5}Si_{13.5}B_9$alloy[95].

Figure 4. 64 shows the DSC curves of the selected alloys. For the Fe-Si-B alloy, two peaks were observed which indicated that two crystallization processes occurred during crystallization. With Cu alloying additions there are two peaks in the DSC curve, the first occurred at lower temperatures compared to the Fe-Si-B alloy, which showed that Cu alloying additions made primary crystallization earlier. With Nb alloying additions only one peak was observed at higher temperatures compared to the Fe-Si-B alloy, which indicated that the amorphous matrix was stabilized in the Fe-Si-B-Nb alloy. With both Cu and Nb alloying additions three peaks were observed which indicated that besides primary and secondary crystallization, processes such as decomposition of the Fe_3B phase to the Fe_2B phase and α-Fe also occurred at higher temperatures.

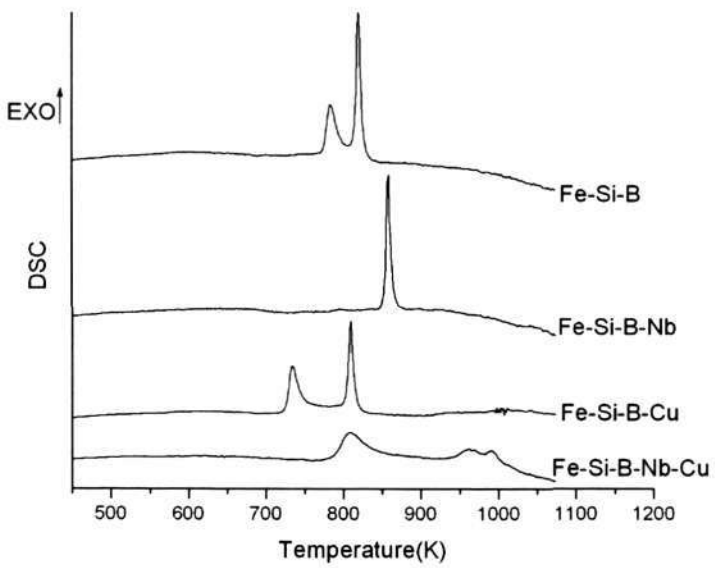

Figure 4. 64 DSC measurements of different alloys with heating rate at 10 K/min

By using the Doyle-Ozawa method the activation energy can be calculated. The table below shows that activation energy for primary crystallization of the Fe-Si-B-Cu alloy is the lowest: 260±5.86 kJ/mol while that of the Fe-Si-B-Nb alloy is the highest: 549±35.7 kJ/mol.

Table 4. 6 Calculated activation energy of the four alloys

	$Fe_{73.5}Cu_1Nb_3Si_{13.5}B_9$				$Fe_{76.5}Cu_1Si_{13.5}B_9$			
Heating Rate(K/min)	2	5	10	20	2	5	10	20
First Peak(K)	790	795	807	819	715	720	729	745
Activation energy(kJ/mol)	360±40.1				260±5.9			
Second peak(K)		937	954	971	793	793	804	822
Activation energy(kJ/mol)	456±35.7				257±30.4			
Third peak(K)		972	985	1003				
Activation energy(kJ/mol)	381±23.8							
	$Fe_{74.5}Nb_3Si_{13.5}B_9$				$Fe_{77.5}Si_{13.5}B_9$			
Heating Rate(K/min)	2	5	10	20	2	5	10	20
First Peak(K)	841	844	852	871	766	772	780	795
Activation energy (kJ/mol)	549±35.7				376±5.9			
Second Peak(K)					800	805	815	832
Activation energy(kJ/mol)					342±38.7			

The phases formed after annealing at 550 °C for 30 min were identified by XRD results

(Figure 4. 65). For the Fe-Si-B alloy, Fe-Si-B-Cu alloy and Fe-Si-B-Nb-Cu alloys only the Fe-Si peaks were identified. In the case of the Fe-Si-B-Nb alloy three phases were formed: Fe-Si, $Fe_{23}B_6$ and Fe_3B.

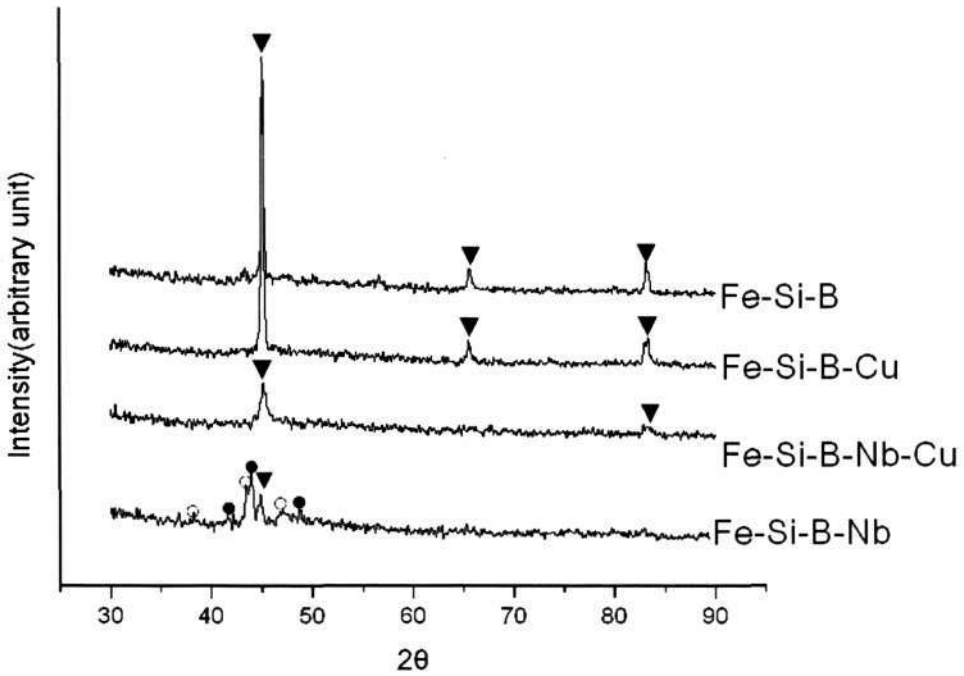

Figure 4. 65 XRD results for the alloy heat treatment at 550 °C for 30 min: Fe-Si (▼), $Fe_{23}B_6$(●), and Fe_3B(○)

TEM observations showed dramatically different microstructures, summarized in Figure 4. 66. Figure 4. 66 (a) to (d) showed the TEM microstructures of the alloys after heat treatment at 550 °C for 30 min. For the Fe-Si-B alloy the dendritic morphology was observed (Figure 4. 66 (a)). On the other hand, with Cu alloying addition, instead of the dendritic morphology, a spheroidal morphology with rough interface was observed (Figure 4. 66(b)), the crystal size varies from 50 nm to 100 nm. With Nb alloying

additions an equiaxed morphology with smaller crystal size was observed (Figure 4. 66 (c)), the crystal size is in the range from 30 nm to 50 nm. With both Cu and Nb alloying additions equiaxed nanocrystals about 15 nm in size was observed (Figure 4. 66 (d)).

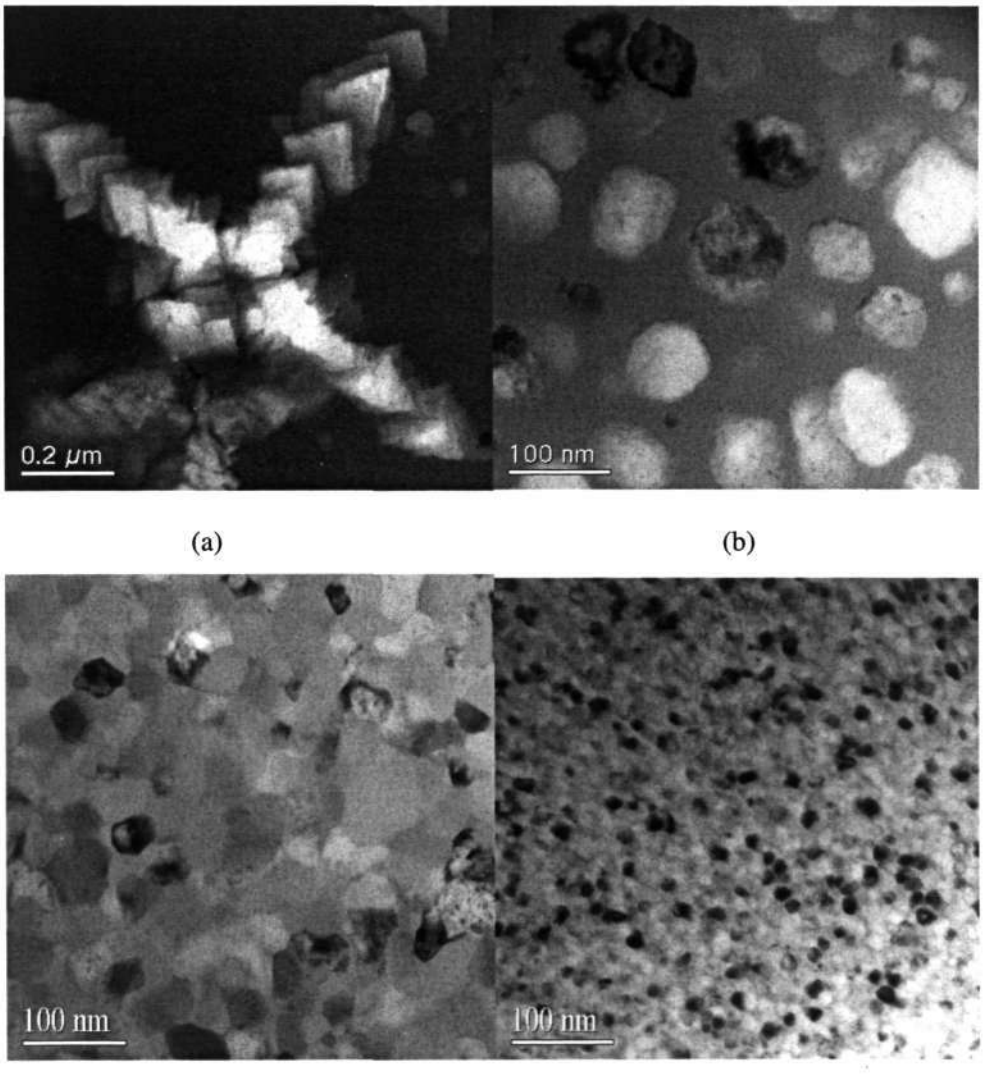

Figure 4. 66 BF TEM micrographs of the (a) $Fe_{77.5}Si_{13.5}B_9$, (b) $Fe_{76.5}Si_{13.5}B_9Cu_1$, (c) $Fe_{74.5}Si_{13.5}B_9Nb_3$ and (d) $Fe_{74.5}Si_{13.5}B_9Nb_3Cu_1$ alloys heat treatment at 550 °C for 30 min

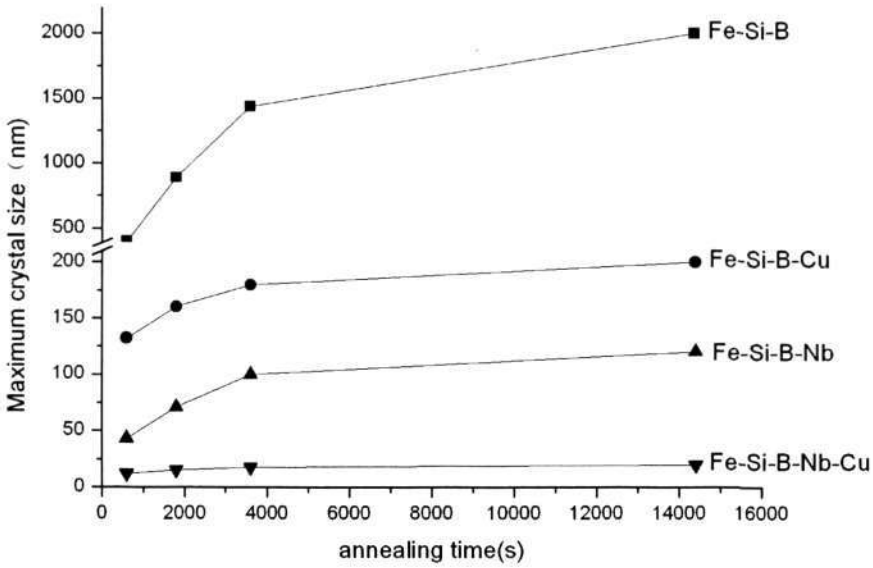

Figure 4. 67 Maximum crystal size as function of annealing time at 500 °C

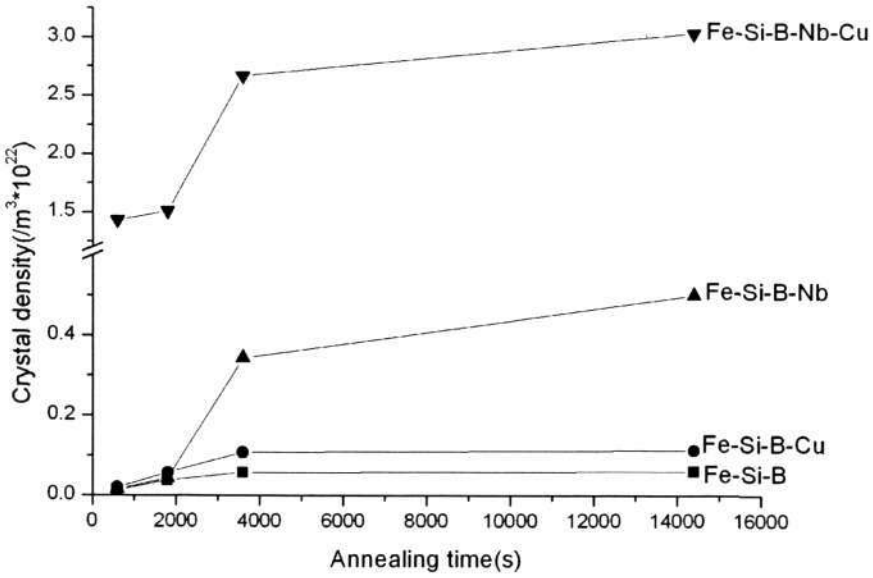

Figure 4. 68 The number of crystal per unit volume as function of annealing time at 500 °C

Figure 4. 67 and Figure 4. 68 showed the maximum crystal size and crystal density at

500 °C for four alloy compositions. It can be observed that Cu and Nb alloying addition individually reduced the crystal size and increased the nucleation density. Combined additions can reduce the crystal size and crystal density further which indicates there are synergistic effects between Cu and Nb alloying additions facilitating the formation of nanocrystal.

By means of VSM the saturation magnetization and coercivity of the four alloy compositions after annealing at different temperature and time were measured and the results are described in the following section.

4.8 Magnetic properties

The annealing temperature and time dependence of saturation magnetization and coercivity of the four alloy compositions were measured by VSM and results are shown in Figure 4. 69 to Figure 4. 74. The saturation magnetization, coercivity and hysteresis loss of four alloys after heat treatment at 550 °C for 5 min, 30 min, 1 h, 4 h, 8 h, 16 h and 24 h are shown in Figure 4. 69 to Figure 4. 71, the saturation magnetization, coerciverty and hysteresis loss after heat treatment at 420 °C, 490 °C, 500 °C, 515 °C, 550 °C, 600 °C, 640 °C for 1 h are shown in Figure 4. 72, Figure 4. 73, and Figure 4. 74 respectively.

The saturation magnetization was the highest (1.65 T) for the Fe-Si-B alloy and the coercivity is smallest for the Fe-Si-B-Cu-Nb alloy after heat treatment for 1 h. During subsequent crystallization the coercivity of the Fe-Si-B and Fe-Si-B-Cu alloy increased dramatically to more than 3000 A/m. Annealing time had only a small effect on the

coercivity of the Fe-Si-B-Nb and Fe-Si-B-Nb-Cu alloys. Hysteresis loss of the Fe-Si-B alloy is the highest and that of the Fe-Si-B-Nb-Cu alloy is the lowest after annealing for 4 h.

As the annealing temperature increased from 420 °C to 640 °C the highest magnetization is observed in the Fe-Si-B alloy (1.7 T) while the Fe-Si-B-Nb-Cu alloy has the least magnetization (1.3 T). For annealing temperature less than 550 °C the coercivity is highest in the Fe-Si-B alloys (more than 6 kA/m), while the Fe-Si-B-Nb-Cu alloy has the lowest coercivity. Cu alloying addition did not change the trend but decreased the magnetization and coercivity. Nb alloying addition reduced the degree of the changes of Ms and coercivity as the annealing temperature was increased from 550 °C to 640 °C. Individual Cu or Nb alloying additions decreased the hysteresis loss, combined additions reduced the hysteresis loss further as the annealing temperature was increased from 490 °C to 640 °C.

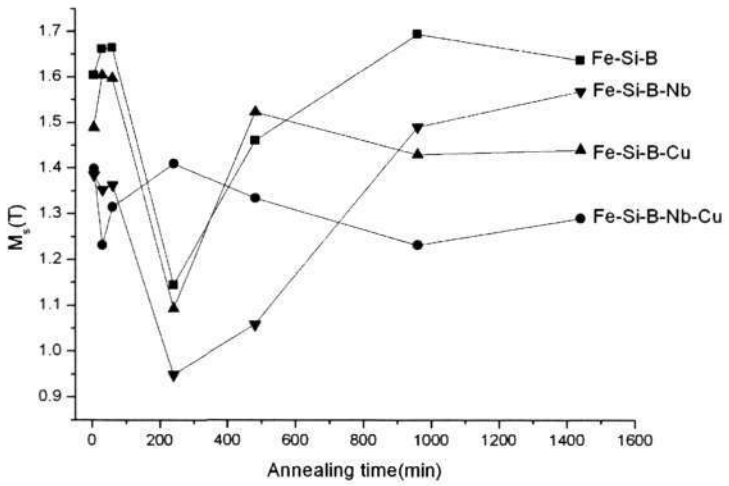

Figure 4. 69 Magnetization dependence on annealing time at 550 °C

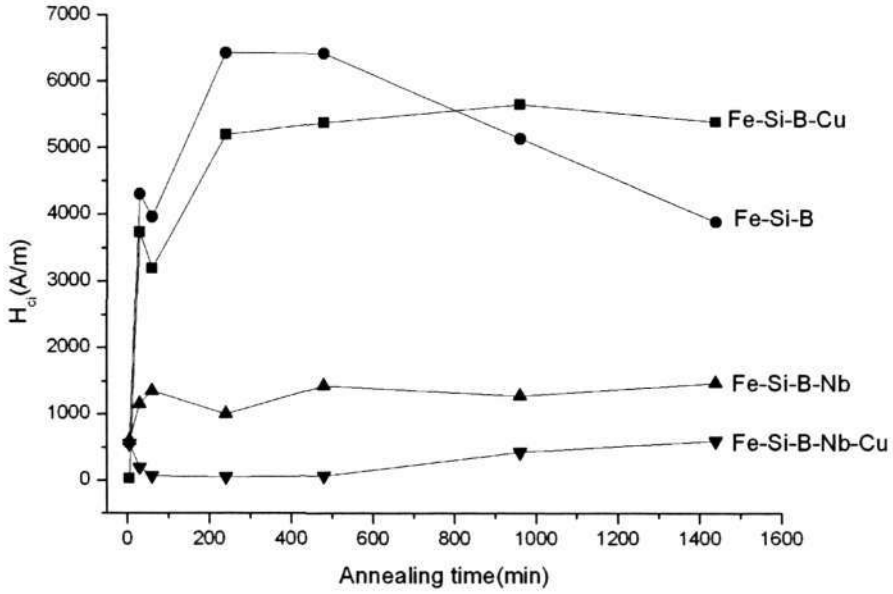

Figure 4. 70 Coercivity dependence on annealing time at 550 °C

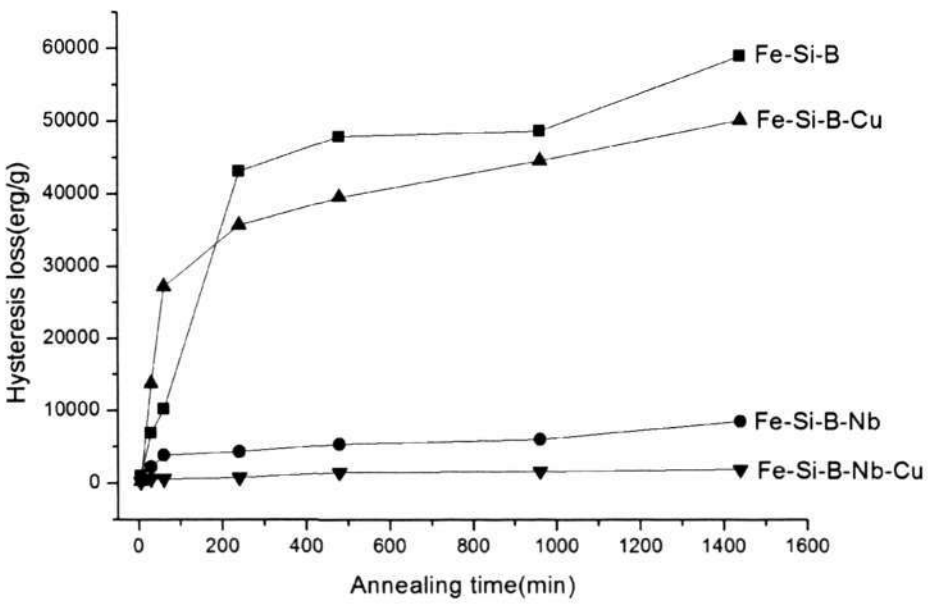

Figure 4. 71 Hysteresis loss dependence on annealing time at 550 °C

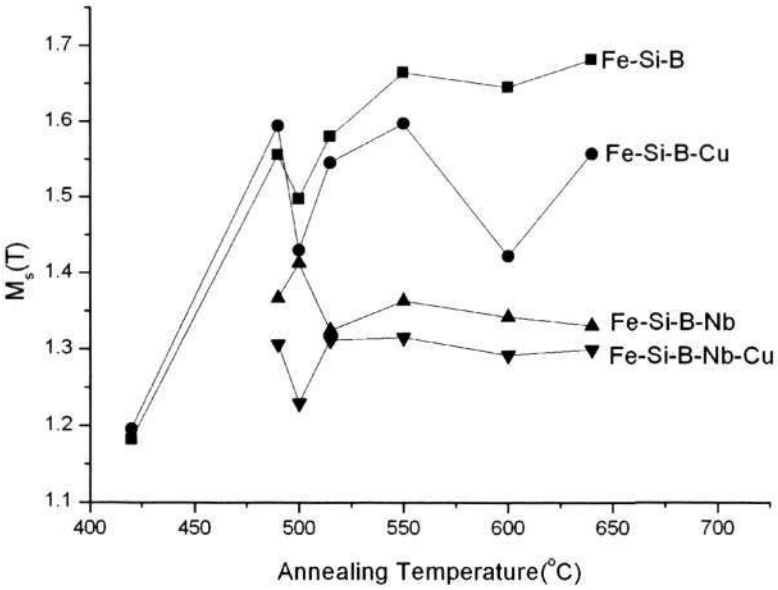

Figure 4. 72 Magnetization dependence on annealing temperatures for 1 h

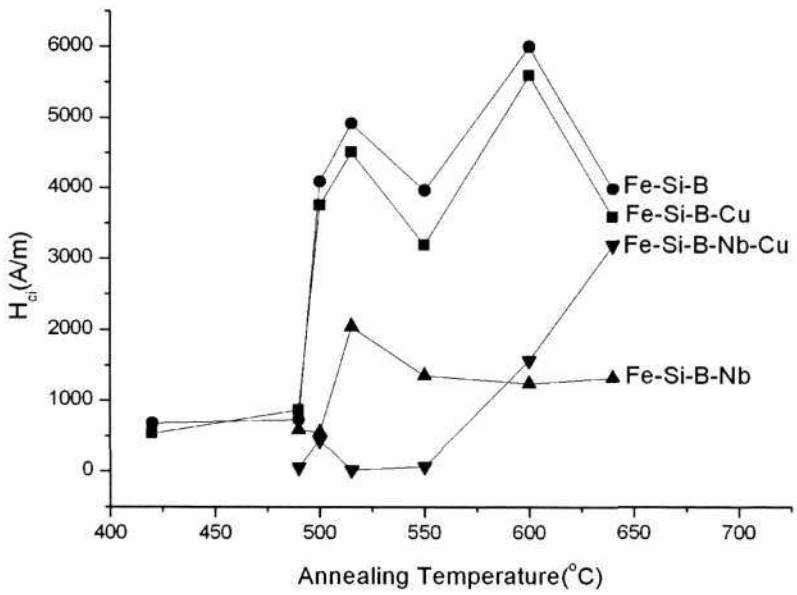

Figure 4. 73 Coercivity dependence on annealing temperatures for 1 h

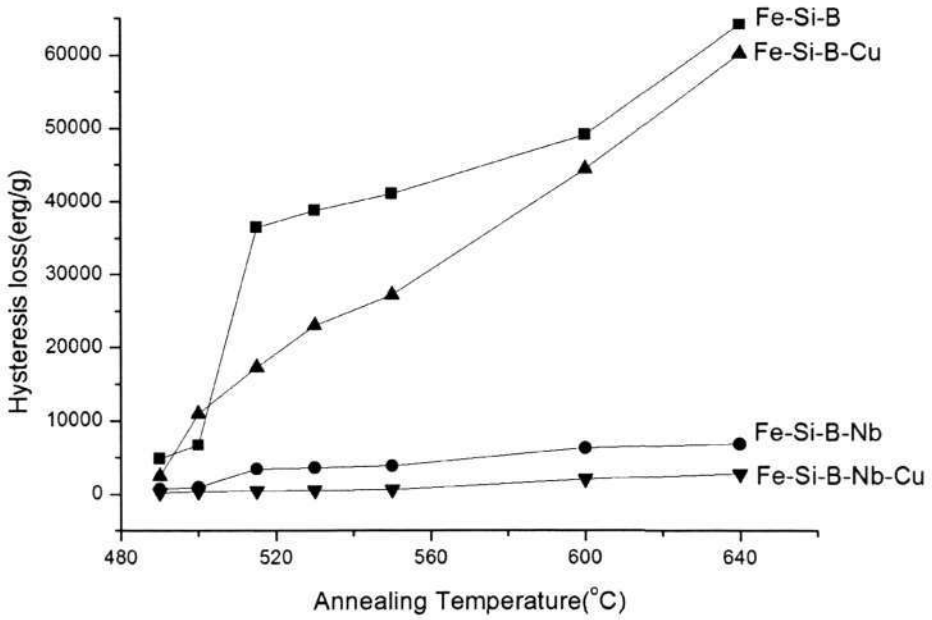

Figure 4. 74 Hysteresis loss dependence on annealing temperatures for annealing time of 1 h

The next chapter will discuss the results described in this chapter regarding the crystallization behavior of the four Fe-Si-B based alloys. The individual and combined effects of 1 at% Cu and 3 at% Nb alloying additions in the Fe-Si-B alloys on the thermal properties, crystallization behavior and magnetic properties will be discussed. Subsequently, the role of Cu and Nb alloying additions of nanostructure formation will be understood.

Chapter 5 DISCUSSION

The experimental results of the four alloys will be discussed in this part and the effect of the individual and synergistic effects of Cu and Nb alloying additions on the thermal properties, crystallization behavior and magnetic properties will be elucidated.

5.1 Analysis of $Fe_{77.5}Si_{13.5}B_9$ alloy

5.1.1 Thermal properties

The DSC curve of the $Fe_{77.5}Si_{13.5}B_9$ alloy exhibited two exothermic peaks at 527 °C and 552 °C (at a heating rate of 10 K/min) corresponding to the formation of the Fe-Si phase during primary crystallization and a Fe-B compound during secondary crystallization. Other researchers have suggested that there are three stages during crystallization of the Fe-Si-B amorphous alloy [96,97]. Due to the decomposition of the Fe_3B phase into the Fe-Si and Fe_2B phases. However, this process occurred almost simultaneously with secondary crystallization so the peaks overlap and only two peaks could be distinguished in the DSC results.

The DSC data also showed that the gap between the two peaks is narrow, indicating that once crystallization began, it is difficult to arrest the process precisely at a predetermined fraction of crystallization phase. As the heating rate increased from 2 K/min to 20 K/min, the crystallization temperatures shift to higher temperatures, as expected from the thermal activation processes required for crystallization. In addition, the calculated activation energy of the crystallization is 376±5.9 kJ/mol for the first crystallization process and

341.8±38.7 kJ/mol for the second crystallization event. Compared with a $Fe_{78}B_{13}Si_9$ alloy for which the activation energy of the first and second crystallization has been reported to be 445.2 kJ/mol and 323.4 kJ/mol respectively, the activation energy of the crystallization for the $Fe_{77.5}Si_{13.5}B_9$ alloy was lower [98,99]. This indicated that with Si replacing B in the alloy, the amorphous matrix will be destabilized which is consistent with the conclusions of earlier reports [100]. It was also observed that primary crystallization has a higher activation energy compared to secondary crystallization, partly because the formation of the Fe-Si phase resulted in boron being rejected to the amorphous matrix, the matrix thus becomes boron rich which facilitates the formation of the Fe-B compound which appears during secondary crystallization.

5.1.2 Crystallization behavior

Primary crystallization occurred at 490 °C for 1 h, unusual solid state dendrites of the Fe-Si phase were observed(Figure 4. 6). A dendritic morphology has been previously observed during crystallization of the Fe-Si-B alloys[101,102,103], However, the observation of closely spaced crystals forming the dendrite braches has not been previously described. The formation of the dendritic morphology in the Fe-Si-B alloy is due to constitutional supercooling which resulted in interfacial instability, facilitating the formation of dendrites. This supercooling resulted from the composition difference between the matrix and crystal during crystallization. This composition difference can be observed in the EDS measurements at the interfaces between the closely spaced crystal and the matrix, as shown in Table 4. 1. The Si concentration in the matrix is about 3 at% higher than that in the closely spaced crystals. Similarly, B was also clearly observed by

EELS to be rejected to the matrix. Hence, due to Si and B solute rejection, the region ahead of the crystal is constitutionally supercooled. This leads to the instability of the interface between the matrix and the crystal which facilitates dendrite formation.

A difference between the present findings and earlier reports is the unusual branches of these dendrites which are composed of several independent but closely spaced crystals instead of a single crystal [101-103]. The spacing between the crystals was in the nanometer range. This suggested that such closely spaced crystals form by a process similar to sympathetic nucleation and growth. This unusual morphology of the dendrites may be due to the higher Si content in the present alloy compared with previous investigations [101-103]. It has been reported that the solubility of B and Si in α-Fe at 490 ^{o}C is about 0.01 at% and 10 at% respectively [104,105]. The solubility of Si in Fe is much higher than that of boron. Thus, compared with the $Fe_{78}B_{13}Si_{9}$ alloy, due to the substitution of B by Si in the $Fe_{77.5}Si_{13.5}B_{9}$ alloy a higher concentration of Si is present in this alloy. The growth of the dendrite branch is diffusion controlled and the lengthening of the branches of the dendrites requires diffusion of both Fe and Si atoms. While diffusion in amorphous alloys can take place by some form of cooperative motion of groups of atoms [101], the affinity between Fe and Si atoms is stronger than that between two Fe atoms [104,105]. Thus, it is suggested that the Si atoms act as a drag force reducing the diffusion rate of Fe atoms, hindering the dendrite growth. The nucleation of new crystals at a short distance from the earlier crystals is therefore favored, giving rise to closely spaced crystals.

More interfaces were created due to these closely spaced crystals which comprised the branches of the dendrites. In order to reduce the total interfacial energy of the system, secondary crystallization was found to occur not only in the matrix between the dendrite branches but also between the closely spaced crystals (as shown by the arrows in Figure 4. 9). The crystal: matrix interfaces provide preferential nucleation sites for the formation of the Fe-Si and Fe_3B phases.

In order to obtain a better understanding of the crystallization process of the $Fe_{77.5}Si_{13.5}B_9$ alloy more observations were made to identify the phases surrounding the dendrite. The secondary crystallization products exhibit a striped morphology (Figure 4. 10) which is different from the lamellar structure reported by Bhatti [102]. Combining the TEM and XRD results the phases formed in the secondary crystallization products are not only Fe-B compounds such as Fe_3B phase, but also the Fe-Si phase. The Fe-Si phase was found to posses a B2 ordered structure, this crystal structure of the Fe-Si phase has not been previously reported in the Fe-Si-B amorphous system. As crystallization proceeded, the volume fraction of the products of secondary crystallization increased at the expense of the amorphous matrix. At the same time, secondary crystallization independently occurred at the interfaces between the closely spaced crystals, thus the dendritic morphology was broken up by the secondary crystallization products. At the end of the crystallization process, the products were found to be the Fe-Si, Fe_2B and Fe_3B phases (bright arrow in Figure 4. 11 and Figure 4. 12). Large crystals of the Fe-Si phase were also observed(dark arrow in Figure 4. 11), this observation differs from earlier reports in a $Fe_{78}B_{13}Si_9$ alloy of a lamellar morphology consiting of Fe-Si and Fe_2B phases [101,

102].

5.1.3 Magnetic properties

The annealing time and temperature dependence of magnetization and coercivity (Figure 4. 69 to Figure 4. 73) showed that the as received amorphous alloy has a saturation magnetization of 1.3 T and the coercivity is about 60 A/m. After primary crystallization occurred the saturation magnetization increased due to the formation of the soft magnetic α-Fe-Si phase, the coercivity also increased due to structural relaxation. As the annealing time increased to 60 min, due to the increasing volume fraction of the Fe-Si phase the magnetization was enhanced while the coercivity remained almost unaltered. The saturation magnetization of the Fe-Si-B alloy is higher than that of the Finemet alloy, it may be possible to improve the soft magnetic properties if coercivity could be decreased. As the crystallization proceeds further to 240 min the magnetization decreased to 1.1T while the coercivity increased significantly from 3.7 kA/m to 6.5 kA/m, this could be due to the formation of the Fe_3B and Fe_2B phases which can increase the coercivity. Formation of the Fe-B compounds leads to an increase of magnetocrystalline anisotropy, as a result of which magnetic hardening takes place. Hysteresis loss increased as the annealing time increased (Figure 4. 71). After annealing at 500 °C the hysteresis loss increased sharply from 10000 erg/g at 1 h to 45000 erg/g at 4 h due to the formation of the Fe-B compound.

As the temperature increased from 490 °C to 640 °C the magnetization showed little change. The coercivity increased significantly at 515 °C due to the formation of the Fe_2B

and Fe_3B compounds for 1h (Figure 4. 5). The XRD observations showed that the occurrence of the Fe_3B phase appeared only after heat treatment at 515 °C for 60 min, matches well with the increase of coercivity. At 550 °C the coercivity decreased to 3.2 kA/m, this decrease is due to the increased volume fraction of the Fe-Si phase. As the crystallization proceeded further, the Fe_2B phase formed from not only by the decomposition of the Fe_3B phase but also from the amorphous matrix, thus the volume fraction of the Fe_2B phase increased greatly compared to the Fe-Si phase, resulting in an increase of coercivity. The hysteresis loss increased as the annealing temperature was increased (Figure 4. 74). As the annealing temperature was increased from 500 °C to 515 °C at 1 h the hysteresis loss increased sharply from 6000 erg/g to 36324 erg/g due to the formation of the Fe_3B phase.

5.2 Dendrite formation in the Fe-Si-B alloy

Concerning the formation of the solid state dendrites, Tiller [106] developed the well known constitutional supercooling criterion to determine the morphological stability of a planar interface during solidification in the binary alloy. But constitutional supercooling ignores the stabilizing effect of interfacial energy and therefore, is valid only at very low velocities. Mullins and Sekerka, taking into account interfacial energy, high velocity thermal effects and non-equilibrium effects, showed that a sphere is stable below and unstable above a critical radius Rc, which is just seven times the critical radius of nucleation theory [107,108].

A mathematical expressions for the diffusion field ahead of an isolated growing

paraboloid has been provided by Ivantsov[109] and is widely used to describe the growth of dendrites. The marginal stability theory, developed by Langer and Muller–Krumbhaar[110] was found to be in better agreement with experimental observations. This theory states that for a given temperature and composition the tip radius of a dendrite corresponds to the smallest unstable perturbation of a plane front. In this hypothesis the dominant factor for the stability of the dendrite was identified as the dimensionless parameter σ[111].

$$\sigma = \frac{2d_0 D}{\rho^2 v} \qquad \text{Eq.5. 1}$$

where d_0 is the capillarity length, ρ is the radius of curvature at the tip of the parabolic, D is the diffusion coefficient and v is the interface velocity. If the dimensionless parameter σ exceeds a critical value, the capillarity forces stabilize directional growth of the dendrite. If σ is less than the critical value the dendrite becomes unstable against protrusion forming deformations. Thus the dimensionless parameter σ, as the dominant factor of the stability of the dendrite, defines when the protrusion is marginally stable [111].

Here, in the case of chemical diffusion, d_0 is the chemical capillarity length defined by:

$$d_0 = \frac{\gamma \left| dC_L^* / dT \right|}{\Delta C^2 (L / T_m \Delta C + \partial \mu / \partial T)} \qquad \text{Eq.5. 2}$$

where γ is the interface energy, L is the latent heat of solution, ΔC is the composition difference between liquid and solid phase at the interface, T_m is the melting temperature, C_L^* is the composition of the matrix at the interface, and μ is the chemical potential of

liquid solution.

Figure 4. 14 to Figure 4. 18 show the development of the dendritic morphology. It can be concluded from in situ hot stage TEM observations that there is a critical value of the crystal size beyond which the equiaxed morphology will transform to the dendritic morphology. This is consistent with the theoretical analysis of Mullins and Sekerka that spheres undergoing diffusion controlled growth into a supersaturated matrix are unstable above a critical size [108]. The critical value of the crystal size is just seven times of the critical radius of nucleation theory. If the crystal size is larger than the critical size the sphere is unstable otherwise the sphere remains stable. The critical nucleation radius is estimated to be around 6 nm (Figure 4. 14), while the critical radius at which the dendrite formation occurred (at 500 ^{o}C for 306 s) when the radius of the crystal is about 45 nm (Figure 4. 15), consistent with Mullins and Sekerka's model. Although the Mullins and Sekerka's theory is developed for spherical morphology, later work by Nebsit and Langer shows that a similar analysis applies to the present case [111,112].

Nesbit suggested that supersaturation inhomogeneity is the main factor leading to directional growth [112]. During diffusion toward a growing crystal with a square shape, the supersaturation is not constant at all points on its surface or interface. Instead, the supersaturation is higher at the corners than at the faces. This supersaturation inhomogeneity becomes even more pronounced as the crystal continues to grow, and eventually it results in the square shape becoming unstable and forming directional growth in the direction of greatest supersaturaion and highest growth rate. Our

experimental observation of square shapes following annealing at 500 °C for 306 s (dark arrow in Figure 4. 15) substantiate these predictions. Due to the higher supersaturation of Si and B at corners compared with that at the face an unstable square shape is observed after 312 s(dark arrow in Figure 4. 16). Subsequent growth leads to the formation of dendrite of which four branches stretch out from corners of the initial square shape after 360 s(dark arrow in Figure 4. 17).

Boron has very little solubility in the α-Fe-Si phase, dendritic growth may be controlled by the diffusion of boron in the amorphous matrix. The diffusion coefficient of solute, D, was obtained from the Ivantsov equation[109]:

$$\frac{C_L^* - C_0}{C_L^* - C_s^*} = Pe^P \int_P^\infty \frac{e^{-t}}{t} dt \qquad \text{Eq.5. 3}$$

Where $P=\rho V/2D$, C_L^* is the boron composition at the interface, C_s^* is the boron composition of the matrix at the interface, C_0 is the initial boron composition of the matrix and D is the diffusion coefficient of boron in the matrix. The maximum crystal size as a function of annealing time was plotted in Figure 5. 1. These measurements could be used to calculate the growth rate.

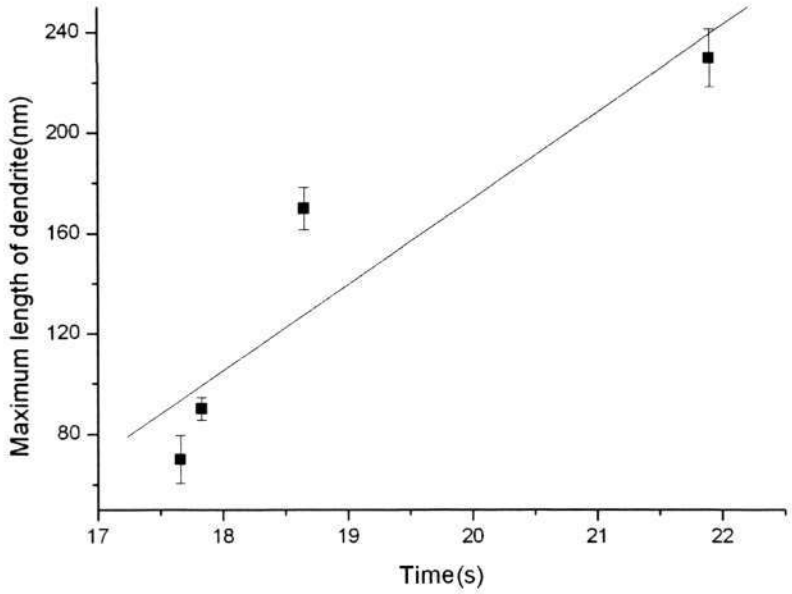

Figure 5. 1 Maximum length of the dendrite with time at 500 °C

The tip radius of dendrite(ρ) was calculated from the fitted parabolic curve and its value is about 18 nm, independent of annealing temperature[113]. Chang and Marti suggested that the maximum length of a dendrite is proportional to $\sqrt{t}$, where t is the annealing time[114]. Thus the growth rate can be estimated from Figure 5. 1. Other values are selected from refs [113,115]

Thus by inserting the D from Eq.5.3 and d_0 from Eq.5.2 the dimensional parameter can be calculated to be in the range: 0.013-0.031. This experimental results lies in the range of theoretical predictions: σ=0.025[111], σ=0.06[116] and σ=0.0195[117].

Hence the prediction made by stability theory for dendritic growth are broadly consistent with experimental observations of dendrite growth in this $Fe_{77.5}Si_{13.5}B_9$ alloy.

5.3 Effect of Cu alloying additions

5.3.1 Thermal properties

1 at% Cu alloying addition does not qualititatively change the DSC results compared to the base Fe-Si-B alloy, two peaks are again observed. The first peak corresponds to the formation of the Fe-Si phase and the second peak indicates the appearance of the Fe_3B compound. This analysis can be verified by the XRD data(Figure 4. 21). It was also observed in the DSC data that there was a significant lowering in the value of the first crystallization temperature from 507 °C to 456 °C when 1 at% Cu was added to the Fe-Si-B alloy, this can be attributed to local clustering associated short range order, this order lowers the configurational free energy of the nucleus [143]. The addition of Cu decreased the primary crystallization temperature by more than 60 °C, much more than that of the secondary crystallization temperature, indicating that Cu alloying additions changed the kinetics and thermodynamics of the first crystallization processes more significantly than those of secondary crystallization [118]. The calculated activation energy also supported this assumption, Cu alloying additions reduced the activation energy of the first crystallization even from 376±5.9 kJ/mol in the case of the Fe-Si-B alloy to 260±5.3 kJ/mol in the case of the Fe-Si-B-Cu alloy, while for the activation energy of secondary crystallization a reduction of only 73 kJ/mol was observed. Since Cu alloying additions decreased the primary crystallization temperature with little effect on the secondary crystallization temperature, Cu alloying additions increase the temperature region of metastable coexistence of the crystalline Fe-Si phase and the amorphous matrix[119].

5.3.2 Crystallization behavior

Cu clusters can serve as heterogeneous nucleation sites for the crystallization of Fe–Si crystals, thus the number density of Fe-Si crystals increased [97]. Importantly, however, the number density observed experimentally is much less than that in the Fe-Si-B-Nb-Cu alloy, which shows that synergistic effects between Cu and Nb must play a crucial role in increasing the nucleation density to the level observed in the Fe-Si-B-Nb-Cu alloy. This important aspect has previously not received much attention in the literature. Interestingly, the morphology of primary crystallization was also altered dramatically by Cu alloying addition although the phases formed after primary crystallization are the same [96]. As described earlier, in the case of the Fe-Si-B alloy the morphology of the primary crystallization product is a dendrite(with arm length of 100 nm) with branches composed of closely spaced individual crystals, while in the case of the Fe-Si-B-Cu alloy, instead of a dendritic morphology, spheroidal crystals about 50 nm in size were observed (Figure 4. 22 and Figure 4. 23).

For Fe-Si-B related alloy compositions different heating rates lead to different morphologies of the crystallization products [120,121]. Specifically, conventional heating at slow rates produced the dendritic morphology, but flash annealing at fast heating rates produced fine crystals with spheroidal morphology[122,123]. The enhancement of the nucleation rate and decrease of the growth rate at faster heating rates resulted in fine crystals with an equiaxed morphology (Figure 5. 2). Kulik suggested that at small crystal size the spheroidal morphology is favored, beyond a critical size interfacial stability develops resulting in a dendritic structure. This prediction was

directly confirmed by our in-situ hot stage TEM observation in Section 4.2. With Cu alloying addition the nucleation rate was enhanced which facilitated the formation of smaller crystals. Thus spheroidal morphology was favored by the addition of Cu to the alloy.

This morphological transition described in the previous section was also observed in the Cu containing alloy from in-situ hot stage TEM observations (Figure 4. 30 to Figure 4. 34). As discussed earlier there is a critical value of the crystal size beyond which the crystal interface becomes unstable, tending to form wavy interfaces [107]. The critical value of the crystal radius depends on the alloy composition and for the Cu containing alloy the critical value is about 130 nm[124], which should be about 7 times the critical nuclei radius [107]. From our in-situ TEM observations the critical nuclei radius is about 14 nm (Figure 4. 30) thus the critical size corresponding to the interface instability should be about 100 nm. As crystallization proceeds, the interface becomes unstable and rough when the crystal size reaches 100 nm which is consistent with our observations (Figure 4. 34). Secondary crystallization hindered further directional growth of the primary crystals.

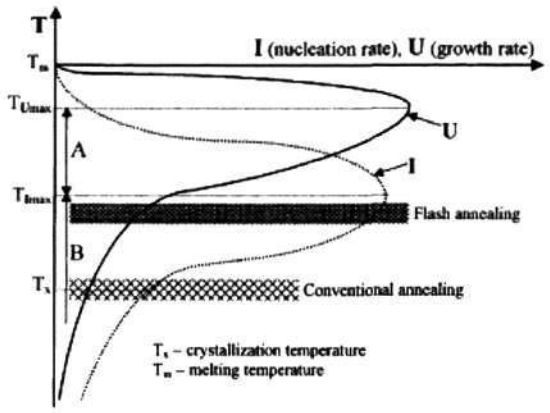

Figure 5. 2 Schematic diagram of the annealing temperature and heating rate dependence of nucleation rate I and growth rate U [124]

At 490 °C, more spheroidal crystals formed from the amorphous matrix and the volume fraction of such crystals increased. When the annealing temperature was increased to 500 °C, secondary crystallization was observed corresponding to the formation of the Fe_3B phase. This phase formed along the spheroidal crystal boundary in the form of a striped morphology (as shown by the arrows in Figure 4. 25), this morphology has not been previously reported. As the Fe-Si spheroidal crystals formed, boron was rejected into the matrix which is helpful for the formation of the Fe_3B phase.

As observed in Figure 4. 35 the nucleation density increased with annealing temperature. The nucleation density can be as high as $10^{21}/m^3$, which is significantly larger than $10^{18}/m^3$ usually observed in primary crystallization [103], confirming that Cu alloying additions increase nucleation density. The largest crystal size is found to increase with annealing temperature (Figure 4. 36). However, the largest crystal size initially increased dramatically with an increase in heat treatment time followed by a marked slowing down

in the growth as the crystallization proceeded, thus the growth of the α-Fe-Si crystals is found to deviate from the parabolic law usually observed in the primary crystallization.

Based on the DSC results and the measured nucleation density from in-situ hot stage TEM observation we can draw a schematic free energy curve to explain the effect of 1 at% Cu alloying addition (Figure 5. 3). With Si content at 13.5 at% the driving force for nucleation in Fe-Si-B alloy and Fe-Si-B-Cu alloy are ΔG_1 and ΔG_2, respectively. As the Cu alloying addition is increased from 0 to 1 at% the driving force for nucleation increases from ΔG_1 to ΔG_2, thus the nucleation will occur at lower temperatures, this is consistent with our DSC observations. In classical nucleation theory the homogeneous nucleation frequency I(t) at temperature T can be expressed as an exponential of the type:

$$I(t) = I_0(T)\exp\left[-(\alpha\sigma^3/\Delta G^2)/kT\right] \qquad \text{Eq.5. 4}$$

Where α is a geometric constant and σ is the free energy of the crystal-amorphous interface. 1 at% Cu alloying addition induces a higher driving force for nucleation resulting in a higher nucleation density in the Fe-Si-B-Cu alloy, which is consistent with our in-situ hot stage TEM observations.

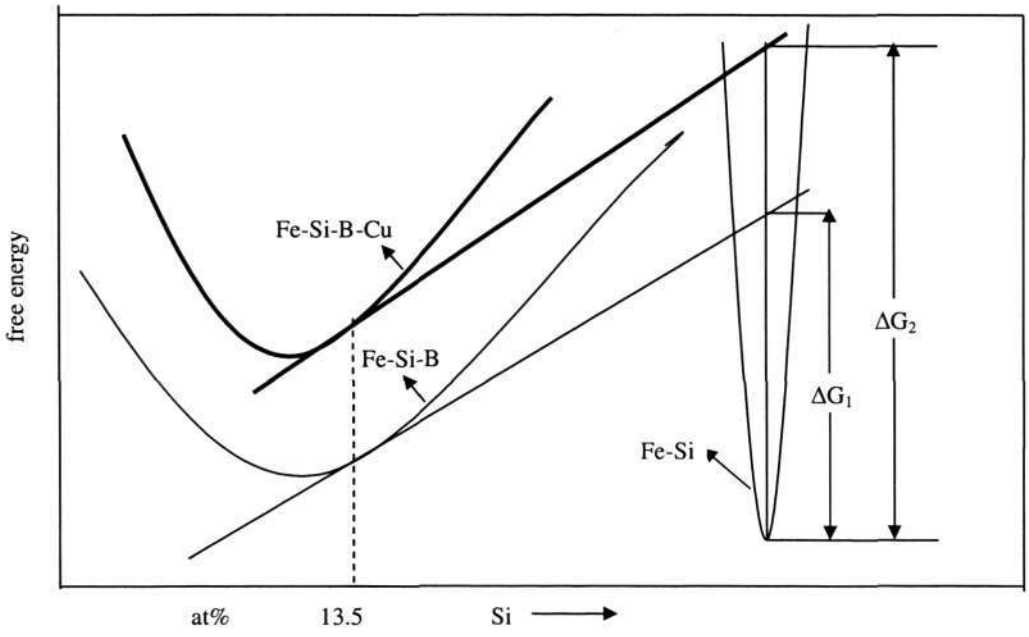

Figure 5. 3 Schematic drawing of the free energy G-curve for the amorphous matrix and the crystallization product

5.3.3 Magnetic properties

Cu alloying addition had a large effect on the magnetic properties. The magnetization and coercivity values of the Fe-Si-B and Fe-Si-B-Cu alloys showed similar trends after crystallization (Figure 4. 72 and Figure 4. 73). After annealing at 500 °C for 1 h Cu alloying additions were found to decrease the saturation magnetization and coercivity. Cu alloying addition decreased the hysteresis loss after annealing for 4 h (Figure 4. 71). As the annealing temperature was increased from 490 °C to 640 °C for 1 h the hysteresis loss was reduced by Cu alloying addition (Figure 4. 74).

When the alloys were heat treated at 420 °C for 1 h, crystallization occurred in the

Fe-Si-B-Cu alloy, however, the Fe-Si-B alloy remains amorphous. Due to the formation of nanocrystals of the Fe-Si phase which is a soft magnetic phase, the saturation magnetization of the Fe-Si-B-Cu alloy is higher than that of the Fe-Si-B alloy.

As the annealing temperature was increased further, the Cu alloying addition increased the saturation magnetization due to the greater volume fraction of the Fe-Si phase (Figure 4. 72), since the volume fraction of the Fe-Si phase in the Cu containing alloy is higher than that of the Fe-Si-B alloy. As the annealing temperature was increased from 490 °C to 500 °C, a sharp increase of coercivity was observed for both alloys. For the Fe-Si-B alloy dendrite growth increased the coercivity by providing additional obstacles to the motion of the domain walls. For the Fe-Si-B-Cu alloy the formation of the hard magnetic phase (Fe_3B) at 500 °C caused deterioration of the soft magnetic properties.

After secondary crystallization began at 500 °C the saturation magnetization decreased in the Cu containing alloy due to the formation of the Fe_3B phase. Formation of the Fe_3B phase leads to an increase of magnetocrystalline anisotropy, as a result of which magnetic hardening takes place [125]. At 500 °C the Fe-Si phase formed in both the Fe-Si-B and the Fe-Si-B-Cu alloys showed significant differences in morphology. In the case of the Fe-Si-B alloy, a dendritic morphology was observed, while with Cu alloying addition a spheroidal morphology with rough interfaces was observed. From shape anisotropy considerations the coercivity of the spheroidal morphology can be higher than that of the dendritic morphology [125], thus the coercivity is higher in the Fe-Si-B alloy compared with that of the Fe-Si-B-Cu alloy.

At 550 °C the saturation magnetization again increased due to Fe-Si phase formation resulting in a higher magnetization value and a lower coercivity value. When the heat treatment is conducted at 600 °C there was very little decrease in the magnetization for the Fe-Si-B alloy while there was a substantial decrease in the case of the Fe-Si-B-Cu alloy, this is due to the decomposition of the Fe_3B phase into the Fe-Si and Fe_2B phases, the Fe_2B phase lowered the saturation magnetization[126].

5.4 Effect of Nb alloying additions

5.4.1 Thermal properties

3 at% Nb alloying additions in the Fe-Si-B alloy altered the thermodynamics of the crystallization process. Nb alloying additions changed the crystallization mechanism from primary crystallization of Fe-Si phase in the case of the Fe-Si-B alloy to eutectic crystallization of Fe_3B and $Fe_{23}B_6$ phases in the Fe-Si-B-Nb alloy. This is consistent with the DSC results. Only one peak was obtained in the DSC curves of the Nb containing alloy which is consistent with a previous report that the range of the coexistence of the Fe-Si phase and the amorphous matrix was reduced by the addition of Nb and disappears with 3 at% Nb in the Fe-Si-B alloy[127]. However, the single peak in the DSC curve obtained in this investigation is different from the observation of two peaks reported by Yavari and Negri [11] and Mattern [128].

Regarding the crystallization temperature measured by DSC, it has been reported earlier that Nb concentration influences the onset of crystallization [129]. When 3 at% Nb was

added to the Fe-Si-B alloy, the peak shifts to higher temperatures from 506.6 °C in the case of the Fe-Si-B alloy to 580 °C in the Fe-Si-B-Nb alloy, which is consistent with the theory that in glasses of the type Fe-M-B-Si (where M is selected from a large number of metals), T_x is increased when the atomic size of M is larger than that of iron and decreased when it is smaller[130]. It has been reported that the atomic size of Fe and Nb atoms are 0.248 nm and 0.286 nm respectively[13], leading to higher T_x with Nb alloying addition. The higher T_x indicates that Nb stabilizes the glassy phase and makes it difficult to crystallize, consistent with previous reports [134,136]. This can also be observed from the values of the calculated activation energy, the activation energy of the Fe-Si-B alloy is about 376±5.9 kJ/mol while that of the Fe-Si-B-Nb alloy is 549±35.7 kJ/mol. This is consistent with the previous report that the enrichment of Nb atoms stabilizes the remaining amorphous matrix and suppresses the growth of the Fe–Si primary crystals [84]. In addition, the single peak is sharp and narrow, thus the crystallization process of the alloy containing Nb is difficult to control once it has begun.

5.4.2 Crystallization behavior

From the XRD results it was observed that the Fe-Si phase dominated as the crystallization proceeded in the case of Fe-Si-B alloy. With Nb alloying addition, in addition to the Fe-Si phase, the $Fe_{23}B_6$ and Fe_3B phases were formed (Figure 4. 39). As mentioned earlier, Nb alloying additions changed the crystallization mechanism from that of primary crystallization to eutectic crystallization. The phases formed as well as the morphology after crystallization was also dramatically different with Nb alloying addition. In the case of the Fe-Si-B alloy a dendritic morphology was observed after

primary crystallization, However equiaxed crystals were observed in the Fe-Si-B-Nb alloy (Figure 4. 40).

Figure 5. 2 shows that an enhancement of nucleation rate and decrease of growth rate resulted in fine crystals with an equiaxed morphology. A similar phenomenon can account for the morphology of Nb containing alloys, in which small equiaxed crystals were observed, compared with the larger size dendritic crystals in the Nb-free alloys. By reducing the growth rate by Nb additions, a smaller crystal size leads to an equiaxed morphology.

As explained in the previous section, in the Fe-Si-B alloy systems a dendritic morphology is observed when solute rejection during crystallization results in sufficient constitutional supercooling. The dominant factor which determines the stability of the matrix: crystal interface is the parameter $(G_l D)/(VC_0)$ [131]. G_l refers to the temperature gradient at the matrix: crystal interface, C_0 is the composition of the amorphous matrix, D is the diffusivity in the matrix and V is the growth rate. With Nb alloying additions the growth rate (V) was reduced greatly. Crystallization occurred at higher temperatures, thus the diffusivity in the matrix (D) was higher in the Fe-Si-B-Nb alloy compared with that in the Fe-Si-B alloy. Hence, the decrease of V and the increase of D facilitated the suppression of the dendritic morphology in the Fe-Si-B alloy, hence the equiaxed morphology was observed in the case of the Fe-Si-B-Nb alloy (Figure 4. 40). As the annealing time was increased from 30 min to 24 h the microstructure showed little change, unlike the usual case of eutectic crystallization in which the growth rate of a

crystal is independent of time [103].

It has been reported earlier that Nb appeared to induce the formation of the $Fe_{23}B_6$ phase when the amorphous phase is crystallized [132], Hampel also identified the $Fe_{23}B_6$ and Fe_3B phases by XRD techniques[133], Mattern suggested that the phase formed was $Fe_{60}Nb_{10}B_{30}$ [119]. However, these reports mainly deal with phase identification by XRD techniques, no TEM analysis and microstructural observations were reported earlier. Our HRTEM observation of the $Fe_{23}B_6$ phase (Figure 4. 41) suggests that the lattice parameter has a higher value of 1.073 nm compared with the value of 1.069 nm reported by Chen and Ryder which may be due to the presence of Nb atoms [134]. The $Fe_{23}B_6$ phase was found to possess an ordered f.c.c structure, Chen and Ryder [134] and Inoue and Takeuchi [135] have suggested a disordered f.c.c structure for this phase. The Fe_3B phase with a lenticular morphology and the corresponding SADP analysis are shown in Figure 4. 42. As suggested by the XRD results the volume fraction of the Fe-Si phase was found to increase with annealing time, the relative intensity of the highest peak of the Fe-Si phase to that of the $Fe_{23}B_6$ phase increased as the annealing time was increased from 30 min to 24 h.

The effect of Nb alloying addition can be rationalized by the schematic free energy curve shown in Figure 5. 4

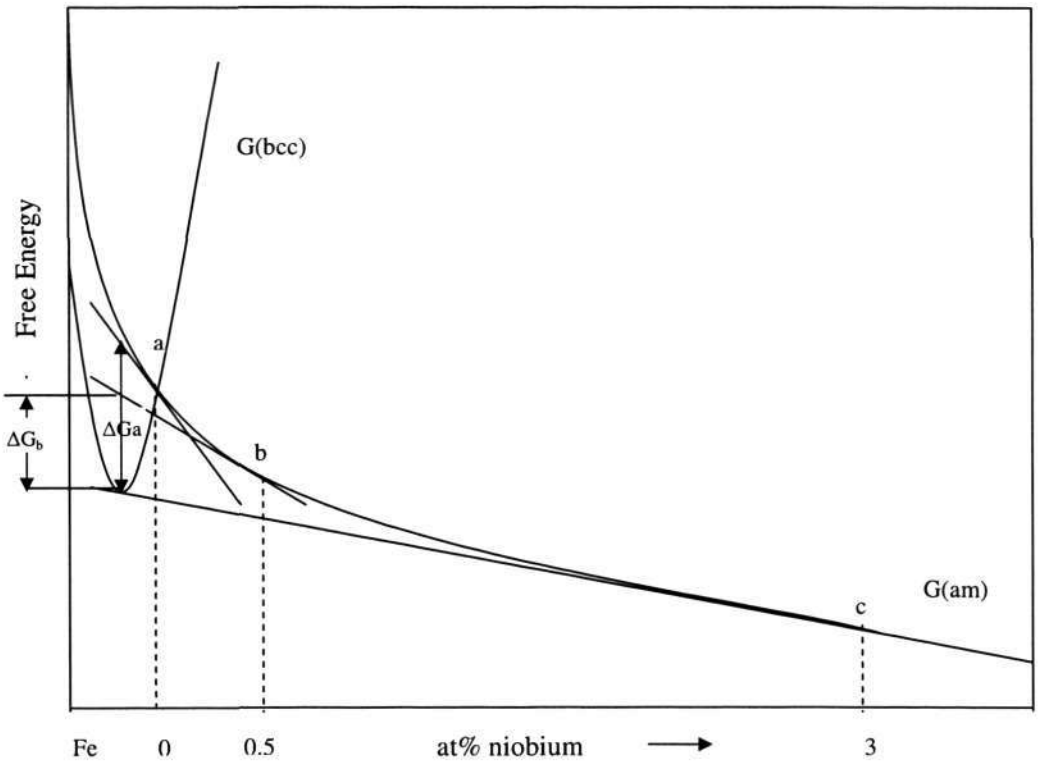

Figure 5. 4 Schematic drawing of the free energy G-curve for the amorphous and the crystallization b.c.c. phase dependence on Nb alloying addition

The alloy composition will determine the nucleation frequency and the growth rate. The values of ΔG relevent for nucleation in primary crystallization will be considered as the content of Nb alloying addition is increased from 0 to 3 at%. According to Eq.5.4 as the Nb alloying addition is increased from 0 to 3 at% the driving force ΔG for nucleation of the newly b.c.c. Fe-Si crystal decreases drastically, resulting in lower nucleation frequency I(T). At point 'a' no Nb is present and primary crystallization occurs, as observed in the Fe-Si-B alloy, and the value of ΔG for nucleation is represented by the value ΔG_a (Figure 5. 4). At point 'b' the Nb alloying addition is 0.5 at%, at this condition the crystallization temperature and the activation energy for crystallization increased which indicated that the driving force for nucleation was decreased[127], the value of ΔG

needed to evaluate the nucleation frequency is ΔG_b. For these two vaules of Nb content, primary crystallization occurred corresponding to the formation of the b.c.c. phase. As the Nb alloying addition was increased to 3 at%, ΔG becomes zero, the driving force for the formation of the b.c.c. phase is zero. The selection of which phase appears in the first stage of the crystallization is determined by the driving force for crystallization of each phase [6], thus $Fe_{23}B_6$ and Fe_3B phases form and subsequent growth becomes interface controlled. Thus eutectic crystallization occurred, consistent with our XRD and TEM observations.

5.4.3 Magnetic properties

Niobium alloying additions alter the saturation magnetization, coercivity and hysteresis loss after heat treatment were determined (Figure 4. 69 to Figure 4. 74). In the case of the Fe-Si-B alloy, as annealing time was increased to 1 h the saturation magnetization reached the maximum value of 1.7 T due to an increase in the soft magnetic Fe-Si phase. As the annealing time was increased to 4 h the saturation magnetization decreased dramatically, correspondingly the coercivity increased due to the formation of the Fe_3B phase. As the crystallization proceeded further the saturation magnetization increased to 1.6 T while the coercivity remains roughly constant. For the same annealing condition with Nb alloying additions, saturation magnetization was reduced compared with the corresponding value of the Fe-Si-B alloy. Regarding the soft magnetic properties of the $Fe_{23}B_6$ phase there are contrary reports. Hono and Ping suggested that the $Fe_{23}B_6$ phase is a soft magnetic phase and its formation does not adversely affect the magnetic properties[136]. However, Pandaa et al. assumed that the $Fe_{23}B_6$ phase has high magnetocrystalline energy resulting

in a degradation in soft magnetic properties [137]. As the annealing time was increased from 1 h to 4 h the saturation magnetization decreased sharply due to the decreased volume fraction of the soft magnetic $Fe_{23}B_6$ phase although the volume fraction of the soft magnetic Fe-Si phase increased, this can also be observed in the XRD data (Figure 4. 39). This is consistent with the $Fe_{23}B_6$ phase being a soft magnetic phase. Nb alloying addition reduced the hysteresis loss much more compared with that of Cu alloying addition in the Fe-Si-B alloy.

5.5 Effect of combined Cu and Nb alloying additions

5.5.1 Thermal properties

The addition of Cu destabilizes the amorphous Fe-Si-B phase, i.e. decreases the primary crystallization temperature. On the other hand, the addition of Nb shifts the crystallization temperature to higher values, i.e. the Nb stabilizes the glassy phase. However, the stabilizing influence of Nb is more than canceled when there is simultaneous addition of Cu. Although there is not a large difference between the temperatures of the first stage crystallization for the Fe-Si-B and Fe-Si-B-Cu-Nb alloys, the crystallization kinetics shown by the DSC plots are very different. For the Fe-Si-B alloy, the first crystallization peak is so sharp and narrow that, once crystallization has begun, it was difficult to arrest the process precisely at a predetermined fraction of crystalline phase. The first exotherm, related to nanocrystallization reaction in the Fe-Si-B-Nb-Cu alloy, is flatter and wider than those for conventional metallic glasses suggesting much lower kinetics of crystallization, probably due to a decrease in crystal growth rate[138].

For the $Fe_{73.5}Cu_1Nb_3Si_{13.5}B_9$ alloy, three peaks can be observed in the DSC curve. The first peak corresponds to primary crystallization of the nanocrystalline phase followed by two other exothermic peaks. The second and third peaks partly split and correspond to further crystallization of the residual amorphous phase, as well as to phase transformation to metastable phases, such as Fe_3B. Compared with the crystallization of the Fe-Si-B alloy, the range of the coexistence of Fe-Si and the amorphous matrix phase is extended by the combined Cu and Nb additions, and is shifted to higher annealing crystallization temperatures. The line broadening in the diffraction patterns indicates the small crystal size of the Fe-Si phase formed in this alloy. Thus the DSC result of the $Fe_{73.5}Si_{13.5}B_9Nb_3Cu_1$ alloy shows features favoring nanocrystallization, which is consistent with previous reports that Cu additions to amorphous Fe-based alloys containing Nb atoms will have tendency to phase-separate out of the glass facilitating a high density of crystals and subsequent crystallization [83,89]. Additions of Cu and Nb together with higher ΔT_x are favorable to soft-magnetic properties.

The activation energy calculated by Ozawa method is 360±40.1 kJ/mol(3.73±0.41 eV) which agrees well with the values ranging from 3.58 to 3.93 eV obtained by thermoelectric power (TEP) measurements and the values of 3.84 to 4.08 eV from Vickers microhardness (HV) [89].

The DSC measurements exhibit three peaks, the first one indicates the appearance of the Fe-Si phase, the second indicates the formation of the Fe_3B phase and the third corresponds to the decomposition of the Fe_3B phase into the Fe_2B and α-Fe phases, this

observation is consistent with the XRD results (Figure 4. 46). This finding is different from some earlier reports where the third peak in the DSC curve was attributed to the formation of a Fe-Si compound which segregates from the α-Fe solid solution [139, 140].

5.5.2 Crystallization behavior

As the annealing temperature and time increased, the Fe-Si phase dominated and the relative intensity of its peaks in the XRD patterns increased. Figure 4. 48(a) shows a high density of nanocrystals (about 12 nm in size) of the b.c.c. α-Fe-Si phase in the amorphous matrix. Compared with the other three alloy compositions the average crystal size in the Fe-Si-B-Nb-Cu alloy is much smaller. The first reason for the smaller size is that with a much higher nucleation density, the supersaturation is "shared" by more crystals, resulting in smaller crystal size. Secondly, for the Fe-Si-B-Nb-Cu alloy the stability of the residual amorphous matrix around the Fe-Si crystals increases due to the formation of Nb and B-rich regions in the matrix during crystallization [1,2]. Thus the activation energy of crystallization of the remaining amorphous matrix increases with increasing fraction of crystallites. This constrains the growth of the Fe-Si crystal and results in the formation of nanocrystals.

Secondary crystallization after heat treatment at 600 °C for 1 h resulted in the formation of the Fe_3B phase in the Fe-Si-B-Nb-Cu alloy. Regarding the phases formed at 600 °C for 1 h there have been many investigations with contradictory conclusions. Noh indicated that the Fe_2B phase formed at 600 °C, while He and Rixecker concluded that f.c.c Cu appeared at 600°C [141,142]. Using XRD techniques Chen did not find any sign of f.c.c.

Cu and the interplanar spacings and the Miller indices were obviously different from those of Fe_2B. Instead, Chen suggested that tetragonal Fe_3B precipitate appeared at 600 °C [134]. Our results, combining DSC, XRD and TEM data showed that the Fe_3B phase formed at 600°C, which is consistent with the work of Chen [134]. TEM observations showed that the Fe_3B phase had a striped morphology (Figure 4. 48(c) and (d)), as reported previously [134]. The dark field image was selected from the streaks in the SADP of samples heat treated at 600 °C for 60 min(circled), such streaks were not observed in the SADP of samples heat treated at 550 °C for 1 h. Importantly, as the annealing temperature was increased, the size of the Fe-Si crystals remains almost constant, consistent with earlier reports [4-6]. As the annealing temperature increased to 640 °C, the Fe_2B phase formed due to the decomposition of the Fe_3B phase, corresponding to the third peak in the DSC measurement.

The results showed that as the annealing time and temperatures were increased the phases formed according to the following sequence:

Fe-Si (after primary crystallization) →Fe-Si +Fe_3B (after secondary crystallization) →Fe-Si + Fe_3B +Fe_2B (further crystallization) →Fe-Si+Fe_2B

Figure 5. 5 which is a simplified, schematic isothermal plot of free energy vs. composition for the alloy containing boh Cu and Nb alloying additions [143]. The diagram indicates (1) a metastable equilibrium can exist which corresponds to the formation of the Fe_3B phas during secondary crystallization, (2) the volume fraction of Fe-Si phase increases with increasing Si content of the alloy, (3) as the crystallization

proceeds the boride Fe_2B phase forms in equilibrium with the Fe-Si phase.

The metastable, two-phase state of finely dispersed, nanocrystalline α-Fe-Si phase in an amorphous matrix can thus be understood in terms of free energy concepts. The kinetics of crystallization process will be modeled in Section 5.7.

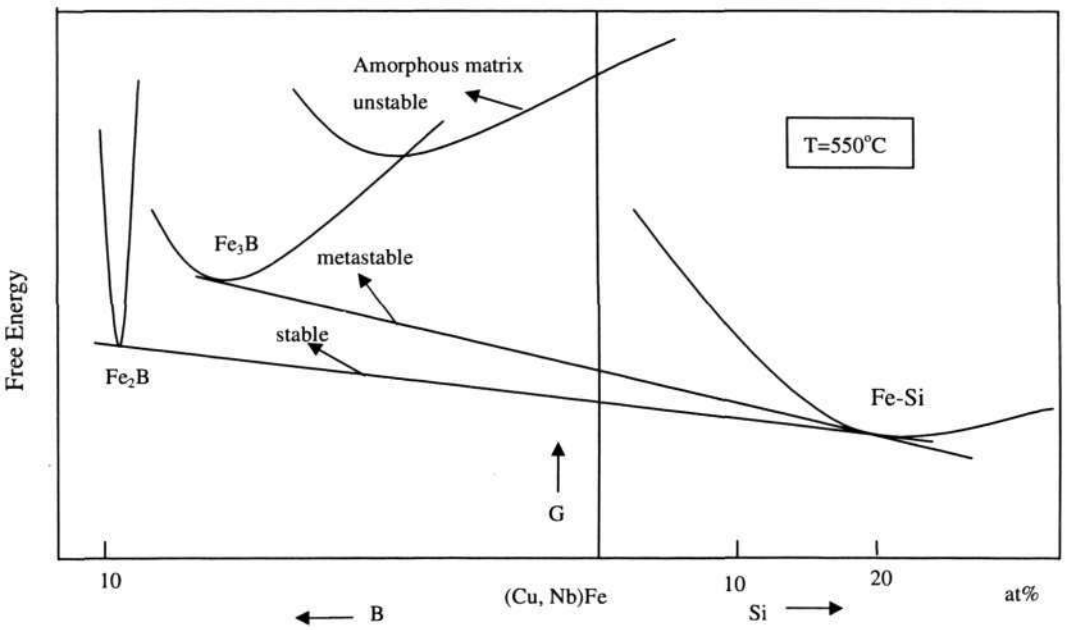

Figure 5. 5 Schematic free energy vs. composition diagram for the Fe-Si-B-Nb-Cu alloy

5.5.3 Magnetic properties

Addition of Nb alone, results in 60 nm α-Fe-Si crystallites, However, domain wall pinning by the boride phase occurs simultaneously, while addition of Cu alone, although increasing the nucleation frequency, does not retard the growth rate of the crystallites sufficiently. Good soft magnetic properties resulted when both Cu and Nb are solute elements, the magnetic softening of the Fe-Si-B-Nb-Cu alloy is a consequence of the increase in an number density and volume fraction of nanocrystals.

With both Cu and Nb alloying additions, as the annealing temperature was increased the coercivity increased from a low value at 490 °C to 500 A/m at 500 °C (Figure 4. 73). Cu-enriched clusters and a small volume fraction of α-Fe-Si crystals can act as pinning centers for domain wall displacements increasing the coercivity. An additional reason of magnetic hardening resulting from Cu segregation and initial nucleation of Fe-Si crystals would be the generation of local magnetoelastic anisotropy distributions within the amorphous phase [118]. At higher temperatures, the saturation magnetization increased due to the formation of a higher volume fraction of the Fe-Si crystals (Figure 4. 72). The volume fraction of crystals is much greater at higher temperatures, these crystals become coupled by exchange interactions and the correlation length increases substantially to about four times the crystallite diameter, averaging out and reducing the macroscopic magnetic anisotropies.

After heat treatment at 600 °C, the coercivity increased sharply due to the occurrence of secondary crystallization, resulting in the formation of the Fe_3B phase. These Fe_3B crystals reduce the local exchange length and, accordingly, produce a weakening of the intergranular magnetic coupling, thus the soft magnetic properties deteriorated [32]. As the heat treatment temperature was increased to 640 °C the saturation magnetization increased slightly while the coercivity increased due to the formation of Fe_2B phase from the decomposition of Fe_3B phase.

For a heat treatment temperature of 550 °C as the annealing time increased the saturation

decreased while coercivity increased to 200 A/m due to structural relaxation (Figure 4. 69). As the annealing time was further increased coercivity remained small while the saturation magnetization increased due to the increasing volume fraction of the Fe-Si nanocrystals. After the alloy was annealed at 550 °C for 4 h the coercivty remains small while the saturation magnetization reached the highest value of 1.4 T, higher than 1.24 T reported by Yoshizawa et al. after the same alloy composition was heat treated at 550 °C for 1 h [2]. After heat treatment for 8 h secondary crystallization occurred with the formation of the Fe_3B phase which caused a deterioration of the soft magnetic properties. The saturation magnetization decreased, as the crystallization proceeded further the coercivity increased further with a decrease in saturation magnetization.

Cu and Nb alloying additions individually reduced the hysteresis loss and their synergetic effects reduced the hysteresis loss further. Hence, it can be observed that the hysteresis loss is lowest in the Fe-Si-B-Nb-Cu alloy leading to good soft magnetic properties (Figure 4. 71 and Figure 4. 74).

5.6 Mechanism of Nanostructure Formation

Combined alloying additions of Cu and Nb resulted in nanocrystal formation and good soft magnetic properties, hence it is useful to understand the mechanism of nanostructure formation. It was observed that either Cu or Nb alloying additions alone cannot lead to nanocrystal formation. Firstly, it is clear that the addition of Cu alone is insufficient to induce the high nucleation density observed in the Cu and Nb containing alloy, suggesting the role of Nb in the nucleation is crucial. Secondly, the addition of Nb alone

is also insufficient to reduce the growth rate to the level observed in the Cu and Nb containing alloy. Finally, individual additions of Cu and Nb result in a different morphology compared to combined additions. Thus there should be synergistic effects between Cu and Nb alloying additions facilitating nanocrystal formation.

There have been numerous investigations of the effects of Cu and Nb alloying additions conducted [1-10], However, there is very little work on synergistic effects. EDS methods have been used to measure the distribution of the elements in the crystals and the amorphous phase [144]. However, in this work EDS, HRTEM and EELS mapping of B, Cu and Nb were utilized to measure the concentration profile in the vicinity of the nanocrystals to study which models are more consistent with experimental observations.

The formation of Cu-rich clusters just before or during the crystallization of amorphous $Fe_{73.5}Si_{13.5}B_9Cu_1Nb_3$ alloy has been observed by APFIM [64]. The crystals were found to be a few nanometers in diameter, containing 20-60 at% Cu. EXAFS measurements of the Cu and Fe Kα edges in refs. [8] and [9] showed that the Cu in the annealed alloy is not incorporated into the b.c.c. lattice of the Fe-Si phase formed, this observation agrees with the negligible solubility of Cu in b.c.c. Fe-Si. Using XRD techniques, Mattern concluded that f.c.c. Cu clusters are less than 5 nm in size, and that at least a fraction of the Cu atoms are still situated in the amorphous matrix phase [119]. Our EELS results for Cu elemental mapping show that Cu clusters are formed in the initial stage of the crystallization, the size range is from 1 nm to 10 nm(Figure 4. 53(b)), which is consistent with previous reports[8,64,119].

As has been reported, the number of crystals per unit volume is also strongly correlated with the concentration of Nb. The crystal density after annealing at 500 °C is enhanced by one or two orders of magnitude in the alloys with 3.0 at.% Nb[119]. Our EELS results for Nb(Figure 4. 53(c)) show that this increase in nucleation density is due to Nb rich regions which can also serve as nucleation sites.

It has been suggested earlier that there is no interaction between Cu and Nb atoms and no driving force for alloying or compound formation [5]. It has been reported that Cu clusters form as soon as the decomposition begins in the Finemet alloy but not in the Nb free alloy [145], and that the presence of Nb promoted the formation of Cu rich clusters [8]. Thus Nb alloying addition will increase the formation of Cu clusters, a synergistic effect that is supported by our experimental results.

The opposite trends of Cu and Nb concentration profile indicated that there is repulsion between Cu and Nb atoms consistent with the Cu-Nb phase diagram showing limited solubility of Nb in Cu [146](Appendix i). It has also been suggested by Hunziker[16] that two solutes with atomic radii both larger than the solvent will tend to repel each other, and since the atomic radii of Nb and Cu solutes are larger than the Fe solvent, Nb and Cu will repel each other resulting in Nb and Cu rich regions. These chemically different regions lead to regions with different chemical potentials and thus with different thermodynamic stability, which is helpful for the formation of Cu and Nb clusters.

Duhaj suggested that the decisive factor influencing the formation of the nanocrystals was the existence of medium-range ordered (MRO) clusters with definite chemical composition in the as-quenched amorphous structure, such clusters increase in size upon annealing and act as embryos in the nucleation process [10]. This suggestion implies that these domains (or clusters) can differ in chemical composition from the matrix[147]. Thus during initial annealing condition, both Cu and Nb rich regions can serve as nucleation sites.

In the regions with low crystal density (Figure 4. 49 and Figure 4. 51) Nb clusters can act as nucleation sites due to the strong attractive interaction between Si and Nb atoms. Such an interaction is suggested by the Hunziker's model, which suggested that when one solute has an atomic radius larger than the solvent and the other has an atomic radius smaller than the solvent, they will tend to attract each other. It has also been suggested that local clustering associated with b.c.c. like topological short range order lowers the configurational free energy of the nucleus [143], thus, the b.c.c structure of Nb and Fe also facilitates the formation of Nb rich regions serve as nucleation sites for the Fe-Si crystals. This is consistent with our experimental observation that Nb content is higher in the center than at the interface of the nanocrystal [11]. Due to the repulsion of Cu and Nb elements Cu was rejected by the formation of the Nb clusters, thus the Cu concentration is higher at the interface. During the growth process, according to Hunziker's model, the interaction of solute elements can strongly influence growth rate[16]. Diffusive interaction also occurs when the mobility of one of the solutes is much smaller than the other leading to the formation of two distinct boundary layers of very different extents

which will hinder the crystal growth. Thus due to the diffusive synergistic interaction between Cu, Nb, B, Si atoms at the interface the growth rate can be reduced.

In regions with high crystal density (Figure 4. 50 and Figure 4. 52) the content of Cu is much higher in the center which is consistent with earlier reports that the copper clusters are often enveloped within nanocrystals, indicating that Cu clusters initially formed in the amorphous phase, followed by nucleation and growth of the Fe-Si phase on the clusters [8]. A higher Nb content was observed in the regions between the nanocrystals is consistent with the soft impingement model of reduction of growth rate [14]. During crystallization, Nb and B atoms were rejected in the amorphous matrix (Figure 4. 54 and Figure 4. 55), thus, B and Nb concentrations around the crystal are higher than within the crystal, which is consistent with Hermann's model that Nb-B aggregates are responsible for the inhibition of growth[13]. Our experimental results suggest that soft impingement and Nb-B aggregates play crucial roles in reducing crystal growth.

On the other hand, it was observed that Cu alloying addition reduces the crystal size and increases the crystal density (Figure 4. 67 and Figure 4. 68) which is different from Hermann's conclusion that Cu does not influence the density of nuclei [13]. Cu alloying additions also reduce the crystal size by diffusive interaction between Cu, Nb, B, Si atoms according to Hunziker's theory. Nb alloying addition results in a smaller crystal size due to its low diffusivity and by increasing the crystal density. This indicates that Nb and Cu alloying additions influence both the nucleation and the growth process. From Figure 4. 67 and Figure 4. 68 the additions of both Cu and Nb induce the smallest crystal size and

highest crystal density compared with other alloys without any alloying addition or only with Cu or Nb alloying additions. Thus it can be shown that Cu and Nb alloying additions can synergistically increase the crystal density, support the nanostructure mechanism based on EDS and EELS results. Hence Cu and Nb alloying additions play a crucial role both in nucleation and growth stages, which is different from Hono's model [4].

The concentration profile of Fe, Si, Nb and Cu elements in region with low and high crystal density were measured by EDS techniques and EELS maps. Based on these results and the microstructural observations the following mechanism of nanostructure formation in the $Fe_{73.5}Si_{13.5}B_9Nb_3Cu_1$ alloy is suggested:

The repulsion of Cu and Nb atoms leads to the formation of Cu and Nb rich regions, both these regions can act as heterogeneous nucleation sites, leading to the high crystal density. Regarding the retardation of growth in regions with low crystal density, the growth rate was reduced, as suggested by the Hunziker model, by the strong interaction of Cu, Si, Nb and Fe atoms. In regions with high crystal density, soft impingement and Nb-B aggregates resulted in inhabition of the crystal growth.

5.7 Modeling of the crystallization behavior of melt spun $Fe_{73.5}Si_{13.5}B_9Nb_3Cu_1$ alloy

During primary crystallization, the composition of the matrix changes during the growth process. For instance, alloying elements, such as B, were rejected into the matrix during crystallization. Thus the free energy difference between the crystal and the amorphous

matrix also changes, so that the corresponding driving force for crystallization is then dependent on the fraction already transformed [148]. Using Eq.2.7 (Section 2.5.1) the Avrami exponent n and kinetic constant K for the heat treated samples for various annealing times are plotted (Figure 5. 6) and the values are listed in Table 5. 1, interestingly, a very low value of Avrami exponent n was found.

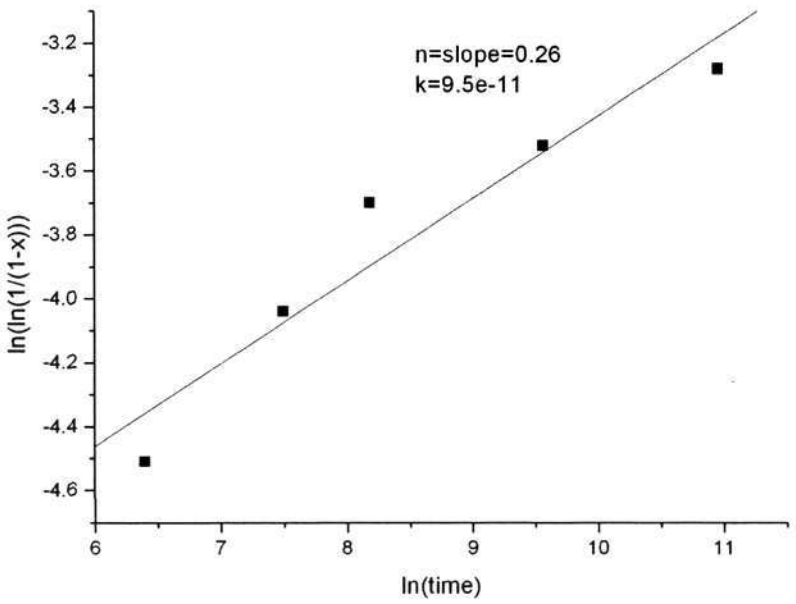

(a)

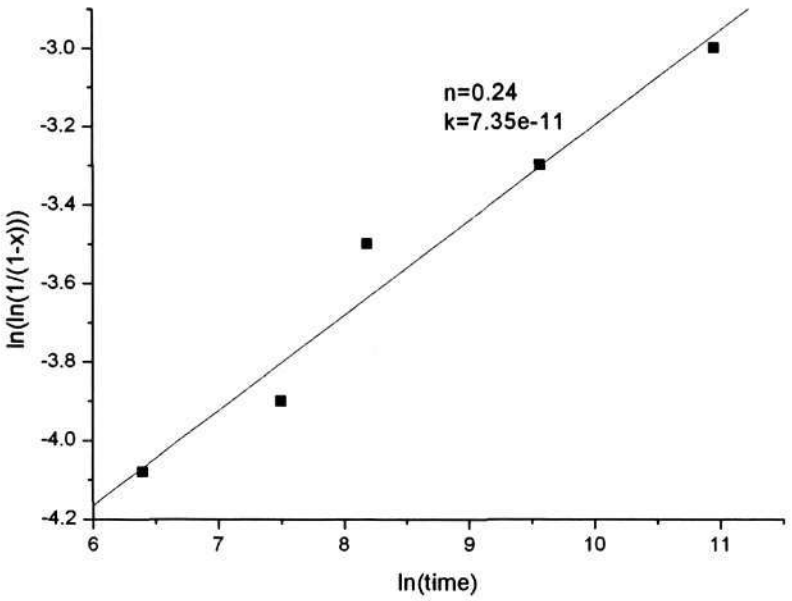

(b)

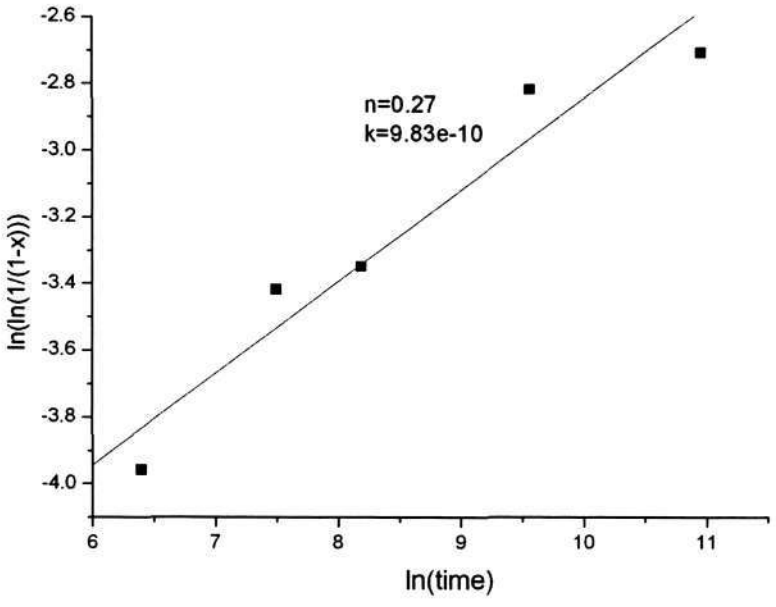

(c)

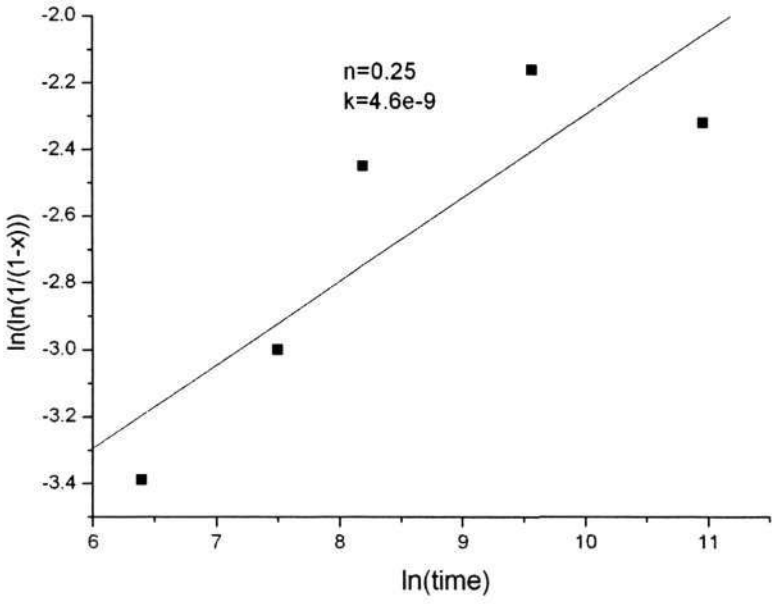

(d)

Figure 5. 6 JMA plot of samples heat treated at (a) 500 °C, (b) 515 °C, (c) 530 °C, (d) 550 °C as a function of ln(time)

Table 5. 1 The Avrami exponent n and kinetic constant K for the annealed samples

Temperature(°C)	Avrami exponent n	Kinetic constant K
500	0.26	9.50×10^{-11}
515	0.24	7.35×10^{-11}
530	0.27	9.83×10^{-10}
550	0.25	4.60×10^{-9}

According to Eq.2.6 the activation energy can be calculated by plotting lnK against $\frac{1}{T}$ (Figure 5. 7). As is shown in Figure 5. 7 the activation energy is 473±35.2 kJ/mol, higher than that calculated by Ozawa method: 360±40.1 kJ/mol.

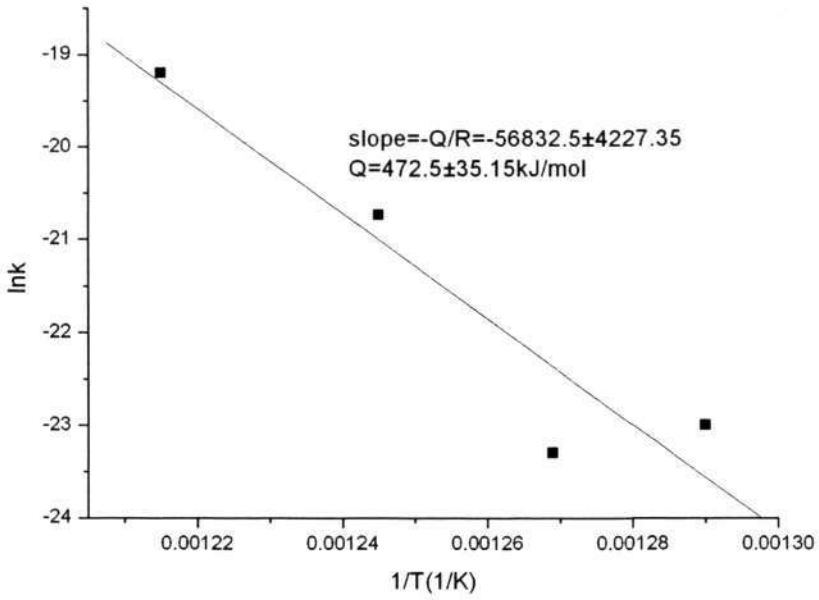

Figure 5. 7 Arrhenius plot of kinetic constant K

The Avrami exponent, n, depends on the dimensionality of the transformation, whether the transformation is interface or diffusion controlled and on the nucleation rate. Assuming constant or decreasing nucleation rate and isotropic growth, one obtains $3<n<4$ for interface controlled and $1.5<n<2.5$ for diffusion-controlled transformations [13,16]. Recently, x-ray[149], Mossbauer[133] and DSC [60]investigations of the crystallization of the amorphous alloy Fe-Si-B-Nb-Cu alloy have been discussed in terms of the JMAK model and have led to the conclusion that Avrami exponents $n<1$ are typical for this type of alloy.

Illekova explained these low values of n using the NGG model with m (the crystal growth exponent) equal to 2, which is consistent with parabolic growth rate dependence on the holding time[60]. According to Eq.2.12 the exponent $1/m$ is the slope of the $ln[1-a(t)]$ vs.

$ln(t+\tau_{GG})$ curve, where τ_{GG} is the quantity which is added to the experimental time t to linearize the dependence. We obtained a large crystal growth exponent equal to 120 hence this NGG model cannot be used to explain the abnormal low Avrami exponent.

Pradell[58] proposed that soft-impingement resulting from an overlap of Nb concentration profiles is responsible for the anomalous low Avrami exponent. In his model a microstructural dependence of crystal growth is introduced, as a consequence of crystal interaction typical of partitioning transformations, where the crystal has a different composition from the matrix in which it develops. Normally, partitioning transformations result in the presence of concentration gradients of several solutes at the interface of the crystals, the growth rate being limited by the slowest-diffusing specimen [11]. However, as crystallization proceeds, the diffusion profiles of neighboring crystals begin to overlap to an appreciable extent (soft impingement), giving rise to a further decrease in the growth rate because of the reduction in the concentration gradient [15]. A decreasing nucleation rate should also be expected in such transformations, since the composition of the matrix changes as crystallization proceeds, resulting in a stable remaining amorphous matrix. This effect of decreasing nucleation and growth rate due to soft impingement is useful to explain the Avrami exponent value.

On the other hand, Hampel[133] attributed the small Avrami exponent to Cu alloying addition. Cu alloying addition increased the quenched in nucleation sites which accelerates the nucleation of primary crystallization, thus in the ideal case no energy is needed for nucleation (athermal nucleation) and n_n will to be zero. This athermal

nucleation is accompanied by thermally activated nucleation which yields n_n between zero and one. The crystal growth is inhomogeneous because in an amorphous alloy if the local distribution of atoms changes, crystal growth will also be affected since crystal growth is dependent on the local composition. Therefore values of $n_g < 1$ may occur. $n=n_n+n_g$ should be less than 1. Thus the low Avrami exponent can be attributed to a higher nucleation density, low growth rate and soft impingement.

Hermann assumed that clusterlike arrangements of nuclei cause a decrease of n in comparison with the random homogeneous(JMAK) distribution[75]. From our EELS maps for Cu and Nb at the initial stage of crystallization, it can be observed that Cu and Nb rich regions served as nucleation sites for the formation of the Fe-Si crystals. Thus the formation of the Cu and Nb rich regions can also lower the value of the Avrami exponent.

In regions with high crystal density, Cu alloying addition increased the nucleation rate for primary crystallization, leading to a low activation energy for nucleation, thus n_n should be less than 1, consistent with Hampel's assumption[133]. As suggested by Hermann a decrease of the nucleation rate with growing volume fraction of crystals is caused both by a decreasing volume fraction of amorphous regions and by an increase of concentration of crystallization inhibitors in the remaining amorphous matrix. Increasing the Nb content in the remaining amorphous matrix will reduce the nucleation rate. The growth rate was also decreased by Nb which induced soft impingement and the Nb-B aggregates outside the crystal, thus n_g should be less than 1. In regions with low crystal density, by Hunziker's model, diffusive interaction between Cu, Nb, B, Si atoms serve as

a drag force to hinder crystal growth[16], thus n_g should be in the range from 0 to 1.

Chapter 6 CONCLUSIONS

The objective of this project is to elucidate the effect of individual and combined alloying additions of 1 at% Cu and 3 at% Nb on the crystallization mechanism of initially amorphous Fe-Si-B-Nb-Cu alloys. Four Fe-Si-B base alloy compositions were selected in this project: $Fe_{77.5}Si_{13.5}B_9$, $Fe_{76.5}Si_{13.5}B_9Cu_1$, $Fe_{74.5}Si_{13.5}B_9Nb_3$ and $Fe_{73.5}Si_{13.5}B_9Nb_3Cu_1$. The thermal properties were studied by DSC, the phase formation during crystallization was identified by XRD techniques, microstructural observations were carried out by conventional and hot stage in-situ TEM. Direct quantitative TEM analysis was also conducted to obtain crystal density and crystal size as a function of annealing temperature and time. The magnetic properties were measured by VSM. Based on the results the individual and synergistic effects of Cu and Nb alloying additions in the Fe-Si-B alloys were determined.

6.1 $Fe_{77.5}Si_{13.5}B_9$ alloy

1. Crystallization of the initially amorphous Fe-Si-B alloy shows that a two–step crystallization processes occurred. The crystallization temperatures at a heating rate of 10 K/min were 507 °C and 542 °C and the activation energy for the two crystallization processes are 376±5.9 kJ/mol and 342±38.7 kJ/mol respectively.

2. An unusual solid-state dendritic morphology of the Fe-Si primary crystals was observed, the branches were composed of closely spaced individual crystals, the spacing between the crystals was of the order of nanometer.

3. The products of secondary crystallization are the Fe-Si phase with B2 ordered

structure and the Fe_3B phase. These phases grew not only among the dendritic branches but also within the dendrites at the interfaces of the closely spaced crystals.

4. Interestingly during hot stage in-situ TEM observation the equiaxed morphology was found to change to a dendritic morphology beyond a critical crystal radius of about 45 nm. These observations could be explained by morphological stability theories.

6.2 Effect of Cu alloying addition

1. The DSC results show that with 1 at% Cu alloying addition ($Fe_{76.5}Si_{13.5}B_9Cu_1$) the primary and secondary crystallization temperatures are lowered to 466 °C and 531 °C. Cu alloying addition reduced the activation energy to 260±5.86 kJ/mol and 257±30.14 kJ/mol for primary and secondary crystallization respectively.

2. The phases formed after secondary crystallization are the same for both the Fe-Si-B and the Fe-Si-B-Cu alloys, i.e. Fe-Si, Fe_2B and Fe_3B. During secondary crystallization the Fe-Si phase formed in the Fe-Si-B and Fe-Si-B-Cu alloys had a b.c.c and DO3 crystal structure, respectively.

3. Cu alloying additions increased the saturation magnetization during primary crystallization but decreased the saturation magnetization during secondary crystallization. The saturation magnetization and coercivity showed similar trends in both alloys, the extent of the change in magnetic properties is higher for the Fe-Si-B-Cu alloy correspond to the Fe-Si-B alloy.

4. 1 at% Cu alloying addition alone does not result in the high crystal density and small crystal size observed in the Fe-Si-B-Nb-Cu alloy. Cu alloying addition influences both nucleation and growth processes resulting in a spheroidal morphology with rough

interfaces about 100 nm in size, there is an increase in crystal density and reduction in crystal size compared to the Fe-Si-B alloy. However, the crystal density in the Fe-Si-B-Cu alloy is much less than that in the Fe-Si-B-Nb-Cu alloy.

6.3 Effect of Nb alloying addition

1. The DSC results show two distinct exothermic peaks in the Fe-Si-B alloy, However, only one peak is observed in the Fe-Si-B-Nb alloy. The crystallization temperature increased to 589 ^{o}C in the Fe-Si-B-Nb alloy. Nb alloying addition increased the activation energy of crystallization to 549±35.7 kJ/mol.

2. After heat treatment, it was found from XRD, TEM and HRTEM results that Nb alloying additions induced the formation of the $Fe_{23}B_6$, Fe_3B phases which were not observed in the Nb free alloys.

3. Alloying addition of Nb decreased the saturation magnetization compared with the corresponding value of the Nb free alloy for the same annealing condition.

4. 3 at% Nb alloying additions induced a change in morphology to that of equiaxed crystals and also resulted in a change of crystallization mechanism from primary to eutectic crystallization. There was an increase in crystal density and reduction of crystal size to a higher degree compared with 1 at% Cu alloying additions, However, Nb alloying additions alone are not sufficient to form the high crystal density and small crystal size observed in the Fe-Si-B-Nb-Cu alloy. Hence, it is clear that synergistic effects are the key to nanostructure formation of the Fe-Si-B-Nb-Cu alloys.

6.4 Effect of Nb and Cu alloying additions

1. Three exothermic peaks are observed in the DSC measurements conducted at a heating rate of 10 K/min, the peaks are at 524 °C, 681 °C and 715 °C. The activation energy corresponding to the peaks were 360±40.1 kJ/mol, 456±40.1 kJ/mol and 381±23.8 kJ/mol.

2. It is interesting to note that addition of 1 at% Cu to Fe-Si-B-Nb resulted in primary crystallization and the same Fe-Si phase was found in the other three alloys.

3. The phases formed after crystallization were identified by XRD and TEM, the product of primary crystallization was a higher density of 10 nm size b.c.c. Fe-Si crystals, the secondary crystallization product was the Fe_3B phase. The Fe_3B phase decomposed into Fe_2B and α-Fe phases at higher temperature. A striped morphology of the Fe_3B phase was observed after the alloy was heat treated at 600 °C for 1 h.

4. EELS element mapping for Cu and Nb at 500°C for 10 min indicated the formation of both Cu and Nb clusters, these clusters can serve as nucleation sites for the subsequent crystallization. EELS element mapping for B and Nb showed that B and Nb atoms were rejected and surround the crystals, consistent with Hermann's model that Nb-B aggregates hinder the crystal growth.

5. EDS measurement of composition in the nanocrystals of the Fe-Si phase suggested that the concentration profile of Cu and Nb showed opposite trends.

6. Our model of nanocrystallization focuses on the key synergistic effects of Cu and Nb combined alloying additions. The compositional and structural results suggest that repulsion between Cu and Nb atoms resulted in the formation of both Cu rich and Nb rich regions, which is helpful for the formation of Cu and Nb clusters. In regions with low

crystal density, Cu clusters can act as nucleation sites consistent with Hono's model. And the retardation of growth in regions with low crystal density the growth rate was reduced, as suggested by the Hunziker's model, by the strong interaction of Cu, Si, Nb and B. In the regions with a high crystal density Nb clusters can act as nucleation sites due to the similar b.c.c. structure of Fe and Nb and the strong attractive interaction between Si and Nb atoms. Soft impingement and Nb-B aggregates were crucial to inhibit the crystal growth.

REFERENCES

1 Yoshizawa, Y., Oguma, S., and Yamauchi, K. (1988). New Fe-based soft magnetic alloys composed of ultrafine crystal structure, J. Appl. Phys., 64, 6044-6046.

2 Yoshizawa, Y., Yamauchi, K., Yamane, T., and Sugihara, H. (1988). Common mode choke cores using the new Fe-based alloys composed of ultrafine crystal structure, J. Appl. Phys., 64, 6047-6049.

3 Herzer, G. (1990). Crystal size dependence of coercivity and permeability in nanocrystalline ferromagnets, IEEE Trans. Magn., 26, 1397-1402.

4 Hono, K., Hiraga, K., Wang, Q., Inoue, A., and Sakurai, T. (1992). The micorstructure evolution of an $Fe_{73.5}Si_{13.5}B_9Nb_3Cu_1$ nanocrystalline soft magnetic material, Acta Metal. Mater., 40, 2137-2147.

5 Hono, K., Li, J. L., Ueki, Y., Inoue, A., and Sakurai, T. (1993). Atom probe study of the crystallization process of an $Fe_{73.5}Si_{13.5}B_9Nb_3Cu_1$ amorphous alloy, App. Surf. Sci., 67, 398-406.

6 Hono, K. (2002). Nanoscale microstructure analysis of metallic materials by atom probe field microscopy, Prog. Mater. Sci., 47, 621-729.

7 Yoshizawa, Y., and Yamauchi, K. (1991). Magnetic properties of Fe-Cu-M-Si-B (M = Cr, V, Mo, Nb, Ta, W) alloys, Mater. Sci. Eng. A, 114, 176-179.

8 Ayers, J. D., Harris, V. G., Sprague, J. A., Elam, W. T., and Jones, H. N. (1997). A model for nucleation of nanocrystals in the soft magnetic alloy $Fe_{73.5}Nb_3Cu_1Si_{13.5}B_9$, Nanostruct. Mater., 9, 391-396.

9 Ayers, J. D., Harris, V. G., Sprague, J. A., Elam, W. T., and Jones, H. N. (1998). On the formation of nanocrystals in the soft magnetic alloy $Fe_{73.5}Nb_3Cu_1Si_{13.5}B_9$, Acta Mater., 46, 1861-1874.

10 Duhaj, P., Svec, P., Sitek, J., and Janickovic, D. (2001). Kinetic and structural aspects of the formation of nanocrystalline phases in $Fe_{73.5-x}Ni_xCu_1Nb_3Si_{13.5}B_9$ alloys, Mater. Sci. Eng. A, 304-306, 178-186.

11 Yavari, A. R., and Negri, D. (1997). Effect of concentration gradients on nanostructure development during primary crystallization of soft-magnetic iron-based amorphous alloys and its modeling, Nanostruct. Mater., 8, 969-986.

12 Gupta, A., Kane, S. N., Bhagat, N., and Kulik, T. (2003). Effect of Cu, Nb and Ta addition on the structural and magnetic properties of amorphous Fe-Si-B alloys, J. Magn. Magn. Mater., 492, 254-255.

13 Hermann, H., Mattern, N., Roth, S., and Uebele, P. (1997). Simulation of crystallization processes in amorphous iron-based alloys, Phys. Rev. B, 56, 13888-13897.

14 Blazquez, J. S., Franco, V., and Conde, A., (2002), The influence of Cu additions on the crystallization and magnetic properties of FeCoNbB alloys, J. Phys.: Condens. Mater., 14, 11717-11727.

15 Teresa. M., Mora. C., Clavaguera. N., Crespo D., and Pradell T. (2002). Crystallisation kinetics and microstructure development in metallic systems, Prog. Mater. Sci., 47, 559-619.

16 Hunziker, O. (2001). Theory of plane front and dendritic growth in multicompnent alloys, Acta Mater., 49, 4191–4203.

17 Zhong, L. W., liu, Y., and Wang, Z., (2002). Handbook of Nanophase and Nanostructured Materials, 245, Tshinghua University Press.

18 Morris, D. G. (1981). Crystallisation of the Meglas 2826 amorphous alloy, Acta Metall., 29, 1213-1220.

19 Yang, M. J., and German, R. M. (1999), Novel 'sendust' alloys with high mechanical and magnetic properties, Met. Powder Rep., 5439

20 Duckham, A., Zhang, D. Z., Liang, D., Luzin, V., Cammarata, R. C., Leheny, R. L., Chien, C. L., and Weihs, T. P. (2003). Temperature dependent mechanical properties of ultra-fine crystallized FeCo–2V, Acta Mater., 51, 4083-4093.

21 Tatsuya T., Hiroshi O., Mitsuhiro H., (2004), Thermodynamic evaluation of the phase equilibria and glass-forming ability of the Fe–Si–B system, Computer Coupling of Phase Diagrams and Thermochemistry, 28, 354–362

22 Naitoh, Y., Bitoh, T., Hatanai, T., Makino, A., Inoue, A., and Masumoto, T. (1997). Applications of nanocrystalline soft magnetic Fe-M-B (M = Zr, Nb) alloys, Nanostruct. Mater., 8, 987-995.

23 Hasegawa, N., Fujimori, H., Kataoka, N., and Hiraga, K. (1993). Relation between microstructure and soft magnetic properties of nanocrystalline Fe/Fe-H_f-C multilayers, J. Magn. Magn. Mater., 126, 583-586.

24 Lovas, A., Varga, B., Kiss, L. F., Nakonechna, L., and Kalincsák, Z. (2003). The evolution of soft magnetic properties and the related density change during amorphous–nanocrystalline transformation, J. Magn. Magn. Mater., 254-255, 489-493.

25 Yoshizawa, Y. (2001). Magnetic properties and applications of nanostructured soft magnetic materials, Scripta Mater., 44, 1321-1325.

26 Shindo, D., Park, Y. G., and Yoshizawa, Y. (2002). Magnetic domain structures of $Fe_{73.5}Cu_1Nb_3Si_{13.5}B_9$ films studied by electron holography, J. Magn. Magn. Mater., 238, 101-108.

27 Sabolek, S., Babic, E., Popovic, S., and Herzer, G. (1997). Influence of core current on magnetization processes in amorphous and nanocrystalline $Fe_{73.5}Cu_1Nb_3Si_{15.5}B_7$ ribbons, Mater. Sci. Eng. A, 226-228, 507-510.

28 Herzer, G. (1996). Nanocrystalline soft magnetic materials, J. Magn. Magn. Mater., 157-158, 133-136.

29 Twarowski, K., Lachowicz, H. K., Kunminski, M., Slawska-Waniewska, A., and Herzer, G. (1995). Magnetostriction and its temperature dependence in FeCuNbSiB nanocrystalline alloy, J. Magn. Magn. Mater., 150, 85-92.

30 Herzer, G. (1995). Soft magnetic nanocrystalline materials, Scripta Metall. Mater., 33, 1741-1756.

31 Benda, O., Bydzovsky, J., and Herzer, G. (1995). Temperature dependence of magnetic properties of nanocrystalline materials annealed in a magnetic field, J. Magn. Magn. Mater., 140-144, 479-480.

32 Makino, A., Inoue, A., and Masumoto, T. (1995). Nanocrystalline Soft Magnetic Fe-M-B(M=Zr, H_f, Nb) Alloys Produced by Crystallization of Amorphous Phase, Mater.Trans. JIM, 36, 924-927.

33 Nalwa, H. S. (2001). Handbook of advanced electronic and photonic and devices, Vol6, Academic Press, San Diego, 77.

34 Makin, A. O., Hatanai, T., Inoue, A., and Masumoto, T. (1997). Nanocrystalline soft magnetic Fe-M-B (M = Zr, Hf, Nb) alloys and their applications, Mater. Sci. Eng. A, 226-228, 594-602.

35 Drbolav, O., Bochu, B., Yavari, A. R., Baro, M. D.,and Surinach, S. (1995). On the role of Cu in the nanocrystallization of Fe-Zr-Based melt spun amorphous alloys, Mater. Sci. Forum, 179-181, 569-574.

36 Zhang, Y., Hono, K., Inoue, A., and Sakurai, T. (1996). Clustering of Cu prior to the crystallization reaction in an Fe-Zr-B-Cu amorphous alloy, Scripta Mater., 34, 1705-1710.

37 Zhang, Y., Inoue, A., Sakurai, T., and Hono, K. (1996). APFIM studies of nanocrystalline microstructural evolution in Fe-Zr-B(-Cu) amorphous alloys, Mater. Sci. Eng. A, 217-218, 407-413.

38 McHenry, M. E., Johnson, F., Okumura, H., Ohkubo, T., Ramanan, R. V., and Laughlin, D. E. (2003). The kinetics of nanocrystallization and microstructural observations in FINEMET, NANOPERM and HITPERM nanocomposite magnetic materials, Scripta Mater., 48, 881-887.

39 Michael, M. E., Matthew, A. W., and David, E. L. (1999). Amorphous and nanocrystalline materials for applications as soft magnets, Prog. Mater. Sci., 44, 291-433.

40 Herzer, G., Hernando, A., Marín, P., and Vázquez, M. (1998). Thermal dependence

of coercivity in magnetic nanostructures, J. Magn. Magn. Mater., 177-181, 959-961.

41 Herzer, G. (1994). Magnetic field induced anisotropy in nanocrystalline Fe-Cu-Nb-Si-B alloys, Mater. Sci. Eng. A, 181-182, 876-879.

42 Chudnovsky, E. M., Saslow, W. M., and Serota, R. A. (1986). Ordering in ferromagnets with random anisotropy, Phys. Rev. B, 33, 251-261.

43 Herzer, G., Suzuki, K., and Cadogan, J. M. (1998). The effect of coherent uniaxial anisotropies on the crystal-size dependence of coercivity in nanocrystalline soft magnetic alloys, J. Magn. Magn. Mater., 177-181, 949-950.

44 Tejedor, M., Hernando, B., Sanchez, M. L., Prida, V. M., Garcia-Beneytez, J. M., Vázquez, M., and Herzer, G. (1998). Magnetoimpedance effect in zero magnetostriction nanocrystalline $Fe_{73.5}Cu_1Nb_3Si_{16.5}B_6$ ribbons, J. Magn. Magn. Mater., 185, 61-65.

45 Alves, F., Simona, F., and Hubert, O. (2004). Analysis of both nanocrystallization and creep-induced anisotropy kinetics in Fe–Si–B–Cu–Nb alloys, Mater. Sci. Eng. A, 375-377, 1011-1014.

46 Illekova, E. (2002). FINEMET-type nanocrystallization kinetics, Therm.Acta., 387, 47–56.

47 Barandiar, J. M., Telleria, I., Garitaonand, J. S., and Davies, H. A. (2003). Kinetic aspects of nano-crystallization in Finemet-like alloys, J. Non-Cryst. Solids, 329, 57–62.

48 Borrego, J. M., Conde, C. F., Millb, M., Conde, A., Caphan, M. J., and Joulaud, J. L. (1998). Nanaocrystallization in $Fe_{73.5}Si_{13.5}B_9Cu_1Nb_1Xz$(X=Nb, Mo and V) alloy studies by X-ray synchrotron radiation, Nanostruct. Mater., 10, 575-583.

49 Ciavaguera, N., Pradell, T., Zhu, J., and Clavaguera-Mora, M. T. (1995). Thermodynamics and kinetics controlling the formation of nanocrystalline FeCuNbSiB materials, Nanostruct. Mater., 6, 453-456.

50 Barbatti, C. F., Sinnecker, E. H. C. P., Sarthour, R. S., and Guimaraes, A. P. (2004). NMR study of the crystallization kinetics in FINEMET-type materials, J. Alloy. Compd., 369,136–140.

51 Illekova. E., Czomorovd. K., Kuhnast. F. A., and Fiorani. J. M. (1996). Transformation kinetics of the $Fe_{73.5}Cu_lNb_3Si_{13.5}B_9$ ribbons to the nanocrystalline state, Mater. Sci. Eng. A, 205,166-179.

52 Ozawa, T. (2000). Temperature control modes in thermal analysis, Pure Appl. Chem., 72, 2083–2099.

53 Lecaude, N., and Perron, J. C. (1998), Proceedings of the International Symposium on Metastable, Mechanically Alloyed and Nanocrystalline Materials, vol. 269–272. Mater. Sci. Forum, USA: Trans Tech Publ;

54 Fanfoni, M., and Tomellini, M. (1996). Demonstration of Avrami's kinetics: Connection with rate equations for clustering on surfaces, Phys. Rev. B, 54, 9828-9833.

55 Erukhimovitch, V., and Baram, J. (1994). Crystallization kinetics, Phys. Rev. B, 50, 5854-5856

56 Sessa, V., Fanfoni, M., and Tomellini, M. (1996). Validity of Avrami's kinetics for random and nonrandom distributions of germs, Phys. Rev. B, 54, 836-841

57 Uebele, P., and Hermann, H. (1996). Computer simulation of crystallization kinetics with non-Poisson distributed nuclei, Model. Simul. Mater. Sci. Eng., 4, 203-214.

58 Pradell, T., Crespoz, D., Clavaguerax, N. and Clavaguera-Morak, M. T. (1998). Diffusion controlled crystal growth in primary crystallization: Avrami exponents revised, J. Phys.: Condens. Mater., 10, 3833–3844.

59 Atkinson. H. V. (1988). Overview no. 65: Theories of normal crystal growth in pure single phase systems, Acta Metall., 36, 469-491.

60 Illekova. E., Czomorovd. K., Kuhnast. F. A., and Fiorani. J. M. (1996). Transformation kinetics of the $Fe_{73.5}Cu_lNb_3Si_{13.5}B_9$ ribbons to the nanocrystalline state, Mater. Sci. Eng. A, 205,166-179.

61 Koster, U., Schiinemann, U., Blank-Bewersdorff, M., Brauer, S., Sutton, M., and Stephenson, G. B. (1991). Nanocrystalline materials by crystallization of metal-metalloid glasses, Mater. Sci. Eng. A, 133, 611-615.

62 Kiss, L. F., Ková, J., and Lovas, A. (2003). Influence of early stages of nanocrystallization on the low-temperature magnetic properties of nanocrystalline ribbons, J. Magn. Magn. Mater., 254-255, 486-488.

63 Haslar, V., Kraus, L., Dlouhý, D., Duhaj, P., and Svec, P. (1996). Influence of Si and Nb content on magnetostriction and creep-induced magnetic anisotropy of nanocrystalline Fe-Nb-Cu-Si-B alloys, J. Magn. Magn. Mater., 160, 257-258.

64 Zhang, Y., Hono, K., Inoue, A., and Sakurai, T. (1996). APFIM studies of nanocrystalline microstructural evolution in Fe-Zr-B(-Cu) amorphous alloys, Mater. Sci. Eng. A, 217/218, 407-413.

65 Duhaj, P., Matko, I., Švec, P., and Janickovic D. (1995). Structural characterization

of the finemet type alloys, J. Non-Cryst. Solids, 192and193, 561-564.

66 Duhaj, P., Matko, I., Švec, P., Sitek, J., and Janickovic, D. (1996). Structural investigation of Fe(Cu)ZrB amorphous alloy, Mater. Sci. Eng. B, 39, 208-215.

67 Zhang, Y. D., Budnick, J. I., Ford, J. C., and Hines, W. A. (1991). Some applications of NMR to the study of magnetically-ordered materials with emphasis on the short-range order in (Fe-B)-based crystalline and amorphous alloys, J. Magn. Magn. Mater., 100, 13-37.

68 Hirotsu, Y. (1994). High resolution electron microscopy of medium-range order in amorphous alloys, Mater. Sci. Eng. A, 179-180, 97-101.

69 Chau, N., Hoa, N. Q., and Luong, N. H. (2005). The crystallization in Finemet with Cu substituted by Ag, J. Magn. Magn. Mater., 290–291,1547–1550.

70 Conde, C. F., Millán, M., and Conde, A. (1998). Crystallization behavior of FeSiB–XNb (X=Pd, Pt) alloys, J. Non-Cryst. Solids, 232-234, 346-351.

71 Panda, A. K., Chattoraj, I., and Mitra, A. (2000). Structural and soft magnetic properties of $Fe_{73.5}Nb_3M_1Si_{13.5}B_9$ (M=Cu, Mn, Pt), J. Magn. Magn. Mater., 222, 263-270.

72 Botta, W. J., Negri, F. D., and Yavari, A. R. (1999). Crystallization of Fe-based amorphous alloys, J. Non-Cryst. Solids, 247, 19-25.

73 Lecaude, N., and Perron, J. C. (1997). Nanocrystallization mechanisms in Finemet-type alloys from calorimetric studies, Mater. Sci. Eng. A, 226-228, 581-585.

74 Lecaude, N., and Perron, J. C. (1996). Modelling of nanocrystallization in Finemet-type alloy from enthalpy measurements, J. Magn. Magn. Mater., 160, 263-265.

75 Hermann, H., Heinemann, A., Mattern, N., and Wiedenmann, A. (2000). Experimental evidence for inhibitor-controlled mechanism of nanocrystallisation in amorphous metallic alloys, Europhys. Lett., 51,127–132.

76 Michael, E. B. (1988). Introduction to Thermal Analysis: Techniques and Applications New York, P23

77 Fultz B., and Howe, J., Transmission Electron microscopy and Diffractometry of Materials, New York, P63-75

78 Goodhew, Peter J. (2001). Electron microscopy and analysis, Taylor and Francis, , New York, 191-193

79 Malis, T., Cheng, S., and Egerton, R. F. (1988). EELS log-ratio technique for specimen-thickness measurement in the TEM. Journal Electron Microscope Technique, 81, 93-200.

80 Y. R. Zhang and R. V. Ramanujan (2006). A study of the crystallization behavior of an amorphous $Fe_{77.5}Si_{13.5}B_9$ alloy, Mater. Sci. Eng. A., 416, 161-168.

81 Kulik, T., Horuba, T., and Matyja, H. (1992). Flash annealing nanocrystallization of Fe---Si---B-based glasses, Mater. Sci. Eng. A, 157, 107-112.

82 Noh, T. H., Lee, M. B., Jim, H. J., and Kang, I. K. (1990). Relationship between crystallization process and magnetic properties of Fe-(Cu-Nb)-Si-B amorphous alloys, J. Appl. Phys., 675 568

83 Kim, W. T., and Jang, P. W. (1994). Heat treatment of melt-spun amorphous Fe-Si-B-Cu-Nb alloy, Mater. Sci. Eng. A, 179/A180, 309

84 Matko, I., Duhaj, P., Svec, P., and Janickovic, D. (1994). Formation of nuclei of metastable phases in nanocrystalline materials, Mater. Sci. Eng. A, 179/A180, 557-562.

85 Zhou, F., He, K. Y., and Sui, M. L. (1994). Nucleation and growth characteristics of amorphous Fe-Si-B-(Cu)-(Nb) alloys during isothermal crystallization process, Mater. Sci.Eng. A, 181/182, 1419-1422.

86 Y. R. Zhang and R. V. Ramanujan (2006). The effect of Copper alloying additions on the crystallization of an amorphous Fe-Si-B alloy, J. Mater. Sci., 41, 5292-5301

87 Y. R. Zhang and R. V. Ramanujan (2005). The effect of niobium alloying additions on the crystallization of a Fe–Si–B–Nb alloy, J. Alloys. Compd., 403, 197-205

88 Y. R. Zhang and R. V. Ramanujan (2006). Characterization of the effect of alloying additions on the crystallization of an amorphous $Fe_{73.5}Si_{13.5}B_9Nb_3Cu_1$ alloy, Intermetallics, 14, 710-714

89 Duhaj, P., Svec, P., Janickovic, D., Mako, I., and Hlasnik, M. (1992). Structural and magnetic properties of the Finemet alloy $Fe_{73}Cu_1Nb_3Si_{13.5}B_{9.5}$, Mater. Sci. Eng. B, 14, 357-364.

90 Kamruzzaman, M., Rahman, I. Z., and Rahman, M. A. (2003). The coercivity dependence of giant magneto-impedance effect in Fe–Cu–Nb–Si–B based metallic alloy ribbon at different crystalline stages, J. Magn. Magn. Mater., 262, 162-165.

91 Conde, C. F., and Conde, A. (1995). Amorphous to Nanocrystalline Transformation of a Finemet-Type Alloy, Mater. Sci. Forum, 179-181, 581-586

92 Hirsch, P., Howie, A., Nicholson, R. B., Pashley, D. W. and Whelan, M. J. (1977).

Electron microscopy of thin crystals (pp. 424-427). Huntington, New york: Robert E. Krieger Publishing Company.

93 Wosik, J., Dubiel, B., Kruk, A., Penkalla, H. J., Schubert, F., and Czyrska-Filemonowicz, A. (2001). Stereological estimation of microstructural parameters of nickel-based superalloy Waspaloy using TEM methods, Mater. Charact. 46, 119-123.

94 Penkalla., H. J., Wosik., J., and Czyrska-Filemonowicz., A. (2003). Quantitative microstructural characterization of Ni-base superalloys, Mater. Chem.and Phys 81, 417-423.

95 Y. R. Zhang and R. V. Ramanujan (2006) Microstructural observations of the crystallization of amorphous Fe-Si-B based magnetic alloys, Thin Solid Film, 505, 97-102

96 Efthimiadis, K. G., Polychroniadis, E. K., Chadjivasiliou, S. C., and Tsoukalas, I. A. (2000). Influence of Cu admixtures on the crystallization of amorphous $Fe_{75}Si_9B_{16}$, Mater. Res. Bull., 35, 937-944.

97 Efthimiadis, K. G., Stergioudis, G., Chadjivasiliou, and S. C., Tsoukalas, I. A. (2002). On magnetic properties and thermal stability of Fe(M)-Si-B(M=V, Ni, Cu, Nb, Mo, Pd, Ag) Amorphous alloys, Cryst. Res. Techno., 37, 827-833.

98 dos Santos, D. S., and dos Santos, D. R. (2002). Crystallization kinetics of Fe–B–Si metallic glasses, J. Non-Cryst. Solids, 304, 56–63.

99 Chrissafis, K., Maragakis, M. I., Efthimiadis, K.G., and Polychroniadis, E. K. (2005). Detailed study of the crystallization behavior of the metallic glass $Fe_{75}Si_9B_{16}$, J. Alloy.

Compd., 386, 165-173.

100 Gibson, M. A., and Delamore, G. W. (1989). Crystallization of low silicon content Fe-Si-B metallic glasses, Mater. Sci. Eng. A, 117, 255-262.

101 Bang, J. Y., and Lee, R. Y. (1991). crystallization of the metallics glass $Fe_{78}B_{13}Si_9$, J. Mater. Sci., 26, 4961-4966.

102 Bhatti, A. R., and Cantor, B. (1994). Crystallization of amorphous $Fe_{78}B_{13}Si_9$, J. Mater. Sci., 29, 816-823.

103 Lubrosky, F. E., (1983), Amorphous Metallic Alloys, London, 151

104 Garba, E. J. D., and Jacobs, R. L., (1986). Electronic-structure and site preference of transition-metal impurities in Fe_3Si, J. Met. Phy., 16, 1485 – 1494.

105 Zhang, Y., and Ivey, D. G. (1998). Fe_3Si formation in Fe–Si diffusion couples, J. Mater. Sci., 33, 3131-3135.

106 Tiller, W. A., Rutter, J. W., Jackson, K. A., and Chalmers, B. (1953). Acta Metall., 1428.

107 Mullins, W. W., and Sekerka, R. F. (1964). Stability of a planar interface during solidification of a dilute binary alloy, J. Appl. Phys., 35, 444-451.

108 Mullins, W. W., and Sekerka, R. F. (1963). Morphological stability of a particle growing by diffusion of heat flow, J. Appl. Phys., 34, 323-329.

109 Ivantsov, G. P., and Doklady, A. N. (1947). Acad. Nauk SSSR, 58, 567.

110 Langer, J. S. (1980). Instability and pattern formation in crystal growth, Rev. Mod. Phy., 5, 21-28.

111 Langer, J. S., and Müller-Krumbhaar, H. (1978). Theory of dendritic growth—I. Elements of a stability analysis, Acta Metall., 26, 1681-1690.

112 Nesbit, L. A., and Laughlin, D. E. (1981). Solid state morphological stability of Ni_4Mo precipitates, J. Crystal growth, 51, 273-278.

113 Kim, S. G., Lee, N. E., and Ra, H. Y. (1988). Dendrite growth of α(Fe,Si) Ferrite in annealed $Fe_{80}Si_8B_{12}$ Metallic glass, J. Crystal growth, 92, 629-638.

114 Chang, C. F., and Marti, J. (1983) J. Mater. Sci., 182297

115 Battezzati, L., Antonoone, C., and Baricco, M. (1997). Undercooling of Ni---B and Fe---B alloys and their metastable phase diagrams, J. Alloys. Compd., 247, 164-171.

116 Muller-Krumbhaar, H., and Langer, J. S. (1981). Sidebranching instabilities in a two-dimensional model of dendritic solidification, Acta Metall., 29, 145-157.

117 Glicksman, M. E., Schaefer, R. J. and Ayers, J. D. (1976). Dendritic Growth---A Test of Theory, Metall. Mater. Trans., 7A, 1747-1759.

118 Marin, P., Vazequez, M., Olofinjana, A. O., and Davies, H. A. (1998). Influence of Cu and Nb on relaxation and crystallization of amorphous FeSiB(CuNb) wires, Nanostruct. Mater., 10, 299-310.

119 Mattern, N., Danzig, A., and Muller, M. (1995). Effect of Cu and Nb on crystallization and magnetic properties of amorphous $Fe_{77.5}Si_{15.5}B_7$ alloys, Mater. Sci. Eng. A, 194, 77-85.

120 Kulik, T. (1997). Low temperature nanocrystallizaztion of iron-based amorphous alloys, Mater. Sci. Forum, 235-238, 421-424.

121 Kulik, T. (1992). The influence of copper, niobium and tantalum additions on the crystallization of Fe-Si-B based glasses, Mater. Sci. Eng. A, 159, 195-201.

122 Kulik, T. (1998). Annealing temperature dependence of size, morphology and composition of primary crystals created in $Fe_{76.5}Cu_1Si_{13.5}B_9$ glass, Mater. Sci. Forum, 269-272, 707-710.

123 Kulik, T., Bucka, D., and Matyja, H. (1993). Effect of flash annealing on the crystal size and morphology of crystallization products of Co-Si-B glasses, J. Mater. Sci. Lett., 12, 76-78

124 Kulik, T. (2001). Nanocrystallization of metallic glasses, J. Non-Cryst. Solids, 287, 145-161.

125 Schwarz, R. B., Shen, T. D., Harms, U., and Lillo, T. (2004). Soft ferromagnetism in amorphous and nanocrystalline alloys, J. Magn. Magn. Mater., 283, 223-230.

126 Chau, N., Hoa, N. Q., and Luong, N. H. (2005). The crystallization in Finemet with Cu substituted by Ag, J. Magn. Magn. Mater., 290-291,1547-1550.

127 Muller, M., Mattern, N., and Illgen, L. (1992). The influence of different Cu/Nb contents on the structure and on the magnetic properties in nanocrystalline Fe-B-Si base alloys, J. Magn. Magn. Mater., 112, 263-268.

128 Mattern, N., Danzig, A., and Muller, M. (1995). Influence of additions on crystallization and magnetic properties of amorphous $Fe_{77.5}Si_{15.5}B_7$, Mater. Sci. Forum, 179-181, 540-544.

129 Graf, T., Hampel, G., Korus, J., Hesse, J., and Herzer, G. (1995). Influence of Nb

concentration on structure and crystallization onset of amorphous Fe(Cu,Nb)SiB finemet alloys, Nanostruct. Mater., 6, 469-472.

130 Donald, I. W., Ward, K. D., Davies, H. A., and Crangle, J. C., 'Proc. 4th Int. Conf. on Rapidly Quenched Metals' Eds. Masumoto, T. and Suzuki, K., Japan. Inst. Met., Sendai(1982)

131 Cahn, R. W., and Haasen, P., Physical Metallurgy, North Holland, 1996, P725

132 Ping, D. H., Hono, K., Kanekiyo, H., and Hirosawa, S. (1999). Microstructural evolution of $Fe_3B/Nd_2Fe_{14}B$ nanocomposite magnets microalloyed with Cu and Nb, Acta Mater., 47, 4641-4651.

133 G Hampel, A Pundt and J Hesse (1992). Crystallization of $Fe_{73.5}Cu_1Nb_3Si_{13.5}B_9$ structure and kinetics examined by X-ray diffraction and Mossbauer effect spectroscopy, J. Phys.: Condens. Matter. ,**4,** 3195-3214.

134 Chen, W. Z., and Ryder, P. L. (1997). TEM observation and EDS analysis of crystalline phases forming in amorphous $Fe_{73.5}Cu_1Nb_3Si_{13.5}B_9$ alloy upon annealing, Mater. Sci. Eng. B, 49, 14-17.

135 Inoue, A., and Takeuchi, A. (2004). Recent progress in bulk glassy, nanoquasicrystalline and nanocrystalline alloys, Mater. Sci. Eng. A, 375-377, 16-30.

136 Wu, Y. Q., Bitoh, T., Hono, K., Makino, A., and Inoue, A. (2001). Microstructure and properties of nanocrystalline Fe–Zr–Nb–B soft magnetic alloys with low magnetostriction, Acta Mater., 49, 4069-4077

137 Pandaa, A. K., Ravikumara, B., Basub, S., and Mitraa, A. (2003). Crystallization

and soft magnetic properties of rapidly solidified $Fe_{73.5}Nb_3Cu_1Si_{22.5-X}B_X$ (X=5, 9, 10, 11.25, 19) alloys, J. Magn. Magn. Mater., 260, 70-77.

138 Conde, C. F., and Conde, A. (1995). Nanocrystallization in $Fe_{73.5}Cu_1Nb_3(Si,B)_{22.5}$ alloys: influence of the Si/B content, Nanostruc. Mater., 6, 457-460.

139 Chen, W. Z., and Ryder, P. L. (1995). X-ray and differential scanning calorimetry study of the crystallization of amorphous $Fe_{73.5}Cu_1Nb_3Si_{13.5}B_9$ alloy. Mater. Sci. Eng. B, 34, 204-209.

140 Varga, L. K., Bakos, Kisdi-Koszd, and Zsoldos. Kiss, L. F. (1994). Time and temperature dependence of nanocrystalline structure formation in a Finemet-type amorphous alloy, J. Magn. Magn. Mater., 133, 280-282.

141 He, K. Y., Sui, M. L., Liu, Y., and Zhao, B. F. (1994). A structural investigation of a $Fe_{73.5}Cu_1Nb_3Si_{13.5}B_9$ nanocrystalline soft magnetic material, J. Appl. Phys., 75, 3684-3686.

142 Rixecker, G., Schaaf, P., and Goner, U. (1992). Crystallization behaviour of amorphous $Fe_{73.5}Cu_1Nb_3Si_{13.5}B_9$, J. Phys.: Condens. Mater., 4, 10295-10310.

143 Herzer, G., and Warlimont, H. (1992). Nanocrystalline soft magnetic materials by partial crystallization of amorphous alloys, Nanostruct. Mater., 1, 263-268.

144 Bouwelen, F., Sietsma, J., Haan, C. D., and Beukel, A. (1992). Quantitative element analysis in high resolution electron microscopy in both phases of nanocrystalline $Fe_{75.5}Cu_1Nb_3Si_{12.5}B_8$, Appl. Phys. Lett., 61, 2536-2538.

145 Ohnuma, M., Hono, K., Onodera, H., Pedersen, J. S., and Linderoth, S. (1999). Cu

clustering stage before the crystallization in Fe-Si-B-Nb-Cu amorphous alloys, Nanostruct. Mater. , 12, 693-696.

146 Massalski, T. B. (1986), Binary alloy phase diagrams, Metals Park, OH, American Society for Metals, 1440-1442

147 Hirotsu, Y., Uehara, M., and Ueno, M. (1986). Microcrystalline domains in amorphous $Pd_{77.5}Cu_6Si_{16.5}$ alloys studied by high-resolution electron microscopy, J.Appl. Phys., 59, 3081-3083.

148 Gonser, U., Ghafari, M., Ackerman, M., Klein, H. P., Bauer, J., and Wagner, H. G. (1982), Rapidly Quenched Metals, Japan Inst. Metals, Sendai, 639.

149 Danzig, A., Mattern, N., and Doyle, S. (1995). An in-situ investigation of the Fe_3Si crystallization in amorphous $Fe_{73.5}Si_{15.5}B_7Cu_1Nb_3$, Nucl. Instr. and Meth. B, 97, 465-467.

151 Villars, P. (Pierre), A. Prince, and H. Okamoto, (1997). Handbook of ternary alloy phase diagrams, Materials Park, OH: ASM International.

APPENDIX I

Table A1 Volume fraction of the Fe-Si-B-Nb-Cu alloy annealed at 500°C for different time:

Time	Real diameter(nm) Standard deviation	Number of crystals/unit volume(/$m^3 \times 10^{22}$)	Volume fraction
10min	10.1/4.21	1.43	1.09%
30min	11.7/4.6	1.51	1.74%
1h	11.9/4.8	2.67	2.45%
4h	12.4/3.17	3.03	2.9%
16h	14.8/1.49	3.35	3.68%

Table A2 Volume fraction of the Fe-Si-B-Nb-Cu alloy annealed at 515°C for different time:

Time	Real diameter(nm) Standard deviation	Number of crystals/unit volume(/$m^3 \times 10^{22}$)	Volume fraction
10min	10.5/4.51	1.75	1.67%
30min	12.4/5.31	2.93	2.05%
1h	13.1/3.69	3.89	2.98%
4h	14.4/5.27	4.23	3.6%
16h	15.1/6.19	4.59	4.89%

Table A3 Volume fraction of the Fe-Si-B-Nb-Cu alloy annealed at 530°C for different time:

Time	Real diameter(nm) Standard deviation	Number of crystals/unit volume(/$m^3 \times 10^{22}$)	Volume fraction
10min	11.8/4.76	3.24	1.89%
30min	13.5/5.23	4.01	3.22%
1h	13.1/6.71	4.74	3.45%
4h	14.3/5.86	5.63	5.76%
16h	15.4/7.11	6.25	6.41%

Table A4 Volume fraction of the Fe-Si-B-Nb-Cu alloy annealed at 550°C for different time:

Time	Real diameter(nm) Standard deviation	Number of crystals/unit volume(/$m^3 \times 10^{22}$)	Volume fraction
10min	13.2/5.27	4.35	3.3%
30min	13.4/6.31	5.41	4.57%
1h	15.5/7.3	7.79	8.24%
4h	18.1/4.69	8.90	10.92%
16h	21.3/6.32	8.32	9.35%

APPENDIX II

Phase Diagram

Binary Phase Diagram of Fe-Si[143]

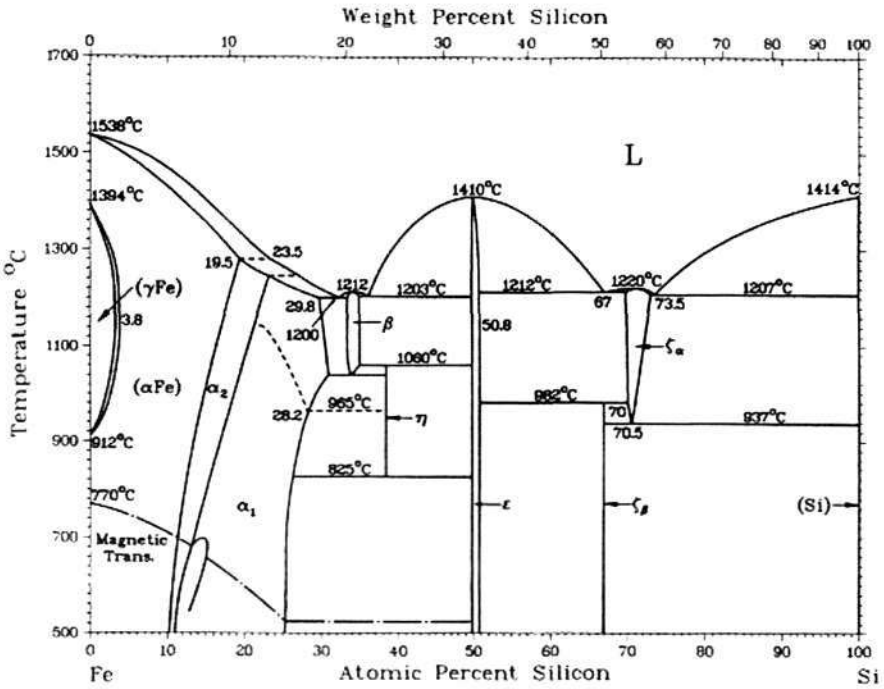

Ternary Phase Diagram of Fe-Si-B at 900°C[148]

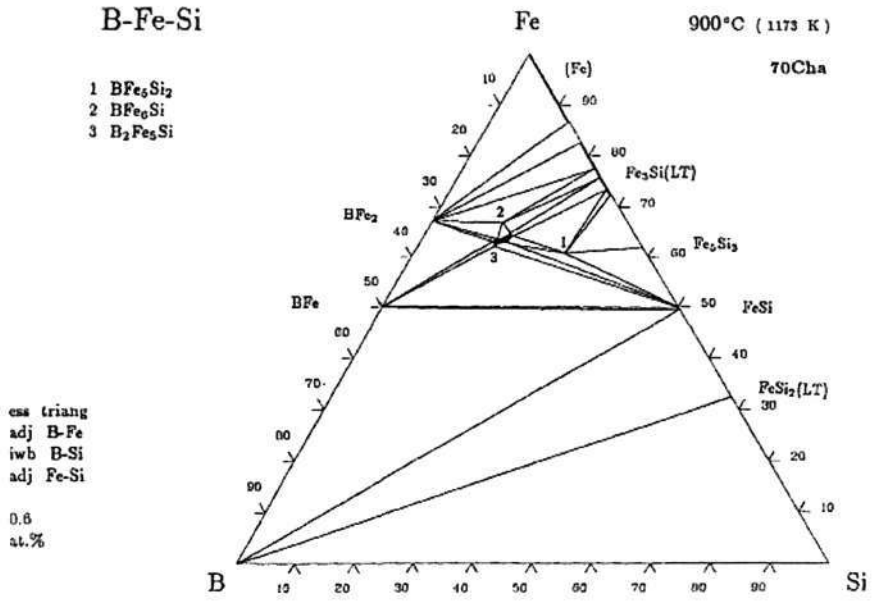

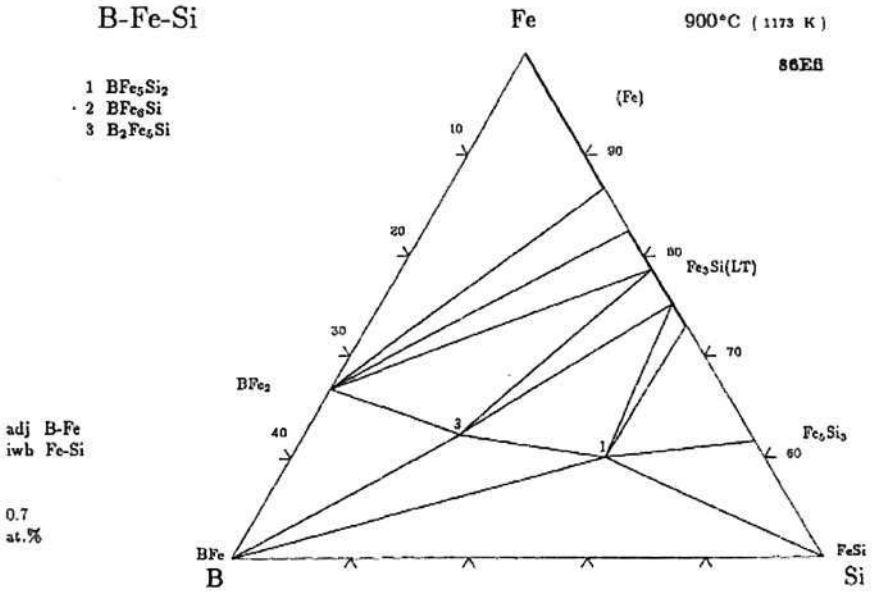

Ternary Phase Diagram of Fe-Si-B at 1000°C[148]

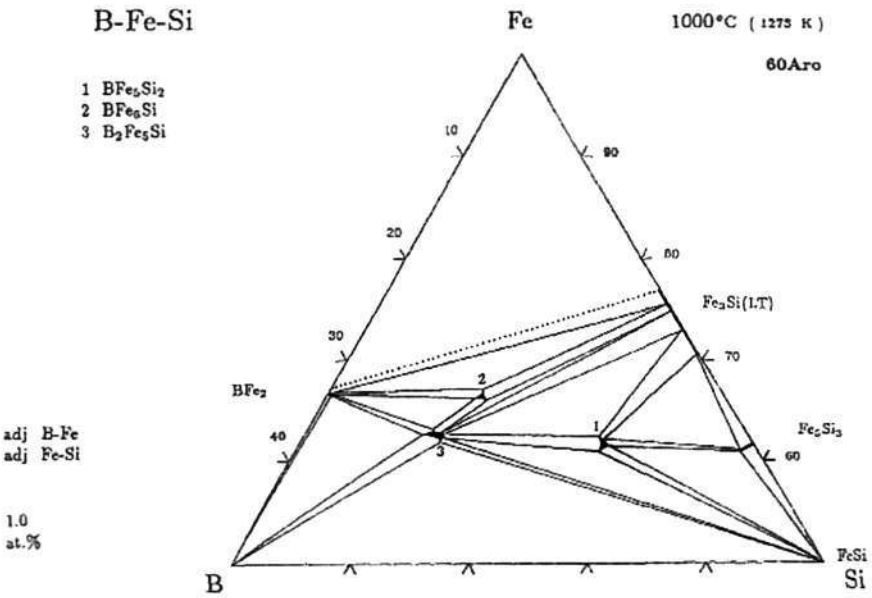

Cu-Nb phase diagram[153]

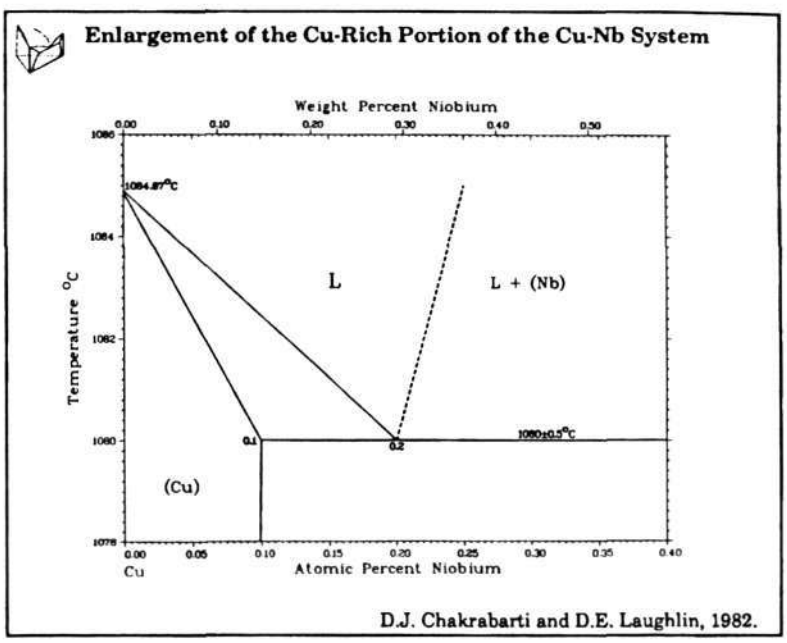

APPENDIX III

Publications:

1. R. V. Ramanujan and Y. R. Zhang,(2006) Quantitative transmission electron microscopy analysis of the nanocrystallization kinetics of soft magnetic alloys, Physical Review B, 74,224408, ***Selected by American Inst. of Physics and American Phys. Soc. for the Virtual J. of Nanoscale Sci. Tech., Dec. 26, 2006.***
2. R. V. Ramanujan and Y. R. Zhang, (2006) Solid state dendrite formation in an amorphous magnetic alloy observed by in-situ hot stage transmission electron microscopy, Appl. Phys. Lett., 88, 182506
3. Y. R. Zhang and R. V. Ramanujan, (2006) Characterization of the effect of alloying additions on the crystallization of an amorphous $Fe_{73.5}Si_{13.5}B_9Nb_3Cu_1$ alloy, Intermetallics, 14, 710-714
4. Y. R. Zhang and R. V. Ramanujan, (2006) The effect of Copper alloying additions on the crystallization of an amorphous Fe-Si-B alloy, J. Mater. Sci., 41, 5292-5301
5. Y. R. Zhang and R. V. Ramanujan, (2006) Microstructural observations of the crystallization of amorphous Fe-Si-B based magnetic alloys, Thin Solid Films, 505, 97-102
6. Y. R. Zhang and R. V. Ramanujan, (2006) A study of the crystallization behavior of an amorphous $Fe_{77.5}Si_{13.5}B_9$ alloy, Mater. Sci. Eng. A., 416, 161-168.

7. Y. R. Zhang and R. V. Ramanujan, (2005) The effect of niobium alloying additions on the crystallization of a Fe–Si–B–Nb alloy, J. Alloys. Compd., 403, 197-205